Modelling of Wind Borne Ice Accretion on Power Transmission Lines

Dissertation

submitted to and approved by the

Department of Architecture, Civil Engineering and Environmental Sciences
University of Braunschweig – Institute of Technology

and the

Faculty of Engineering
University of Florence

in candidacy for the degree of a
Doktor-Ingenieur (Dr.-Ing.) / Dottore di Ricerca
in
Mitigation of Risk due to Natural Hazards on Structures and Infrastructures *)

by
Tobias Wagner
born 24 January 1979
from Bonn, Germany

Submitted on	27 August 2010
Oral examination on	29 October 2010
Professorial advisors	Prof. U. Peil Prof. C. Borri

2010

*) Either the German or the Italian form of the title may be used.

Von der Fakultät Architektur, Bauingenieurwesen und Umweltwissenschaften der Technischen Universität Carolo-Wilhelmina zu Braunschweig zur Erlangung des Grades eines Doktoringenieurs (Dr.-Ing.) genehmigte Dissertation

Eingereicht am	27. August 2010
Disputation am	29. Oktober 2010

Vorsitzender:	Prof. Dr.-Ing. Hocine Oumeraci
Berichterstatter:	Prof. Dr.-Ing. Udo Peil
Berichterstatter:	Prof. Dr.-Ing. Claudio Borri
Prüfer:	Prof. Dr.-Ing. habil. Manfred Krafczyk

„Nichts ist so praktisch wie eine gute Theorie.“

Kurt Lewin

Acknowlegement

First of all I want to thank my tutors Prof. Dr.-Ing. Udo Peil and Prof. Dr.-Ing. Claudio Borri. They gave me the freedom and the support I need to explore such a complex topic as ice accretion on transmission lines is. Furthermore, I would like to thank them for their enthusiasm to found the International Graduate School of Risk Management of Natural and Civilization Hazards on Buildings and Infrastructure (GRK 802), which is affiliated to the Technical University Braunschweig (Germany) and the University of Florence (Italy). It is sponsored by the German Research Foundation (DFG), which I would like to acknowledge here as well. The graduate school provides a lively and encouraging frame for scientific and cultural exchange among students and professors from Italy and Germany. I benefitted especially from discussions with Dr.-Ing. Enzo Marino and Sonja Uphoff on numerical modelling of flows as well as from the support of Christine Winkelvos and David Döhrmann in the field of risk management.

During my research I spend most of my time at the Institute of Steel Structures at the Technical University in Braunschweig and I would like to thank all members of the institute for their collaboration. Especially, I am thankful to Arno Kirch, who is also a member of the graduate school, and Dr.-Ing. Matthias Clobes for many inspiring discussions. The processes of ice accretion are associated with many different research fields. Fortunately, I had the opportunity to discuss my work with competent researchers of all these fields. Especially, I want to thank Prof. Dr.-Ing. habil. Manfred Krafczyk and Dr.-Ing. Claudio Mannini for the discussions of computational fluid dynamics as well as Dr. rer. nat. Günter Schewe for his support in fluid mechanics and for the information and anecdotes on wind tunnel testing and aerospace research he provided. Martin Buchholz supported me with discussions of thermodynamics and helped me to validate my numerical model.

Writing a dissertation obviously requires proofs reading, for which I am thankful to Sarah Wrede and Sandra Singh. A special thanks goes to Robin Rudorf who provided the final revision and much more. In the process he taught me how to write more comprehensively, which is not always an easy task for an engineering scientist, especially when it is not his mother tongue.

A special thanks goes to my family for all the emotional support they provided. Last but not least I want to thank "Giulia di Medici" and her Florentines for a great and inspiring time.

Bonn, June 2011

Tobias Wagner

Abstract

The work presented here enables us to numerically simulate ice accretion on transmission lines. Ice loads can cause significant damage to electric power transmission networks, especially in combination with wind. Overhead lines can collapse due to the mass of ice deposits, but also additional loads due to so-called Galloping oscillation can cause significant damage on the structures. Aerodynamic instability of cables due to ice accretion is a known phenomenon. Investigating shape and density of the ice accretion through experiments is very complex. Therefore, a numerical model is presented to simulate ice accretion processes on cables. The model is divided into two main parts, the calculation of the flow field and the ice accretion. The stream of air and precipitation particles is modelled as a one-way coupled multiphase flow. Ice accretion and flow field are calculated iteratively to account for geometrical changes of the ice deposit in the flow calculation. Finally, a risk management framework and its implications for power outages are investigated. Monetary losses due to blackouts increase exponentially with time. The presented approach evaluates variation in outage duration and compares the risk of blackouts to other types of disasters.

Kurzfassung

Die hier vorgestellte Arbeit ermöglicht die nummerische Simulation der Vereisungen von Hochspannungsleitungen. Dieses meteorologische Phänomen kann erhebliche Schäden an den Leitungsnetzen verursachen, besonders wenn es gemeinsam mit starkem Wind auftritt. Nicht nur das Gewicht der Eisablagerungen kann zum Versagen der Leitungen führen. Angeregt durch den Wind kann es zum sogenannten Seiltanzen kommen. Die Leitungen beginnen zu schwingen, wodurch die Konstruktion erheblich belastet wird. Aerodynamische Instabilität von Seilen als Folge eines durch Eisablagerungen geänderten Querschnitts ist ein bekanntes Phänomen. Da die experimentelle Untersuchung von Vereisungsvorgängen sehr aufwendig ist, soll hier ein numerisches Vereisungsmodell vorgestellt werden. Das numerische Modell besteht aus zwei Berechnungsschritten, die iterativ durchlaufen werden: Zunächst wird die Strömung aus Luft und Niederschlagspartikeln als einfach gekoppelte Zweiphasenströmung berechnet. Basierend auf dem Massestrom der Niederschlagspartikel wird dann das Eiswachstum ermittelt. Abschließend wird ein Risikomanagementkonzept und seine Schlussfolgerungen für die Bewertung von Stromausfällen betrachtet. Der präsentierte Ansatz berücksichtigt die Varianz der Ausfalldauer und ermöglicht den Vergleich von Stromausfällen mit Katastrophenszenarien.

Contents

Nomenclature

Variables written in normal font refer to scalars, those in bold font refer to matrices or vectors. Furthermore, numbers as indices are used to distinguish variables of the same kind.

Latin Letters

A	Reference area the flow passes
$A(\phi)$	Differential operator of the differential equation
A_1, A_2	Contact points of ice and cable surface
$\mathbf{a}_p$	Particle acceleration vector
$a(...)$	Arbitrary function
b	Source term of the differential equation
C_D, C_L, C_M	Aerodynamic drag, lift and momentum coefficient
C^+	Constant of the wall function model
c_p	Specific heat at constant pressure
CST	Cost function
$C_{\varepsilon 1}, C_{\varepsilon 2}, C_\mu$	Constant of the turbulence model
D	Damage
d	Diameter or characteristic diameter
e	Error estimate
$e(T)$	Saturated water vapour pressure in reference to the temperature
$\mathbf{e}_i$	Ice evolution vector
F_D, F_L	Aerodynamic drag and lift force
F_p	Density of the particle flux
F_y	Force in y-directon
f	Vortex shedding frequency
f_d	Dripping frequency
f_n	Differential quantity of the frequency function of the particle diameters
$\mathbf{F}$	Force vector
G	Total incoming radiative heat flux
Gr	Grashof number
g	Gravity
h	Heat transfer coefficient

h_n	Step size of the Runge-Kutta algorithmt
I	Electrical current
J	Total outgoing radiative heat flux
j_1, j_2, j_3, j_4	Parameter of the Runge-Kutta algorithm
k	Turbulent kinetic energy
k_f	Thermal conductivity of a fluid
k_T	Eddy conductivity
k_w	Turbulent kinetic energy at the wall
k_1, k_2, k_3, k_4	Parameter of the Runge-Kutta algorithm
L	Monetary loss
L_e	Latent heat of evaporation at 0 °C
L_f	Latent heat of fusion
LWC	Liquid water content in the air
l	Length or characteristic length
M_k	Centre of the cable
MVD	Medium volume diameter
M_W	Aerodynamic moment
m	Mass
$\mathbf{N}_a \cdot \mathbf{x}_a$	Test function or also called shape function
N_i	Supporting points of the surface algorithm
Nu	Nusselt number
P	Probability of occurrence
P_c	Power generated by the energised conductor
P_f	Power taken by the flow
Pr	Prandtl number
Pr_T	Turbulent Prandtl number
$Pr_{T\infty}$	Constant of the thermal boundary layer model
p	Pressure
Q	Heat source or sink
Q_i	Heat production of the energised conductor
q	Heat transfer
q_c	Heat transfer due to convection
q_d	Heat transfer due to conduction
q_{drip}	Heat transfer due to dripping of pendant drops
q_e	Heat transfer due to evaporation
q_f	Heat transfer due to freezing
q_i	Heat transfer due to Joule heating
q_l	Heat transfer due to warming the supercooled droplets to freezing temperature
$q_r, q_{r,s}, q_{r,l}$	Heat transfer due to radiation, short wave and long wave radiation
q_s	Heat transfer due to sublimation

$q_{0.95}$	95%-quantile
R	Universal gas constant or Macklin's parameter
R_c	Electrical resistance of the conductor
R_D	Risk in terms of damage
R_G	Residual of the approximation
R_L	Risk in terms of loss
Re	Reynolds number
St	Strouhal number
Stk	Stokes number
$\mathbf{S}(z)$	Surface contour defined by cubic splines
$s(z)$	Parametric function
T	Temperature
T^+	Dimensionless temperature
t	Time
U	Average or quasi-steady velocity
u	Velocity
u^+	Dimensionless velocity parallel to the wall
u_*	Friction velocity
V	Volume
$\tilde{V}(...)$	Variances
W	Water supply rate
W_G	Weight function
$\dot{W}$	Heat capacity flux
x	Distance in x-direction
y	Distance in y-direction
y^+, y_1^+, y_2^+	Dimensionless boundary layer depth
z	Free parameter

Greek Letters

α	Collision efficiency
α_C, α_D	Volume fraction of the continuous and disperse phase
α_i	Impact angle of the droplet
β	Collection efficiency
β_{Gr}	Fluid expansion coefficient
ε	Turbulent dissipation rate
$\varepsilon_H, \varepsilon_M$	Eddy diffusivity of heat and momentum
ε_m	Ratio of molecular masses of water and air
ε_r	Surface emissivity

δ	Accretion ratio
δ_{therm}	Boundary thermal boundary layer depth
δ_w	Boundary velocity boundary layer depth
κ	Kármán's constant
λ	Fraction of liquid water within the ice deposit
λ_s	Stabilisation parameter
μ	Dynamic viscosity
μ_T	Eddy viscosity
ρ	Density
ρ_r	Surface reflectivity
σ	Stefan-Bolzmann constant
$\sigma_k, \sigma_\varepsilon$	Constant of the turbulence model
τ	Stress tensor
τ_C, τ_D	Velocity response time of the continuous and the disperse phase
τ_w	Shear stress at the wall
θ	Conductor rotation due to ice accretion and other torsion forces
$\varphi, \widehat{\varphi}$	Angle of attack and angle of attack due to vertical movement only
φ_A	Separation angle
ϕ	Flow variable
ψ	Torsional displacement of the conductor bundle
χ	Accretion efficiency
Ω	Domain of the differential equation

Indices

Some of the symbols and variables presented above may have indices. Their meaning can vary with the subject they refer to.

In case of diameter (d), length (l), heat transfer coefficient (h) and water supply rate (W) as well as for Grashof (Gr), Nusselt (Nu) and Reynolds number (Re) the indices are:

$(\ldots)_c$	Conductor or cylinder
$(\ldots)_d$	Pendent drop
$(\ldots)_{dend}$	Dendritic ice at the icicle tip
$(\ldots)_i$	Icicle
$(\ldots)_p$	Particle
$(\ldots)_t$	Icicle tip
$(\ldots)_w$	Icicle wall
$(\ldots)^N$	Natural convection
$(\ldots)^F$	Forced convection

$(...)_r$ Root

In case of pressure (p), temperature (T), velocity (u) and averaged or quasi-steady velocity (U) as well as for area (A) the indices are:

$(...)_a$ Ambient
$(...)_i$ Impact
$(...)_p$ Particle
$(...)_s$ Surface
$(...)_{rel}$ Relative
$(...)_0$ Initial or quasi-steady

In case of mass (m), volume (V) and density (ρ) the indices are:

$(...)_C$ Continuous phase
$(...)_D$ Disperse phase
$(...)_i$ Ice
$(...)_f$ Fluid
$(...)_p$ Particle
$(...)_s$ Spongy ice
$(...)_w$ Water
$(...)_0$ Stationary average

In case of cost function (CST), loss (L), probability (P) and time (t) the indices are:

$(...)_D$ Dam failure
$(...)_E$ Electricity blackout
$(...)_{0.05,\,0.95}$ 5%-quantile or 95%-quantile
$(...)_{int}$ Interval

Other

$(...)_{max,\,min}$ Maximum or minimum value
$\dot{(...)}$ Derivative of time
$\overline{(...)}$ Average
$(...)'$ Derivative of dimensionless time

$d(...)$	Differential operator
$\partial(...)$	Partial differential operator
$(...)^T$	Transpose
∇	Nabla operator
Δ	Deviation or difference
$*$	Convolution
$\otimes$	Tensor product

Abbreviation

AC	Alternating current
BBK	Bundesamt für Bevölkerungsschutz und Katastrophenhilfe (Federal Office of Civile Protection and Disaster Assistance)
DC	Direct current
DFG	Deutsche Forschungsgemeinschaft (German Research Foundation)
DOF	Degree of freedom
DNS	Direct numerical simulation
CFD	Computational fluid dynamics
FD	Finite difference
FE	Finite element
LES	Large eddy simulation
RANS	Reynolds Average Navier-Stokes
SGS	Subgrid-scale

1 Introduction

1.1 Motivation and Research Objectives

Atmospheric icing occurs when freezing raindrops, supercooled cloud droplets or snow flakes hit a surface. This phenomenon can cause significant damage to electric power transmission networks, especially in combination with wind. Shape and density of ice forming on cables are therefore of major interest in investigating the risk of failure. Large amplitude oscillations at low frequencies and also twisting due to asymmetrical icing of cables can both cause fatigue damages. In extreme weather events atmospheric icing can cause severe damage to towers and power lines [6, 48]. A large number of small-scale failures can cause enormous damage just as well as a single major winter storm event [70, 104]. Examples of such events took place in northern America in 1998 and to a much smaller extent in Germany in 2005, where the devastating power of winter storms left many people without electricity for weeks and caused significant monetary damage [13, 82]. Blackouts cause cascading problem which, with time have major effects on telecommunication, transportation, money transfer and industrial production. Even essential needs like food supply and production or medical services are in danger after a certain period without electricity [11].

The hazards of winter storms raise the question how such a risk should be treated. Investigating the risk of power outages due to winter storms involves a huge number of individual issues. It depends on meteorological scenarios, properties and utilisation of the power network as well as on structural aspects of transmission lines.

The work presented here focuses on a numerical model to simulate ice formation on conductor bundles. Furthermore, risk aspects that distinguish severe power outages from other hazards are investigated.

Three reasons make it seem useful to develop a simulation scheme for icing processes on conductor bundles: Firstly, meteorological observations from the 1950s give a first hint that tandem arrangements of cylinders have an effect on the icing process [23, 162]. Secondly, the vulnerability of modern societies to blackouts is growing with the increasing demand of energy and increasing use of capacity. Since public authorities, in Germany for example, tend to restrict the construction of new transmission lines, bundled conductors are used increasingly to cope with the rising energy demand [55]. Thirdly, experimental investigation of a large number of meteorological conditions and bundle geometries is extremely expensive. Therefore, it is

beneficial to simulate icing processes numerically. Numerical models until now were restricted to single cables due to the assumptions made in the air flow calculation [35, 49, 71, 77, 80, 81].

Consequently, an ice accretion model is developed to investigate:

- Ice formation on transmission lines for a variety of icing conditions.
- The influence of tandem arrangement of cables in conductor bundles on ice accretion.
- Heat transfer within ice deposit and conductor under different conditions.

The risk assessment of winter storms shows a particular characteristic. Blackouts cause mainly monetary losses that increase exponentially with outage duration. Therefore, it seems useful to develop a concept to evaluate variances in hazard duration and to compare blackouts with other types of disasters.

The structure of the work presented here is as follows. Chapter 2 starts with an overview on atmospheric icing and types of ice accretion. It shows the state of the art of modelling icing of conductors. Also a model to simulate the formation of icicles is presented in order to ease the understanding of icing models. Then follow an introduction on dynamic behaviour of transmission lines and strategies for mitigating ice accretion. Chapter 3 describes the ice accretion model developed here. Separate sections explain model structure, fluid dynamic, multiphase flow and heat transfer calculations, which eventually lead to the ice growth computation. Applying the newly developed model ice accretion process is examine in chapter 4. Subsequently, chapter 5 explains a risk management framework suitable for evaluating blackouts and presents a concept to include variance in hazard duration in risk assessment.

2 Atmospheric Icing

2.1 An Overview on Atmospheric Icing

Atmospheric icing is a complex meteorological phenomenon threatening a large variety of man-made structures, such as individual vehicles or buildings as well as whole infrastructure systems. Depending on the meteorological conditions icing is caused by different scenarios. In-cloud icing occurs, as the term indicates, in clouds. Severe events are more likely on structures in mountain regions or on offshore structures exposed to cold clouds and strong winds. Soft hoar frost forms often in the vicinity of open water, where water vapour can transform to ice crystals. Precipitation icing is the term use for ice formation due to wet or dry snow and freezing rain. Significant icing events occur where high precipitation and low temperatures are found. In general, ice accretion is linked to geographic conditions as for example distance to the coast, altitude above sea level and the local topography [15, 52, 116, 172, 178]. Routinely, quantity measurements of ice and snow events are part of meteorological observations to derive probabilities of occurrence and to compare different locations. This data is widely used to create risk maps of expected ice and snow quantities. Due to the complexity of icing processes their accuracy is limited. Makkonen et al. for example found less influences of geographic parameters such as altitude above sea level, instead they emphasised local terrain and relative height above the mean elevation of the surrounding as a crucial criteria for icing intensity [83]. Engineering standards try to include all these aspects within their regulations.

The international standard Atmospheric Icing of Structures ISO 12494 concentrates, as the name indicates, on ice loads [47]. Thus, snow loads on roofs for example are not taken into account. Only static as well as dynamic loads due to ice deposits are covered. Static ice loads, generalised ice shapes and drag coefficients of individual member cross-sections are defined in reference to predefined icing conditions. The standard includes influences of terrain and topographic height as well as meteorological parameters such as precipitation types and temperature. In contrary the European engineering standard Euro Code 1 Part 1-3 [27] accounts for snow loads. It considers different climate conditions of Northern European countries and provides maps showing design snow loads in several European countries. The code includes parameters like altitude above sea level or temperature in the design criteria. Other buildings or local terrain can cause screening of a structure from ice and snow loads. This and also different accumulation due to building height and roof shapes is taken into account. Also overlapping of snow on roof edges is incorporated. The German engineering standard DIN-1055-T5 is

the latest of the above mentioned codes [24]. It adapts both concepts and gives maps for design snow and ice loads in Germany. Extreme snow loads like snow avalanches are not considered, but they are hazardous consequences of snow accumulation in mountain regions. In comparison snowdrift is less drastic, but drift of snow mass can cause interference of roads or railways and also unexpected loads on roofs [9].

Already in the 1940s aircraft engineers faced problems with icing on airfoils [66]. Ice deposits change the aerodynamic behaviour of the airplane and thus it can lose lift force and may crash. Even today large effort are undertaken to investigate icing phenomena on aircrafts. Ships and naval structures are prone to severe icing in cold regions as well, even though salinity of sea water spray reduces the icing rate [78]. The consequences are less threatening, but icing reduces a ship's functional capability. Also wind turbine design has to coupe with ice loads as the turbines suffer significant losses in efficiency and therefore profitability due to iced rotor blades [166]. Also railways are vulnerable to icing, when the contact to the overhead lines are covered with ice [133]. The sensitive infrastructure of electrical transmission lines can suffer enormous damage from large numbers of small-scale failures on single lines as well as from major winter storms [70, 104].

The thesis presented here will focus on this area. For modern society this is a crucial field, as blackout can cause significant problems on telecommunication, transportation and industrial production.

2.2 Types of Snow and Ice Accretion

Different meteorological conditions lead to a large variety of snow and ice deposits. But from an engineering point of view only some of these lead to significant loads on structures namely rime, glaze ice and wet snow [82]. For simplicity's sake the term ice accretion is often used for both, ice as well as snow deposits. Condensing water vapour forms a soft deposit, known as hoar frost. The load is small compared to accumulation of rime or glaze ice and therefore it is not considered here. It can however cause significant energy losses due to corona discharge [28]. Furthermore the electric field of the conductors can have an influence on the evolving ice density, but this aspect is of minor importance here [115]. Solid precipitation in form of snow grains, graupel, hail and ice pellets are not considered as either. They do not stick to transmission lines and hence they are not associated with major loads. Different types of ice and snow precipitations can occur simultaneously and therefore the accretion can show mixed characteristics. However the major classes of ice accretion show distinct characteristics and are described in the following.

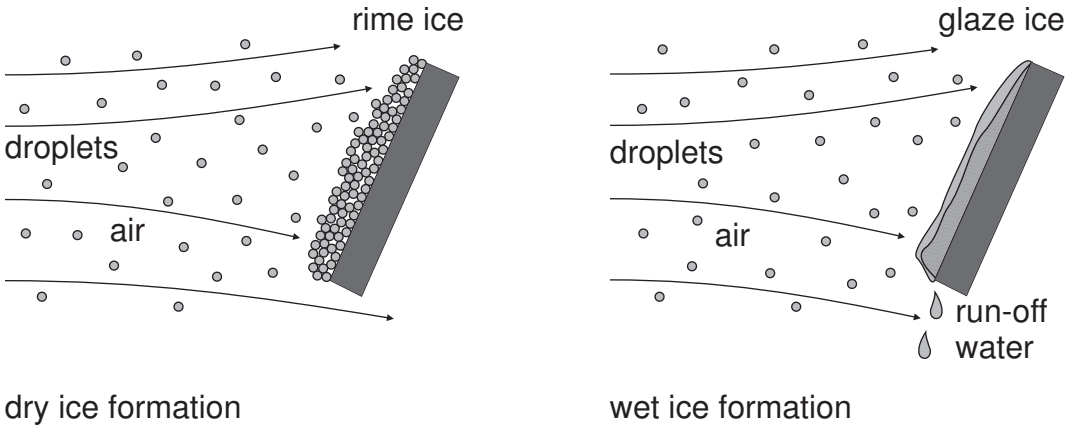

Figure 2.1: Dry ice growth (left) and wet ice growth (right).

2.2.1 Dry and Wet Ice Growing Conditions

The icing conditions influence both the accretion mass and the density of evolving ice. The transition from one growing regime, dry or wet, to the other is dependent on the thermodynamic conditions. When heat loss in the system is lower than heat gain, a liquid layer forms from impinging droplets or melted ice and snow crystals. Ice evolution due to freezing of such water film is called wet growth (cf. figure 2.1). It occurs at temperatures around the melting point, therefore the heat balance is very sensitive. Aforementioned glaze ice and wet snow fall under the term of wet growth. In contrast to that, rime ice develops in dry growing conditions. The heat transfer within the thermal system under dry growing conditions can be neglected, because the latent heat of the droplets released during freezing is dissipated without changing the state of the ice and the surface conditions, hence no liquid layer arises [82].

We need to recall here, that freezing point is not a characteristic property of water, since water droplets can experience temperatures below the freezing point without becoming solid. This process is called super-cooling and can occur, when the freezing temperature is reached, but no nucleus for crystallisation is present. Due to air temperature inversion rain drops fall into a freezing air layer and become supercooled.

2.2.2 Rime Ice

Rime ice forms, when super cooled water droplets hit a surface with a temperature less than $0\,^{\circ}\mathrm{C}$ or at least only slightly above $0\,^{\circ}\mathrm{C}$. It occurs as in-cloud icing due to freezing fog or as precipitation icing due to freezing drizzle. The typical droplet diameter of fog droplets is about $10\,\mu\mathrm{m}$ in a range from 1 to $50\,\mu\mathrm{m}$ [61, 117]. Freezing drizzle are precipitation droplets ranging in diameter from 50 to $500\,\mu\mathrm{m}$ [61, 117]. The density of rime ice deposits varies as result of droplet size, wind velocity and latent heat in the droplets. The so called hard rime has a densely packed crystal matrix leading to a relatively high density varying from 100 to $600\,\mathrm{kg/m^3}$.

Figure 2.2: Rime ice accretion on a transmission line in Norway in 1961. The weight of the ice accretion of $305\,\mathrm{kg/m}$ on each span is the highest ice load ever recorded [82]. (with permission of the Royal Society, photo: Wist, 1961)

The dense rime matrix develops from droplets having either a great momentum or freezing at the surface does not occur instantly due to boundary conditions. Soft rime occurs, when droplets with a small momentum freeze instantaneously on the surface. For this to occur, the temperature usually needs to be below $-5\,^{\circ}\mathrm{C}$ at moderate wind velocities. In this conditions air voids are left between the frozen droplets leading to densities of less than $100\,\mu\mathrm{m}$ [103]. Higher wind velocities cause a more densely packed ice matrix.

2.2.3 Wet Snow

Wet snow occurs when snow is falling through a layer of warm air. It forms an agglomeration of ice crystals, water and air voids. When this occurs, the temperature at the ground is usually from -2 to $+5\,^{\circ}\mathrm{C}$ and the liquid water content in the air is high [103]. Precipitation icing by wet snow can lead to significant loads on structures especially on lattice towers and transmission lines. Depending on the meteorological conditions the snow can possess strong adhesion strength. In combination with strong wind forces wet snow is compressed into compact deposits. The density can vary from 200 to $990\,\mathrm{kg/m^3}$[117]. It can exceed the density of pure glaze ice. This is due to the higher density of the liquid water embedded in the snow. Locally it can have up to 50 % of liquid water content in the snow body [125].

Figure 2.3: Wet snow accretion on a transmission line [86]. (with permission of Thierauf, photo: Stehr, 2005)

2.2.4 Glaze Ice

Glaze ice is usually smooth, dense and transparent. It is formed by freezing rain or drizzle at a temperature of about 0 °C [117]. Thus, generally speaking, it is precipitation icing, but it may also occur as in-cloud icing. Obviously, it can also occur as a result of ice and snow deposits melting and again freezing. The ice is clear, smooth and dense, because the latent heat released during freezing process is not dissipated completely and a liquid layer forms. Dendrite ice crystals grow slowly into the liquid layer leading to a high density. The density can reach 917 $\mathrm{kg/m^3}$ for bubble free ice, but commonly some air is embedded and thus its density is somewhat lower. The temperature at the ice surface remains at 0 °C. Meteorological conditions for glaze ice formation usually show high liquid water content in the air and freezing rain with droplets ranging from 0.5 to 4 mm [61, 103].

2.2.5 Icicle Growth

Icicles can appear in many forms and sizes, with corrugated or smooth surfaces, pointed or blunt. Lenggenhager described the various types of icicles and their growth mechanism [68]. Icicles are actually a form of glaze ice with the same characteristics as other types of glaze. Never the less they are treated here as an individual paragraph, because of their

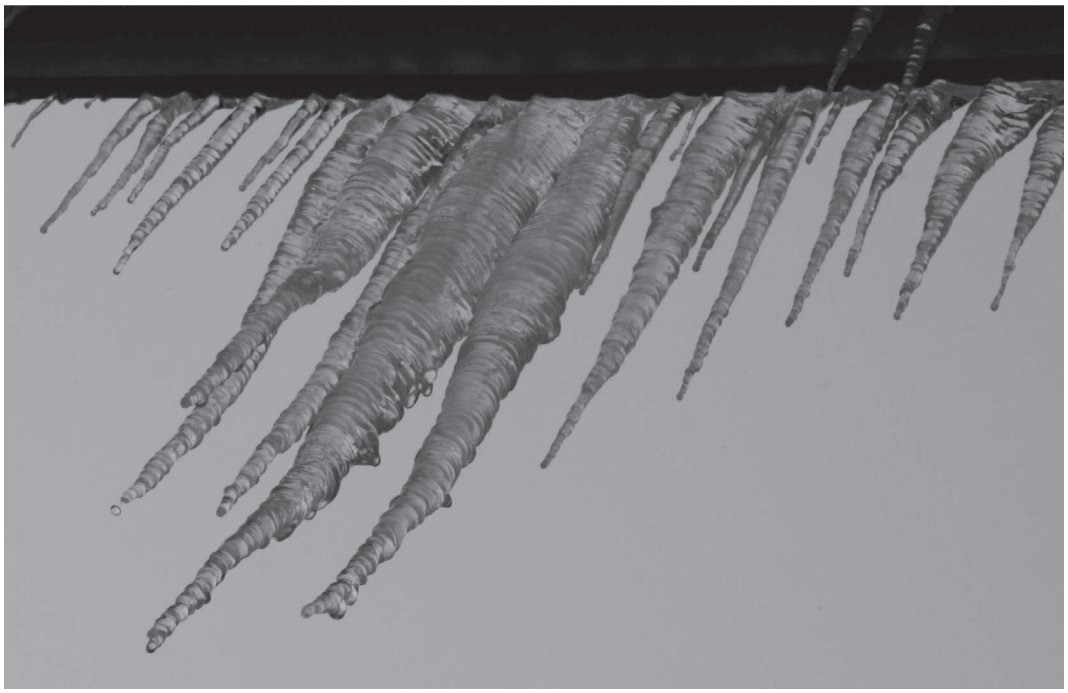

Figure 2.4: Glaze ice in form of icicles growing at a roof rail. (Photo: Wagner, 2009)

growth mechanism and because they can cause significant static ice loads. Experiments in freezing precipitation showed that 46 % of the total ice mass was contributed by icicles [84]. Furthermore they can catch significant wind loads due to their longitudinal extension. When an icicle forms a liquid film covers its surface. Due to gravity and wind drag this film flows towards the icicle's tip and forms a pendant drop. Hence, icicle grows mainly at the tip. The growth mechanism clearly illustrates this to be an example of glaze ice formation and therefore a model for icicle formation is presented in section 2.4.

2.2.6 Natural Precipitation

The characteristics of natural precipitation are important for atmospheric icing, since we focus here only on the consequences of this meteorological phenomenon some authors and their work are presented that deal with the meteorological aspect of atmospheric icing. Diem [23] and Waibel [162] investigated incloud icing and found already in the 1950s, that tandem arrangement of cylinders affect the shape of ice deposits. Best studied drop size distributions of rain and drizzle [7]. Although the study is not in particular on icing events, the results are valid for freezing rain and drizzle. In the same field is the work of Marshall et al. on precipitation trajectories and measurements of drop size distribution [88, 89, 90]. Hitschfeld et al. examined the development of size distribution during fall of rain drops [44]. Characteristics of snow fall are described by Mellor and Mellor [97], for example. Further details on the occurrences

mechanisms and the meteorological background of natural precipitation are given by Mason [91]. Meteorological studies, such as the above mentioned, are used to build the test setup of small scale icing experiments in climatic wind tunnels. The simulation of natural precipitation in wind tunnel experiments is not an easy task. Therefore analysed Kollar et al. multiphase flows of air and artificial precipitation in wind tunnel experiments. Their studies focused on the effect of droplet-droplet collision [60], evolution of droplet size distribution [59] and also on evaporation and turbulences [62] in wind tunnel experiments.

2.3 Modelling Atmospheric Icing

There are many different approaches for modelling ice accretion. Not all of these account for every aspect. Even though the approaches may seem to be rather different and use diverse terms, the underlying principles are the same. Diem [23] and later Makkonen [82] described the fundamental mechanism of ice accretion. The simple but fundamental model structure developed by Makkonen is also used in advanced icing models. The complexity of advanced models arises from more sophisticated treatment of individual model elements. A flow field calculation with computational fluid dynamic (CFD) models, for example. To give an overview of the current state of ice accretion modelling we look in the following section at the principles and assumptions of various icing models. For many engineering applications not only the static ice load is important, but also the influence of ice deposits on aerodynamic behaviour. To illustrate the icing mechanism it is useful to neglect the shape of the ice body, focusing on the change of accumulated ice mass over time, called the icing rate. Accounting for time dependent changes of geometry during the icing process is a challenging task as we will see in later sections.

The maximal possible icing rate is defined by the maximum amount of icing particles per unit projection area of an object exposed to the particle flux. Consequently the flux density is given by:

$$F_p = LWC \cdot u_{p,0} \tag{2.1}$$

where LWC is the liquid water content in the air and $u_{p,0}$ is the particle velocity in undisturbed flow. Hence the maximal possible icing rate is calculated by:

$$\left(\frac{dm_i}{dt}\right)_{\max} = F_p \cdot A \tag{2.2}$$

where m_i is the mass of ice and A is the projection area of the iced object perpendicular to the particle flux. Considering real icing conditions not all particles passing the projection area contribute to the ice formation. In order to achieve a realistic icing rate diminishing effects

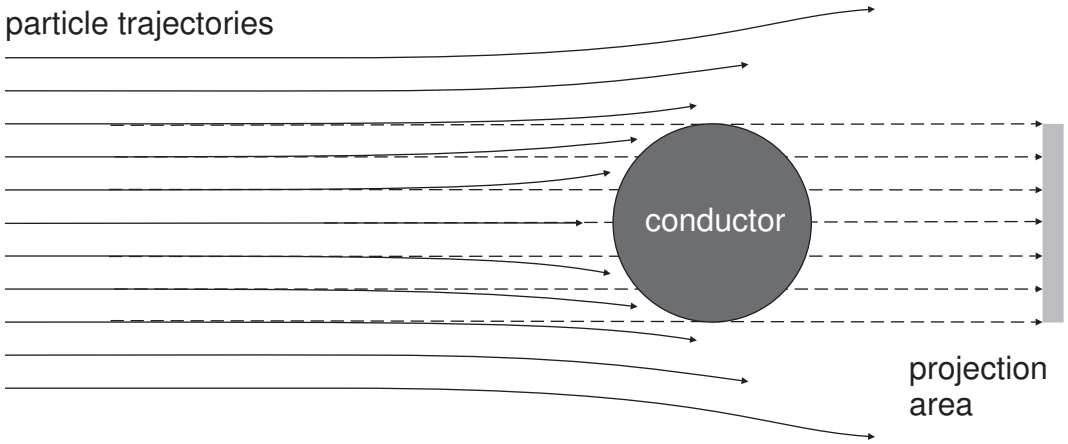

Figure 2.5: Collision efficiency.

are incorporated via three parameters varying from one to zero. Leading to the following expression for reduced icing rate:

$$\frac{dm_i}{dt} = \alpha \cdot \beta \cdot \chi \cdot F_p \cdot A \tag{2.3}$$

where α is the collision efficiency, β collection efficiency and χ accretion efficiency.

The collision efficiency is the fraction of particles impinging on the object compared to those that would pass the projection area in an undisturbed flow. The icing rate decreases due to particles being dragged around the object by the air flow (cf. figure 2.5). It is governed by air flow, particle drag and inertia. Consequently particles with a sufficiently large inertia have a collision efficiency of one.

The collection efficiency is the ratio of incoming particles, which end up sticking to the surface compared to all impinging particles. Those which do not stick bounce from the surface. Particles which do not freeze contribute only to the heat balance. Particles that do freeze take part in the heat balance and contribute directly to the ice formation (cf. figure 2.6). Hence, when all particles stick to the surface the collection efficiency is one. Sometimes the collection efficiency is also called sticking efficiency.

The accretion efficiency accounts for particles that stick on the surface and do actually freeze. It equals one, when all particles freeze. It decreases when the heat flux is too small and not all particles solidify. Remaining particles form a thin liquid layer on the surface. The surplus of unfrozen water is partially dragged off due to gravity or wind (cf. figure 2.7).

The icing process is a complex phenomenon. Just as the boundary conditions vary on a larger scale, the small scale structure of ice formation can vary significantly. When droplets freeze instantaneously on impact the ice accumulation is a rather two-dimensional process. But when the equilibrium of freezing and melting is sensitive or the mass flux on the surface is not more or less perpendicular to the surface, a complex three-dimensional ice structure forms [61].

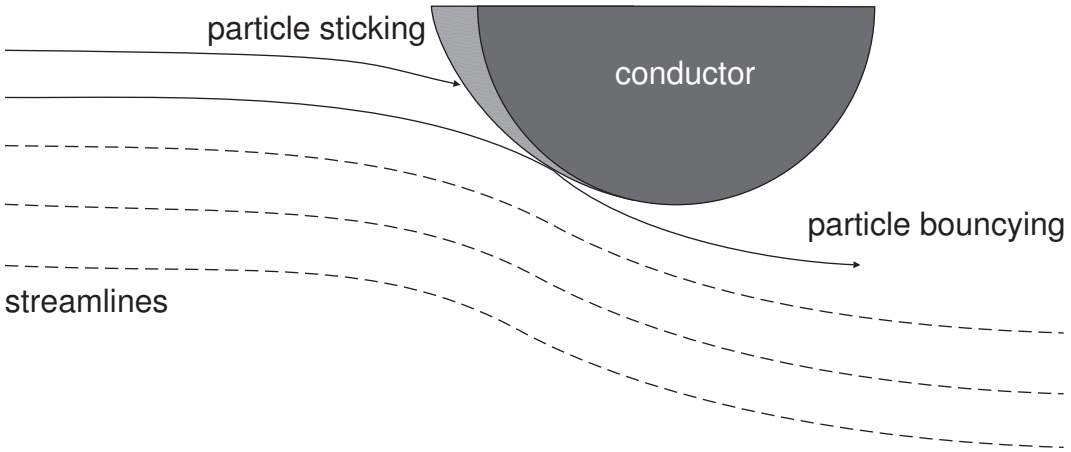

Figure 2.6: Collection efficiency.

In order to reduce the complexity of the model assumptions are made. The collision efficiency is often assumed to be one in simple models. Even so it is only a good approximation for larger freezing rain drops. The collection efficiency of supercooled cloud droplets is always presumed to be one for dry icing conditions, because the droplets freeze directly on impact. Regarding atmospheric icing of structures like lattice towers or cables dry snow or hail are assumed to bounce off from the surface and therefore contribute not to the ice accumulation. Hence the collection efficiency is presumed to be zero. On large roof structures however these precipitation types need to be taken into account, because they can bounce and still remain on the roof. Droplets of freezing rain splash on a surface. The mass loss depends on the impact angle and therefore the collection efficiency varies between zero and one. In case of wet snow is the collection efficiency within the same range, whereas here it depends also on the impact speed. The accretion efficiency in case of dry ice growth per definition is equal to one. Wet growing conditions are not easy to describe by elementary considerations, because here the freezing mechanism is very sensitive to boundary conditions. Consequently, simplifications put significant constrain on possible results. One attempt is to assume accretion efficiency of one. Meaning that no water shedding is considered, the formation of icicles is neglected.

As a next step let us now look at assumptions and improvements of diverse icing models that are presented in the literature. An early and very basic model by Imai proposed an equation to estimate the ice load on a conductor in freezing rain, which depends only on wind velocity and temperature ([45] from [81]). The precipitation intensity was not considered at all. Another basic model for glaze ice formation developed by Lenhard is only based on the precipitation intensity. But it showed poor correlation of ice load and precipitation intensity ([69] from [81]). As mentioned before, not only the ice load is difficult to estimate but even more to modelling geometrical changes due to ice deposits poses even more difficulties. Makkonen for example assumed that the ice accumulates evenly around a conductor [77]. It keeps a cylindrical cross-section and the icing rate is parameterised with geometry variables. Another

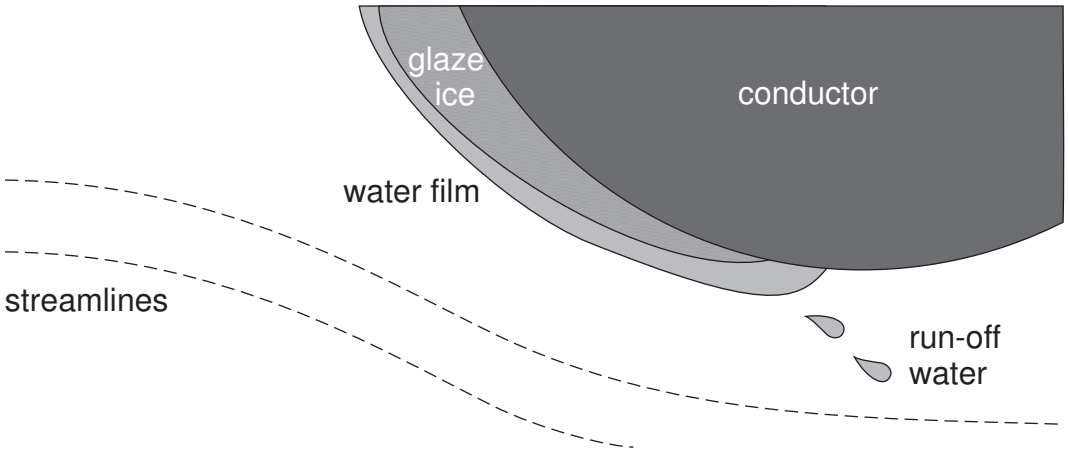

Figure 2.7: Accretion efficiency.

way to simplify the model was used by Lozowski et al. [71]. They calculated the initial icing rate of a blank cylinder and extrapolated it over time to simulate the growth of an ice deposit.

McComber accounted for the changing geometry by calculating the collision rate in reference to the impact angle of impinging droplets, which changes with a growing ice deposit [93]. This was also the first approach to account for torsion of a single conductor due to eccentric ice load. Skelton worked on the effect of torsional stiffness of the conductor on rime ice accretion [137] and effects of counter weights [136], restraining torsion in order to reduce the total ice load. Later torsional effects where also modelled for wet snow accretion, where it leads to characteristic snow sleeves [119, 120, 138].

The collision efficiency is assumed to be one in simple models [40, 49, 50, 81], which is accurate when the particle trajectories are insensitive to changes in the flow pattern. When for example relatively large particles stream on an object of small size at moderate flow velocities, the particle trajectories are hardly deflected. Earlier McComber [95] and Lozowski et al. [71] successfully used an empirical equation, fitting experiments by Langmuir and Boldgett [66] on droplet trajectories to define the collision efficiency. The same approach was adopted to calculate the droplet trajectories for a stochastic model aiming to investigate the rime-feather growths occurring under low impact rates and dry growing conditions [39]. Even though the model is based on limiting assumptions it successfully explained feather like structure of soft rime ice. Advanced models simulate the particle flux as a multiphase flow. The majority uses a one-way coupled two-phase flow scheme. First, the flow field is calculated, then based on the solution the particle motion is determined. The flow field is either described by potential flow [37, 67] or the Navier-Stokes equation [38, 110, 161, 168]. The particle motion is commonly calculated with a Lagrange approach [38, 158, 168]. Naterer developed a model with a Eulerian approach, which is numerically more efficient but less often used [106, 107]. This is due to considerations regarding the volume fraction of droplets in the air flow. More details on this subject are given in the section 3.3. It is often assumed, that the droplet spectra of natural

precipitation can be simplified sufficiently by the use of characteristic particles [32, 33, 35]. Significantly more costly are models, where the whole droplet spectrum is considered. This effort is made for aircraft icing models for example, where an impact of individual fractions of droplet the spectrum can be identified [168]. Aircrafts are vulnerable to icing, because the ice deposit reduces the buoyancy of the airfoil.

The collection efficiency is commonly modelled with different approaches depending on the precipitation type. In general cloud droplets are considered to have a collection efficiency on conductors of one [82]. Even advanced models for aircraft icing reduce the collection efficiency only globally by the cosine of the angle of attack of the airfoil [168].The collection efficiency of freezing rain and drizzle is often not modelled explicitly in simple models [40, 49, 50, 81], but they imply a collection efficiency of one. Improved conductor icing models account for splashing of rain drops when they impinge of the surface. The cosine of the impact angle has proved to be a good measure not only for freezing rain drops but also for wet snow flakes [117, 121]. Moreover, investigations by Admirat showed that the collection efficiency is also reciprocally proportional to the impact velocity of the flakes [3].

The heat balance governs the accretion efficiency. Modelling ice formation at low temperatures is therefore easier than modelling icing processes around the melting temperature of ice. The first leads to dry growth and therefore to an accretion efficiency of one. The latter requires a calculation of the sensitive equilibrium of liquid or frozen water governed by the heat balance. In order to avoid the calculation of the heat balance simple models assume an accretion efficiency of one, not only for dry but also for wet ice formation. They neglect shedding of water and in return are not taking icicle formation into account [81]. The first scheme to calculate the heat balance of ice deposits was presented by Messinger [98]. The two dimensional model was developed to estimate the ice accretion on airfoils. Makkonen presented the first conductor icing model accounting for the global heat balance [76, 77, 85]. Szilder et al. developed a model which calculates the local heat balance of ice deposits on conductors [148, 149]. They account for different properties of dry and wet icing conditions and also for the transition from dry to wet ice formation. The film of unfrozen water occurring in glaze ice growth is not modelled explicitly. They use the heat balance as a measure to restrict the ice evolution and to define the ice density. Fu developed a two dimensional model, where the liquid water film is treated as a continuous, thin layer moving from the stagnation point towards the edge of the surface [35]. A particular aspect linked to the sensitive equilibrium of the freezing water film is considered in morphogenetic models [146, 147]. Even with equal boundary conditions the accretion shape can differ significantly in experiments. Morphogenetic models try to account for this with stochastic modelling of film distribution and local freezing. However, the formation of rivulets on the surface has an important influence on the heat balance and liquid layer distribution. To model it accurately, complex three dimensional simulations of the freezing process are necessary. So far, it is only implemented in aircraft icing models, since it is computationally expensive [99, 100]. Moreover, when even smaller scales are resolved, such as splashing and solidification of a single droplet, the investigation of icing processes on

structures becomes impossible due to a lack of computational resources [174]. During snow accretion, when the wet snow hits a surface, it undergoes a rapid change. The conglomerate of ice crystals, air void and moisture adhere to the surface by ice bond and capillary forces of the liquid water in the snow deposit [122].

A number of different models describe the heat balance of snow accumulations on a single conductor and are verified by field observations and experiments [2, 41, 118, 171]. Another important aspect of estimating the load from wet snow or ice is the shedding of the deposits from the cables. Also here the heat balance and with it the liquid water content of the accumulation are the governing factors [125, 126, 127]. However, the model resolution and complexity have not yet reached the level of models used in aircraft icing. In general those models account only for in-cloud icing, but they consider the whole droplet spectrum important for aircraft icing. For the icing of structures however, the treatment of all major types of precipitations is important in icing of structures.

To summarise, collision, collection and accretion efficiency are modelled in various approaches leading to equivalent conclusions. Glaze ice formation fed by rain drops with high inertia is barely affected by the collision efficiency. But due to splashing of the rain drops the collection efficiency has an influence on the glaze ice growth. Rime ice accretion on the other hand is mainly affected by collision efficiency, due to cloud droplets with low inertia, and not by the collection efficiency, which is equal to one. Hence, some approaches merge collision and collection efficiency to a catch efficiency instead of defining them separately. Wet snow accretion is affected by collision and sticking. Furthermore, modelling accretion efficiency of glaze ice, wet snow or transition from rime to glaze ice requires an adequate treatment of the heat balance.

Conductors and airfoils are not the only structures for which ice accretion models are developed. Zavarian et al. for example derived a method based on observations to estimate ice loads on high structures. They found a correlation between altitude above sea level and the ice load [172, 173]. Never the less, there are many uncertainties when estimating ice loads on high structures. Therefore, Peil et al. investigated different ice loading scenarios in a parameter study [111]. The complexity of icing and melting processes is illustrated by comparing attempts to describe ice loads on lattice towers with measured data. Figure 2.8 shows a TV tower in Sweden, with measured and predicted ice loads. It highlights limits of simplifying assumptions, numerical procedures and transfer of meteorological data to models.

Meteorological models that use standard parameters like precipitation rate, temperature and wind speed are very limited in predicting ice accretion especially for long icing events [94]. These models operating on large scales are not suitable to reliably estimate extreme ice loads on structures, but they are useful to give a qualitative estimate of ice loads and return periods of ice events at certain locations.

On a smaller scale than meteorological models are investigations of snow drift. They simulate wind driven snow transport in complex terrain as for example around a number of low-rise

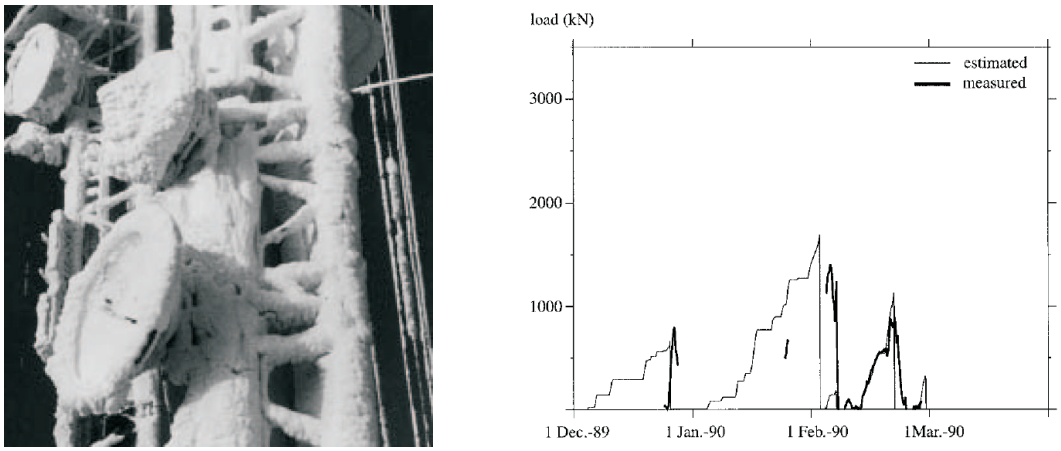

Figure 2.8: Iced TV tower in north Sweden (left) and estimated and measured ice loads (right) [145]. (with permission of the American Meteorological Society)

buildings [8]. Here the salutation and transport process of snow flakes is incorporated in CFD codes [9]. Another field of interest is the stability of snow avalanches, which is also investigated by numerical models [144].

Closer to aircraft and conductor icing are new models investigating losses in energy production of wind turbines [5, 38]. Ice accumulation on rotor blades can reduce their efficiency significantly. Here, the icing process is not modelled, but the influence on the aerodynamic behaviour of ice accumulation is under investigation. The task is challenging and even though the models are using sophisticated CFD codes main outcomes are of rather qualitative nature only. For example, that icing on the tip of the blade has a higher impact on the energy production [5], which can also be found using less demanding aerodynamic calculations. Another recent study investigated the aerodynamic behaviour of transmission lines in various types of conductor bundles under wind action, but without looking into the effect of ice deposits [124]. Even though conductor bundles are frequently used to significantly increase the power capacity per line, their aerodynamic behavior is not fully understood. The aim of future research should be to combine such a dynamic transmission line model with the analysis of ice deposits on conductor bundles presented here.

However, the variety of assumptions and simplifications reflect the field where the models are applied to.

2.4 Icicles Formation

2.4.1 Growing of Icicles

The formation of icicles is a good example to illustrate the process of ice evolution in wet growing conditions. Formation of icicles is often neglected when icing of structures is investigated. Even though they contribute significantly to the ice load. Moreover, they increase the collection area for precipitation, which leads to an increasing icing rate [81]. Especially in extreme icing events loads are therefore significantly underestimated [82]. A side from static and dynamic loads, the icicles can also cause flashovers when they form on isolators of transmission lines [79]. Icicles form under freezing precipitation or due to freeze and thaw cycles of larger ice deposits. The ice evolution is fed by a flux of supercooled water on the surface of the icicles. It is either collected on the icicle itself due to precipitation or arrives at the icicle root as discharge of other collectors such as a roof for example. If sufficient water is present a liquid film of supercooled water develops. Gravity and wind drag drive the water towards the icicle tip, where it forms a pendant drop. Unless the water flux is very small the film covers the entire surface. It usually has a thickness of 40 to 100 µm ([74] from [73]). The pendant drop at the tip grows as more water flows down. When it reaches a certain size it strips and a new drop can form. Experiments showed that under calm wind conditions the diameter of the pendant drop lay between 4.8 to 5.0 mm, regardless of the growing conditions ([75] from [73]).

Icicles form under wet growing conditions. The growth is proportional to the heat loss. Since icicles grow mainly in the longitudinal direction, the main heat loss must occur at the tip. To freeze the liquid water running down the icicle the latent heat released during freezing must be dissipated. This occurs manly due to thermal convection and evaporation. Heat loss from radiation is very small and heat conduction within the ice is negligible [79]. The thin water film on the icicles surface is supercooled and therefore any changes in the film temperature can not contribute significantly to the heat transfer. Compared to that, the heat flux at the surface of the pendant drop is significant. Figure 2.9 shows the cross-section and heat flux of an icicle.

The icicle's tip grows into the pendant drop. First, ice crystals form a thin tube filled with liquid water. The thickness of the wall is 0.1 mm or less ([74] from [73]). Then the water inside the tube slowly solidifies.

While the icicle grows lengthwise, a fraction of the water film freezes on its way to the tip and slowly contributes to the radial growth of the icicle. The liquid water inside the icicle cannot transfer heat to the tip or radially to the walls, because there is no temperature gradient. The wall and the tip covered with a film of supercooled water are at freezing temperature and thus the entrapped water can only freeze by conducting heat to the root of the icicles. Consequently the liquid water freezes slowly from the root to the tip [73]. This process has a negligible effect on the longitudinal and radial accretion and thus it is insignificant for the heat balance at the

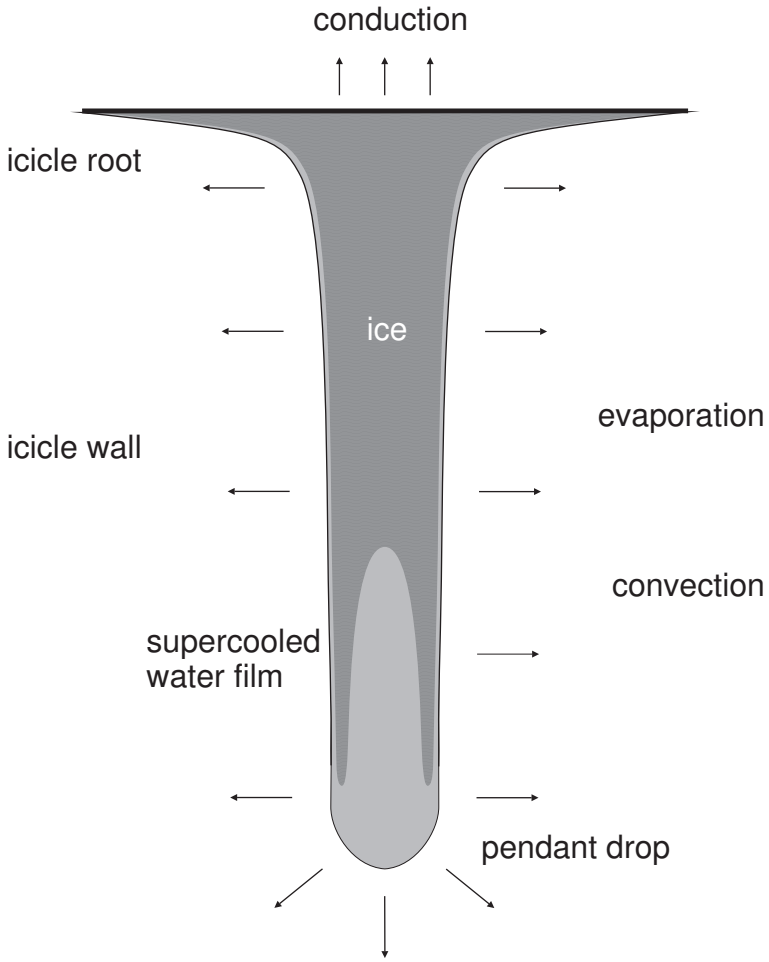

Figure 2.9: Schematic cross-section of an icicle, where dark areas denote liquid water and lighter areas resemble ice.

tip or the surface. To summarise the icicle growth shows three main processes, longitudinal and radial growth and inward radial freezing.

However, icicles require continuing conditions to form. If the supply of supercooled water is very high it is unlikely that the icicle will grow very large. It starts growing slowly, because the latent heat of freezing is only partially dissipated. In the contrary case of a low water supply, from a certain point on no water reaches the tip and consequently no further elongation of the icicle is possible. Therefore very large icicles form under conditions where the water supply rate increases with time [73, 79]. That makes it very important to account for the collection of droplets by the icicle itself, since water supply from droplet collection increases as the icicles grows, even more so in conjunction with higher wind speeds [82].

2.4.2 Spacing of Icicles

Often a number of icicles form side by side. In order to estimate the impact of icicle formation on structures, the spacing is an important issue. The total ice and wind load as well as the growth rate are affected significantly by the icicle spacing. The discharge of supercooled water at the root of the icicles is inversly proportional to the number of icicles per unit length. Since a small rate of water supply promotes the initial icicles growth, the total ice load increases with decreasing icicles spacing. Once the icicle formation has started an increase of the water flux will further intensify the icicles growth. Given that the icicles themselves collect droplets and therefore the water supply increase with grows, the prediction of icicle spacing is essential. Experiments in freezing precipitation by Makkonen and Fujii [84] showed that 46 % of the total ice mass were contributed by collection on the icicles themselves. There are two different theoretical approaches for estimating icicle spacing. Both have been verified in experiments and are briefly presented here.

Makkonen and Fujii presume that the icicles originate from pendant drops and that their spacing is governed by the spacing of pendant drops when the icicle formation starts [84]. The equilibrium of gravity and surface tension acting on a pendant water film governs the spacing. This approach predicts an initial drop spacing of 21 mm. In the experiment the cable had a diameter of 22 mm. The results indicated that for practical application icicle spacing of 22 ± 30 mm is a reasonable assumption. Furthermore, the spacing seems to be insensitive to air temperature (-4.2 to $-1.2\,^{\circ}$C) and wind speed ($1 - 10\,$m/s) in the given range. Also the cable diameter is of little importance. Both a diameter bigger than the pendant drop and a wire with a diameter of 4 mm showed the same spacing of icicles. No significant differences in spacing where observed between stranded wires and smooth cable either. Once icicles grow the spacing does not change and only rarely new icicles form between already existing one. A loss of a pendant drop form the icicles due to wind drag was not observed in the experiments. But higher wind velocities might have an impact on the loss of water. In general under conditions of high wind speed icicles form an elliptical cross-section and the longitudinal axis is parallel to the wind direction. Due to strong winds several icicles can grow into a uniform ice body. On hydrophobic surfaces the growth rate was found to increase faster in the beginning, once the icicles forms. It is due close spacing of to pendant drops on such a surface developing longer and narrower icicles. Consequently, hydrophobic coating on power lines could therefore even result in higher ice loads.

The other approach to explain the spacing of icicles is based on the Rayleigh-Taylor instability of a thin water layer attached to the underside of a solid substrate [10]. The system is instable having a denser fluid (water) above a less dense fluid (air) and gravity acting downwards. The initial state where the fluids are motionless is instable, because the energy level of the system is reduced when the denser fluid descends and the less dense fluid rises. The transition to a more energy efficient, and hence stable state, is initiated by perturbations of the interface between the fluids. Small perturbations are stabilized by the surface tension, but at a certain wavelength

Figure 2.10: Icicles growing at a roof edge. (Photo: Wagner, 2009)

the perturbation grows rapidly. Therefore, the surface becomes rippled with a periodicity of the largest mode of the so-called Rayleigh-Taylor instability. In case of freezing water the periodically rippled surface is the root of the icicles. Assuming that the water has the water having a temperature of 0 °C the spacing of the icicles is calculated to 24.7 mm, which is in reasonable agreement with the experiment by Makkonen and Fujii [84].

However, all these considerations are based on generic assumptions, which may differ from real settings. In a way that icicles may merge or bend as it is shown in figure 2.10. For practical application it is reasonable to assume 45 icicles per meter [81]

2.4.3 Modelling Icicle Formation

The presented two-dimensional model is based on the work of Makkonen [79] and Maeno et al. [73]. It simulates the evolution of a single icicle in moderate wind conditions. Based on the considerations of the previous section, radial and longitudinal icicle growth are modelled separately. The lengthwise growth is governed by the heat balance at the surface of the

pendant drop and the radial growth depends on the heat balance at the wall of the icicles. Heat conduction at the icicle root is neglected. Longitudinal and radial growth are simultaneously solved to simulate the icicle formation.

Heat Balance at the Pendant Drop

The heat balance depends on the time the pendant drop remains at the tip as well as its size and shape. Experiments have led to the following expressions to estimate drop radius and dripping frequency [73]. The shape is assumed to be hemispherical. The drop radius depends on the water supply rate and is then calculated by:

$$d_d = 0.0196 \cdot W + 4.66 \tag{2.4}$$

where d_d is the diameter of the pendant drop and W is the water supply rate. The dripping frequency is given by:

$$f_d = 0.0166 \cdot W + 0.0281 \tag{2.5}$$

In the experiments the drops remained 2-14 seconds at the tip. Over this time interval defined by the dripping frequency is the heat balance is defined as [79]:

$$q_c + q_e + q_r = q_{drip} + q_f \tag{2.6}$$

where q_c, q_e and q_r are heat transfer due to convection, evaporation and radiation. The heat flux due to dripping of pendant drops is q_{drip} and q_f is the heat flux due to freezing.
In the following the individual heat fluxes are defined, starting with the convective heat transfer, which is given by:

$$q_c = h_t \cdot (0\,^\circ\mathrm{C} - T_a) \tag{2.7}$$

where h_t is the convective heat transfer coefficient at the drop surface and T_a the ambient air temperature. The heat transfer coefficient is derived and explained in more detail in the appendix A. Heat flux due to evaporation is defined as:

$$q_e = h_t \cdot \frac{0.622 \cdot L_e}{c_p \cdot p_a} \cdot (e(0\,^\circ\mathrm{C}) - e(T_a)) \tag{2.8}$$

where L_e is the latent heat of evaporation at $0\,^\circ$C, $e(0\,^\circ\mathrm{C})$ and $e(T_a)$ are the saturated water vapour pressure at $0\,^\circ$C and at ambient temperature. The specific heat of water is c_p and p_a is the air pressure. Sublimation, which is the transition of ice directly to water vapour, is neglected. The heat transfer due to radiation is very small here it is approximated by:

$$q_r = 8.1 \cdot 10^7 \cdot \sigma \cdot (0\,^\circ\mathrm{C} - T_a) \tag{2.9}$$

where σ is the Stefan-Bolzmann constant. Emissivity from the tip to the environment is assumed to be one and solar radiation is not considered at all. The heat loss due to the temperature change of the water forming the pendant drop until it strips is given by:

$$q_{drip} = \frac{2 \cdot c_p \cdot W_t \cdot \Delta T}{\pi \cdot d_d^2} \tag{2.10}$$

where W_t is the mass flux of water reaching the tip of the icicle, ΔT is the change in temperature of the pendant drop. The water flux reaching the tip of the icicle depends on the flux at the root of the icicle W_r and on the mass flux collected by the icicle itself W_w. The latter contributes significantly to the growth rate and was not accounted for in the original model [81]. Subtracting the losses due to evaporation and freezing of the water film on its way to the tip leads to the following expression for the water supply rate at the tip:

$$W_t = W_r + W_w - \pi \cdot d_i \cdot l_i \cdot \left[\frac{\rho_s}{2} \cdot \frac{dd_i}{dt} + h_t \cdot \frac{0.622}{c_p \cdot p_a} \cdot (e(0\,^\circ\mathrm{C}) - e(T_a)) \right] \tag{2.11}$$

where d_i is the mean icicle diameter and l_i is the length of the icicle. The other unknown parameter is the temperature of the pendant drop. It is defined by:

$$\begin{aligned} \Delta T &= 0.568 \cdot 10^{-5} \cdot \left(\frac{dl_i}{dt} - \frac{1}{2} \cdot \frac{dd_i}{dt} \right)^{0.943} && for && 0.2\,^\circ\mathrm{C} \geq \Delta T > 0.05\,^\circ\mathrm{C} \\ \Delta T &= 1.070 \cdot 10^{-4} \cdot \left(\frac{dl_i}{dt} - \frac{1}{2} \cdot \frac{dd_i}{dt} \right)^{0.478} && for && \Delta T > 0.2\,^\circ\mathrm{C} \end{aligned} \tag{2.12}$$

The heat flux due to latent heat of fusion at the tip is:

$$q_f = \frac{2 \cdot L_f \cdot \rho_i \cdot d_{dend} \cdot (d_d - d_{dend})}{d_d^2} \cdot \frac{dl_i}{dt} \tag{2.13}$$

where L_f is the latent heat of fusion, ρ_i is the ice density, d_{dend} is the thickness of the dendritic ice at the tip is assumed to be 75 µm. An exact calculation has an negligible effect on the result and is therefore omitted [73].

2.4.4 Heat balance at the Icicle Wall

In order to simplify the calculation of the heat transfer via the wall of the icicle it is approximated as a circular cylinder. The diameter of the cylinder represents the mean diameter of the

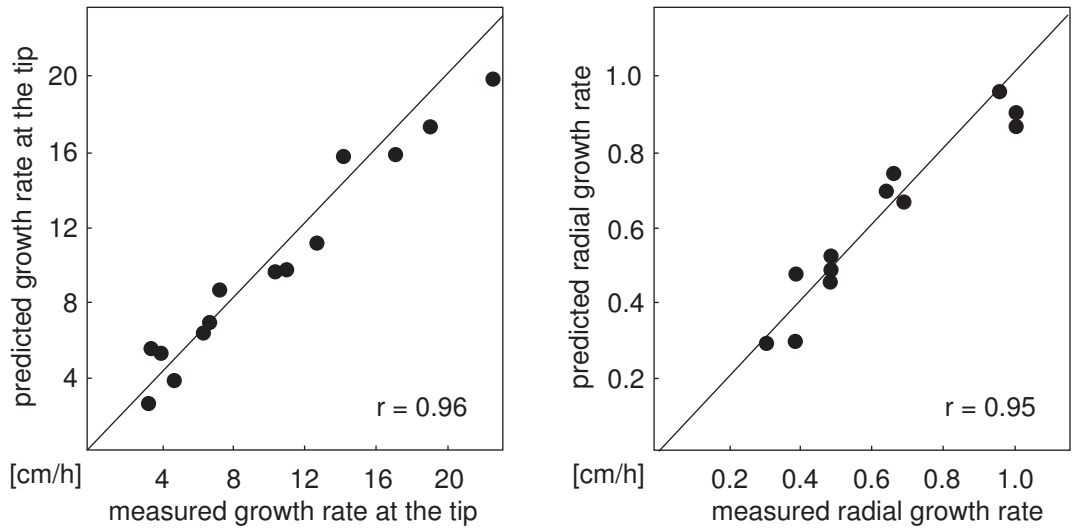

Figure 2.11: Predicted and measured longitudinal (left) and radial (right) icicle growth [79]. A correlation coefficient of 0.96 and 0.95 proves good agreement of experimental results and theoretical approach.

icicle, which is not necessarily equal to the diameter at mid span of the icicle.
The heat balance at the wall of the icicle is defined by [79]:

$$q_c + q_e + q_r = q_f \tag{2.14}$$

The convective heat transfer at the wall is identical to the at the tip in spite of the different heat transfer coefficient and therefore it is computed by:

$$q_c = h_w \cdot (0\,^\circ\mathrm{C} - T_a) \tag{2.15}$$

where h_w is the convective heat transfer coefficient of a cylinder. The heat transfer coefficient is explained in more detail in the appendix A. Also the heat transfer due to evaporation heat differs only in reference to the heat transfer coefficient:

$$q_e = h_w \cdot \frac{0.622 \cdot L_e}{c_p \cdot p_a} \cdot (e(0\,^\circ\mathrm{C}) - e(T_a)) \tag{2.16}$$

The heat flux due to radiation is approximated by equation 2.9. The heat transfer due to latent heat release during freezing of the water film on the icicle surface is defined as:

$$q_f = \frac{1}{2} \cdot \rho_s \cdot L_f \cdot (1 - \lambda) \cdot \frac{dd_i}{dt} \tag{2.17}$$

where ρ_s is the density of spongy ice and $\lambda = 0.26$ the fraction of liquid water within the ice. When ice grows under a supercooled water film it entraps unfrozen water. The fraction

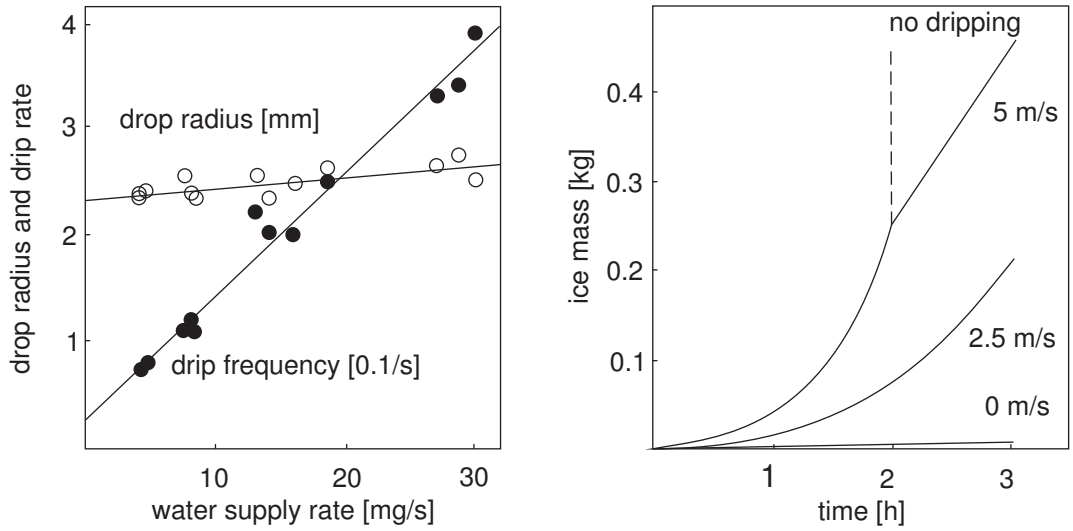

Figure 2.12: Dripping frequency and drop radius versus water supply rate (right) at various temperatures (-4 to $-21\,^{\circ}\mathrm{C}$) at an icicle tip [73]. Simulated ice mass at various wind speeds (left) at an air temperature of $-5\,^{\circ}\mathrm{C}$, humidity of $80\,\%$ and water supply rate of assumed $50\,\mathrm{mg/s}$ [79].

is presumed to be independent of the growing conditions. The density of the spongy ice is calculated by:

$$\rho_s = \lambda \cdot \rho_w + (1-\lambda) \cdot \rho_i \tag{2.18}$$

where ρ_w is the density of water.

Simulation of Icicle Growth

Rearranging the equations of heat transfer at the tip and at the icicle wall leads to the following expression for longitudinal and radial growth.

Longitudinal Growth:

$$\frac{dl_i}{dt} = \frac{q_c + q_e + q_r - q_d}{2 \cdot L_f \cdot \rho_i \cdot d_{dend} \cdot (d_d - d_{dend}) \cdot d_d^{-2}} \tag{2.19}$$

It is important to notice that the heat flux due to dripping of the drop depends on dl_i/dt and dd_d/dt included in the definition of ΔT and W_t. Both are taken from the previous time step.

Radial Growth:

$$\frac{dd_i}{dt} = \frac{q_c + q_e + q_r}{\frac{1}{2} \cdot \rho_s \cdot L_f \cdot (1-\lambda)} \tag{2.20}$$

Here the heat transfer coefficient h_w depends on length and average diameter of the icicle. Therefore the model requires simultaneous solving of both equation 2.19 and 2.20.

The results of the model showed good agreement with experimental results over a wide range of water supply and temperatures values [81]. But the model does not account for higher wind speeds, where icicles are expected to bend and deform. Recent investigations incorporate also boundary layer effects on the formation of rippled icicle surfaces [152]. But these effects are of a more descriptive nature and of minor importance for understanding the process of icicle formation. Another interesting approach to model icicle growth are morphogenetic models [146]. They account for geometry variation of icicles that occurs in spite of identical boundary conditions, since the growth mechanism here is based on statistical considerations. This highlights a major challenge of modelling wet ice growth. It is difficult to determine the flow direction of a water film or the formation of rivulets, when the boundary conditions do not define the direction clearly. In case of icicle formation at moderate wind velocities the water flows due to gravity down to the tip. But at higher wind velocities this assumption is not valid any more.

2.5 Dynamic Behaviour of Transmission Lines

Transmission line vibrations can arise from wind action alone, from wind in interaction with ice deposits or even when ice is shed from a conductor. The oscillations may cause flashovers or twisting of conductor bundles. Furthermore, the dynamic loads on conductors, ground wires, insulators and towers can eventually cause fatigue damages. From an aerodynamic point of view conductors are considered as bluff bodies. The separation of the boundary layer forms a distinct wake. Their low inertia and self-damping makes them prone to aeroelastic instabilities such as vortex induced vibrations, galloping and wake induced oscillations. These phenomenons are studied experimentally, by field observations and theoretically since decades. The fundamental mechanisms are understood, but some problems are still not completely understood as for example galloping of iced conductor bundles. The following passage provides an overview of dynamic behaviour of transmission lines due to wind and ice action, damages occurring and mitigation strategies.

2.5.1 Vortex Induced Vibration of Conductors

Aeolian vibrations are an aerodynamic instability. Vertices shed in the wake of the conductor according to the flow field, which causes pressure fluctuations on the conductor surface. When the shedding frequency is close to the natural frequency of a conductor, resonance can lead eventually to oscillations. Once the conductor is in motion it interacts with the flow field. In consequence the oscillation can change due to changes in the flow field. This effect can even

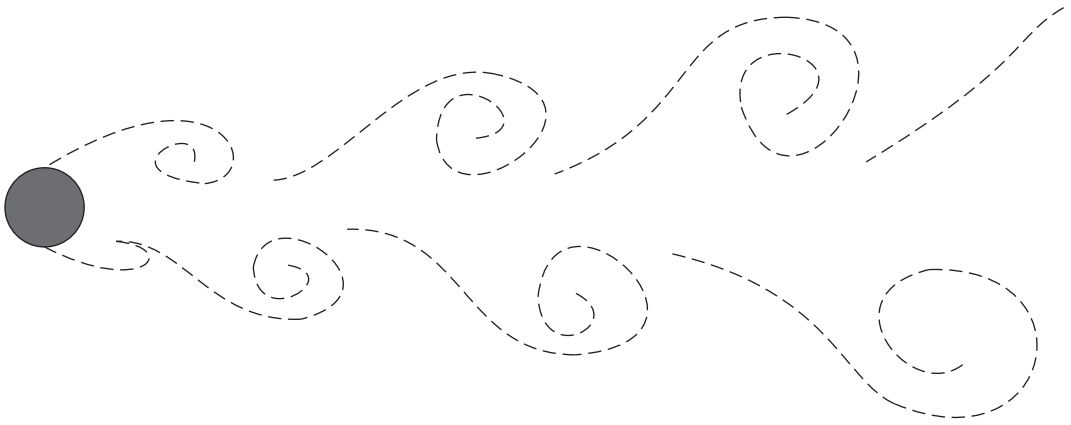

Figure 2.13: Vortices shedding from a cylinder in a so-called vortex street.

sustain the conductor movement when the flow velocity leaves the critical range. This effect is termed as lock-in. Amplitudes are seldom larger than twice the conductor diameter.

The characteristics of the flow pattern are described by means of the dimensionless Reynolds number, which is the ratio of inertial to viscous forces. It is given by:

$$Re = \frac{\rho \cdot u \cdot d}{\mu} \tag{2.21}$$

where ρ is the density of the fluid, u is the flow velocity, d the characteristic length of the flow geometry and μ is the dynamic viscosity. Another important quantity to describe flow characteristics is the vortex shedding frequency:

$$f = \frac{St \cdot u}{d} \tag{2.22}$$

where St is the Strouhal number. In the sub critical range of the Reynolds number of a flow around a cylinder, the Strouhal number is approximately 0.2. It ranges over all flow conditions commonly of interest in the scope of conductor oscillation since the stranded surface of conductors causes only minor deviations from a smooth cylinder behaviour [154]. Observations show that conductor oscillations not only occur at wind velocities associated with resonance of vortex shedding and natural conductor frequency, but in a range of 85 to 115 % of the wind speed associated with the given Strouhal number. This is due to the line motion, it correlates with the vortex separation along the line and the movement controls the shedding frequency [19]. The vibrations arising from vortex shedding are multiple sinusoidal waves along the transmission line. In practice, the frequency range of conductors varies from 3 to 150 Hz and the maximum amplitude can reach the conductor diameter [154]. It depends on the wind speed or rather on the balance of excitation force due to vortex shedding and damping of the conductor and applied dampers. The amplitude tends to decrease with increasing frequency, since the internal damping increases with the frequency. A snow covered environment might

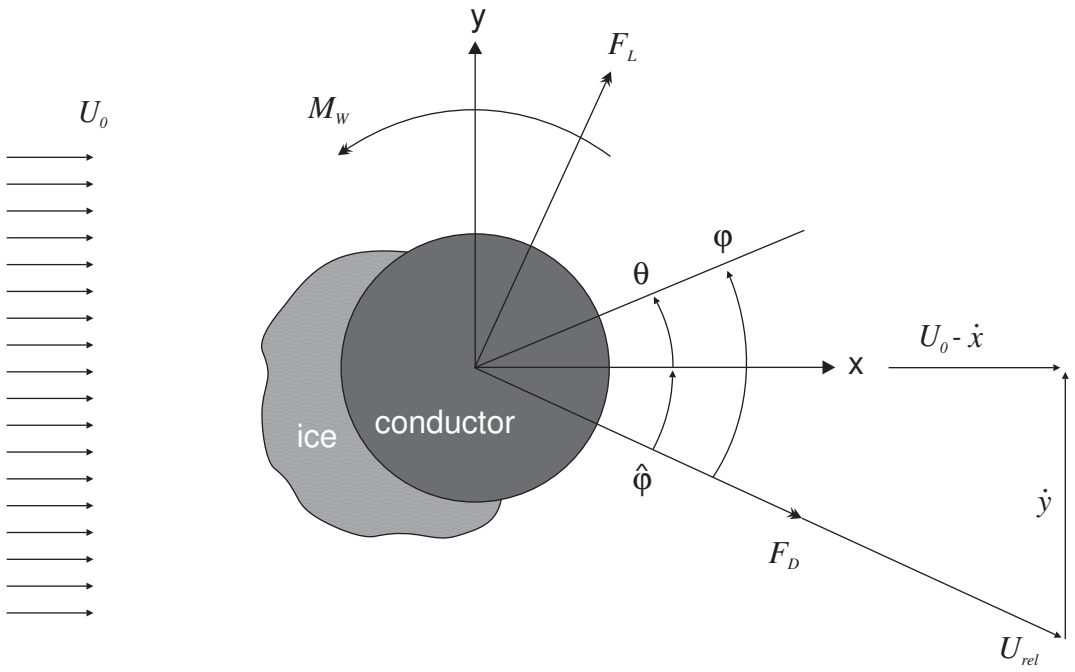

Figure 2.14: A conductor with ice deposit is exposed to a steady wind velocity U_0. Aerodynamic drag force F_D, lift force F_L, and aerodynamic moment M_W, are caused by the relative wind velocity U_{rel}, which results of the steady wind velocity and the velocity of the conductor $\dot{x}$ and $\dot{y}$. The angel of attack φ, the conductor rotation due to ice accretion and other torsion forces θ and the fraction of the angle of attack due to vertical movement $\hat{\varphi}$, are orientated counter-clockwise.

affect the wind velocity fluctuation, since it smoothes the terrain [154]. A less turbulent wind field supports the initiation of vortex induced oscillations. In any case, direct consequences of ice accretion are more significant. The internal damping of the conductor depends significantly on the resulting tension. Additional ice and snow loads increase the tension in the conductor and thus decrease the internal damping. Furthermore, ice may bond conductor strands together and thereby decrease internal damping as well. Also the vortex shedding frequency changes due to ice and snow deposits. For conductors with low torsional stiffness the deposit forms sleeves around the conductor. The cylindrical cross-section remains, but the diameter increases, which leads to a lower shedding frequency. On conductors with higher torsional stiffness the deposit occurs on the windward side and the geometry is no longer cylindrical, which affects the shedding frequency via a changing Strouhal number. Both alter the oscillation frequency when it comes to galloping. Therefore it might be out of the feasible range of applied dampers or the dampers could lose their efficiency being iced themselves.

2.5.2 Galloping of Conductors

Galloping is an aeroelastic instability of bluff bodies in a streaming fluid. In contrast to vortex induced vibrations, galloping can be considered as a negative aerodynamic damping because it works along with the motion velocity of the conductor. The classical conductor galloping was described by Den Hartog [22]. It is a one degree of freedom oscillation, considering only vertical displacements. Observations showed that iced conductors can also experience oscillations with torsional and horizontal components. These instabilities with two or three degrees of freedom are termed as flutter or flutter galloping. Commonly, all conductor oscillations with large amplitude and low frequency are called galloping. The amplitudes may reach up to 150 times the conductor diameter, which means a maximum displacement of several meters. The aeroelastic instability originating from lateral movement that causes an additional aerodynamic force in the same direction. This can be explained using the quasi-steady hypothesis. This approach uses the relative wind velocity calculated from a constant wind velocity and the moving velocity of the conductor. The motion changes the angle of attack and the relative velocity, which leads to pressure variations on the surface resulting in aerodynamic forces amplifying the conductor motion. These aerodynamic lift and drag forces act in the aerodynamic centre, whereas its position is not known a priori. Therefore, the centre of the conductor is commonly chosen as reference point for the forces and an aerodynamic pitching moment is introduced to account for the location of the aerodynamic centre.

In order to model galloping of an iced conductor lift, drag and aerodynamic moment coefficients are determined by wind tunnel experiments [17, 105]. The aerodynamic coefficients are measurements on fixed, rigid cylinders with an attached ice profile. The cylinders are examined along their rotation axis.

Semi-empirical models are commonly used to describe conductor galloping with a quasi-steady approach. It implies a steady wind velocity relative to the conductor. The flow velocity acting on the conductor results from the steady wind velocity and the conductor motion. Semi-empirical means in this sense that the equation of conductor motion includes aerodynamic coefficients derived from wind tunnel experiments. Figure 2.14 shows such a semi-empirical model. The cross-section of an iced conductor is exposed to a steady wind. Aerodynamic drag force, lift force and aerodynamic moment originating from the relative flow velocity:

$$U_{rel} = \sqrt{(U_0 - \dot{x})^2 + \dot{y}^2} \tag{2.23}$$

where U_0 is the steady wind velocity, $\dot{x}$ and $\dot{y}$ are the velocity components of the conductor. The angel of attack describes the angle between the relative flow velocity and the reference line of the initial orientation. It leads to the following expression for the Aerodynamic force

and the aerodynamic moment:

$$\begin{aligned} F_D(\varphi) &= \frac{1}{2} \cdot \rho_f \cdot C_D(\varphi) \cdot d \cdot U_{rel}^2 \\ F_L(\varphi) &= \frac{1}{2} \cdot \rho_f \cdot C_L(\varphi) \cdot d \cdot U_{rel}^2 \\ M_W(\varphi) &= \frac{1}{2} \cdot \rho_f \cdot C_M(\varphi) \cdot d^2 \cdot U_{rel}^2 \end{aligned} \tag{2.24}$$

where ρ_f is the air density, C_D, C_L and C_M are the aerodynamic coefficients. To define the coefficients as dimensionless quantities the characteristic length d is required. At first, for simplicity reasons the galloping mechanism is explained considering only vertical displacements, then later also torsional displacements. Field observation revealed that also inclined, elliptical oscillation trajectories of conductors occur, showing the presence of a horizontal component. This horizontal displacement may originate from increasing wind velocities over the height, increasing the drag force with altitude. Or the drag force changes with the angle of attack during an oscillation cycle. Thus, the horizontal movement would correspond either to the vertical or torsional displacement [154]. To consider only vertical displacements assumes that the conductor is infinite rigid and no torsion can occur. It leads to $\widehat{\varphi} = \varphi$ and consequently the vertical force acting on the conductor is defined by:

$$F_y(\varphi) = F_D(\varphi) \cdot \sin(\varphi) + F_L(\varphi) \cdot \cos(\varphi) \tag{2.25}$$

For small perturbation of an angle $\Delta\varphi$ the trigonometric expressions can be simplified to:

$$\cos(\Delta\varphi) \approx 1 \qquad \textit{and} \qquad \sin(\Delta\varphi) \approx \Delta\varphi \tag{2.26}$$

Expanding the aerodynamic coefficients in a Taylor series and using only the first two terms leads to:

$$C_{L,D}(\bar{\varphi} + \Delta\varphi) = C_{L,D}(\bar{\varphi}) + \frac{\Delta\varphi}{1!} \cdot \frac{dC_{L,D}(\bar{\varphi})}{d\varphi} + \frac{\Delta\varphi^2}{2!} \cdot \frac{d^2C_{L,D}(\bar{\varphi})}{d\varphi^2} + \ldots \tag{2.27}$$

A new expression for the vertical force accounting for small vertical displacements is then:

$$F_y(\bar{\varphi} + \Delta\varphi) = \frac{1}{2}\rho_f \cdot \left(C_L(\bar{\varphi}) + \Delta\varphi \cdot \frac{dC_L(\bar{\varphi})}{d\varphi} + \Delta\varphi \cdot C_D(\bar{\varphi}) + \Delta\varphi^2 \cdot \frac{dC_D(\bar{\varphi})}{d\varphi} \right) \cdot d \cdot U_{rel}^2 \tag{2.28}$$

One can see that for small displacements the term $\Delta\varphi^2$ is negligible and the expressions with $\Delta\varphi$ account for force variations. For the following equation small vertical displacements leading to small changes in the angle of attack cause an additional force in the same direction.

$$\frac{dC_L(\bar{\varphi})}{d\varphi} + C_D(\bar{\varphi}) < 0 \tag{2.29}$$

If this amplifying effect is larger than the damping, conductor and wind velocity add their effect to one another and galloping oscillations build up.

As mentioned before transmission lines do not experience only vertical oscillations. And obviously a conductor of several hundred metres with a diameter of a few centimetres is not rigid in torsion. Significant effort was spend to investigate this aspect for both single conductors and conductor bundles [42, 102, 105, 108, 109, 132, 134, 155, 163, 164, 165, 175]. The torsional stiffness depends not only on the line diameter and material but also on the tension. In conductor bundles the tension in every subconductor is different. Number, spacing and distance between spacers have an additional influence on the torsional behaviour. Therefore, torsional stiffness of bundles is generally two orders of magnitude higher than of single conductors, which may have stiffnesses in a range of 10 to $1000\,\mathrm{Nm}^2/\mathrm{rad}$. Moreover, conductor bundles can show resonance between the vertical and the torsional modes unlike single conductors where the frequency of the torsion model is about 3 to 10 times larger than of the vertical mode. However, torsion occurs in both single and bundle conductors. When considering vertical displacements together with torsion the instability criterion is not as easy to establish. Several cases are possible: First, rotation can be in phase with vertical displacement, which requires a significant distance between vertical and torsional oscillation frequency as it is true for single conductors with only a thin ice deposit [96], for example. The torsional movement has no inertia effect on the vertical oscillation. Consequently, the galloping criterion is still valid, just the calculation of the angles is a bit more complex. Second, when it comes to phase shifts of vertical and torsional oscillation, flutter galloping can occur. In such a case, torsional damping and resonance of vertical and torsional modes are important, which makes the investigation of flutter galloping more complex. Details on theoretical and practical aspects of flutter instabilities are discussed in a report by Kirch and Peil [57]. Flutter galloping is commonly expected for bundles or single conductors with large ice deposits, whereas severe flutter galloping is mainly associated with conductor bundles. Severe galloping oscillation of single conductors are in contrast to that usually caused by vertical galloping [154]. Not yet mentioned is the influence of tension in individual conductors on the stiffness and thus on the oscillation behaviour. A Finite Element (FE) model by Wang and Lilien illustrates this aspect of dynamic behaviour of conductor bundles nicely [163, 164]. A similar model by Zhang et al. also considers ice accretion on the transmission line [175]. The ice deposits are assumed to have identical shape on all subconductors. We will see in section 4.6 that this is not necessarily the case.

Calculating the aerodynamic forces based on the quasi-steady approach is for many applications feasible [139]. Recently attempts have been made to include the interference effect of cylinders in a tandem arrangement in a quasi-steady model [169]. None the less all these models based on the quasi-steady approach are limited in the analysis of iced conductor bundle oscillation, since the wake is not considered so far and the wake induced oscillations are not yet modelled (cf. section 2.5.3).

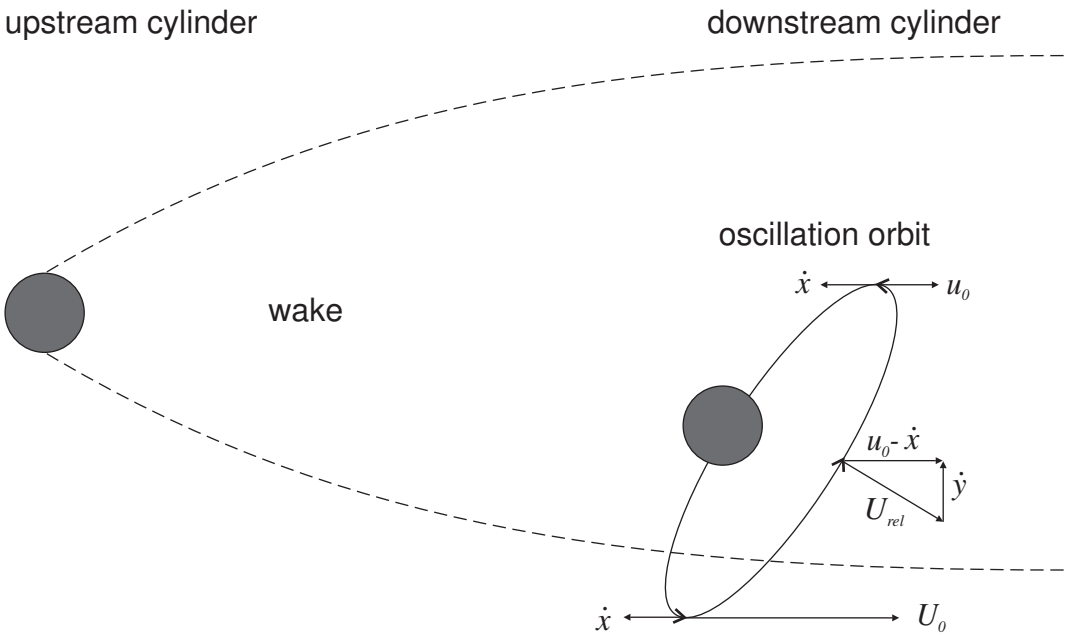

Figure 2.15: Wake induced oscillation orbit of a cylinder, at a freestream wind velocity U_0 and a velocity in the wake $u_0 < U_0$. The velocity components of the oscillating conductor are $\dot{x}$ and $\dot{y}$ leading to a relative flow velocity U_{rel}.

Already in the 1940s flutter of air foils was examined with an unsteady approach [63]. It considers not only relative flow velocity and angle of attack, but also velocity of the structure. Due to the collapse of the Tancoma-Narrows Bridge, this approach is also applied in designs for slender long span bridges [135]. Recent investigations on iced conductor bundles by Waris et al. compared galloping predictions of unsteady versus quasi-steady theory for transmission lines [165]. It showed that the unsteady approach achieved better results, when the mode frequencies are not coupled. When the frequencies are coupled the results are similar. However, the unsteady approach seems more robust than the quasi-steady approach in predicting galloping. Another recent study compared field measurements with a model using an unsteady approach for various types of conductor bundles without ice deposit [124]. The comparison showed also that the approach is adequate for engineering purposes.

2.5.3 Wake Induced Oscillation Mechanisms of Bundle Conductors

Wake induced vibrations are less frequent than galloping or vortex induced vibrations. They only have a significant effect on subspans of conductor bundles, where two or more cables are arranged in line of the wind direction. Single conductors are too far apart for wake induced oscillations to occur. In case of bundle rolling, twisting or full span galloping the wake of upstream cables has no influence behaviour of the whole bundle.

But the wake behind an upstream conductor may excite a downstream conductor to vibrate. When a critical wind velocity is reached a downstream cable drifts downstream with the strong flow external of the wake and upstream against the weaker flow in the wake. Leading to a characteristic elliptical orbit of the downstream cylinder is shown in figure 2.15. In practice the oscillation frequency of the subspan lies within a range of 1 to 5 Hz [154]. The parameters influencing the wake induced vibrations are the ration of conductor spacing and conductor diameter, angle of attack, distribution pattern of spacers along the span and length of a subspan, which is the distance between spacers. The first two are affected by ice accretion. The ratio of spacing to diameter is usually above 10 for bare conductors and therefore only small excitation forces are expected on the downstream conductor. But when the wind velocity is high enough the leeward conductor can experience oscillations large enough to cause even conductor clashing. Furthermore, due to the spacers the conductors are mechanically coupled. A sufficient amount of spacers along the span can prevent this problem. However, with ice or snow deposits the spacing to diameter ratio, is reduced and thus the excitation forces increase significantly. Assuming a conductor diameter of 35 mm together with a spacing of 400 mm, the ratio is about 11.4. A snow event might lead to snow accumulation around the conductor. A deposit depth of 20 mm is already possible under moderate snow intensity. The diameter enlarges to 75 mm and the ratio drops to 5.3. Thus the excitation forces increase significantly and severe subspan oscillations may occur. Another parameter influenced by ice or snow accretion is the angle of attack. Torsional displacement occurs on bare conductor bundles, but even more on bundles with unevenly iced conductors. The tilt changes the angle of attack and exposes the downstream conductor to the flow outside the wake, which drives the oscillation. Especially, if the tilt is negative and the leeward cable is below the windward one. Then the external flow catches the conductor at an optimal position on its oscillation orbit. Quad bundles, four conductors arranged in a square with 400 mm spacing, with a negative tilt of approximately 10 degree can suffer under severe subspan oscillations [42], for example. Subspan oscillations of iced quad bundles have been observed to last for several hours causing extreme stresses on spacers and connections [56].

2.5.4 Effects of Galloping on Transmission Lines

Clashing of conductors and flashovers are the most frequent problems of galloping transmission lines. Flashovers cause circuit breakers to open. Such repeating power interruption obviously reduces the service quality and can damage the circuit breakers seriously. And also the conductors can be damaged due to the clashing and flashovers. Transmission line galloping causes dynamic loads in conductors and support structures. Field measurements have shown that vertical loads on insulators and towers increases up to 2.0 times the static loads of the iced conductors [154]. Horizontal loads due to tension in the cables rises up to 2.8 times on anchorage structures [154]. Additional loads due to galloping are commonly assumed to be covered by designing the structures for extreme wind or ice loads. But dynamic loads can cause

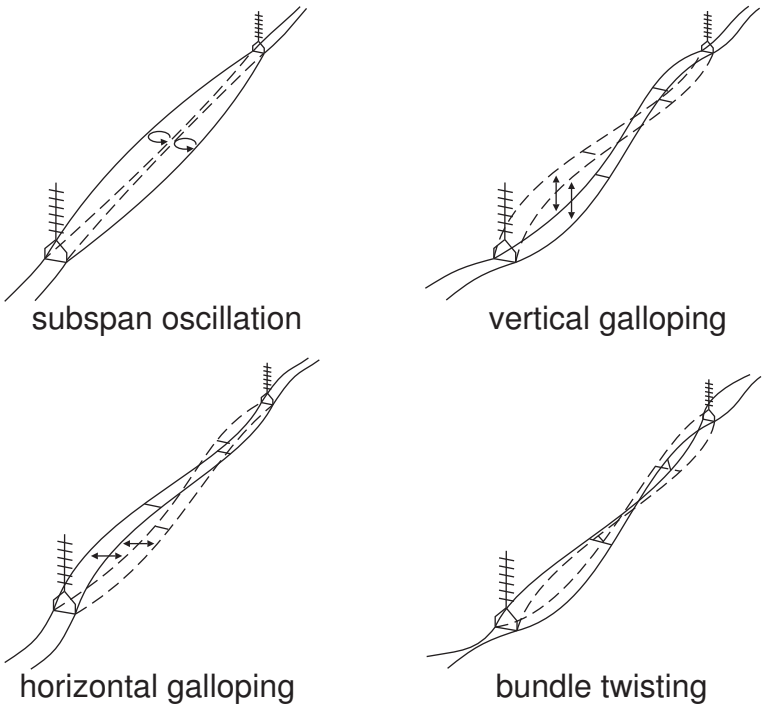

Figure 2.16: Oscillation modes of conductor bundles (following [123] from [42]).

fatigue damages. Most commonly they occur in bracing members and connections, rarely in main members of the towers. In general towers fail due to fatigue next to insulators. They suffer from damages due to bending moments during the galloping and clashing against tower arms. Cables of conductor bundles can clash and destroy the glass or porcelain insulators. Dampers are also occasionally damaged due to steep travelling waves and low frequency galloping with large displacements. This can occur, when the oscillation frequency and displacement exceed the design criteria of the damper. Fatigue damages on the conductor are seldom a problem, whereas it is a problem for the connection devices.

2.5.5 Mitigation of Galloping on Transmission Lines

No mitigation strategy for galloping oscillations or damages due to galloping is able to prevent it under all conditions. To prevent galloping they need to act either on the oscillation behaviour of the conductor or the aerodynamic instability. The first would mean to apply dampers or de-tuning pendulums to mitigate oscillations. Dampers dissipate oscillation energy. Detuning pendulums on the other hand shift the natural frequency of the line to avoid resonance. Field observations have shown that detuning pendulums alone could reduce the maximum galloping amplitudes for single and bundle conductors of two and four cables by roughly one third [154]. A very efficient anti-galloping strategy is a combination of detuning the vertical degree of freedom (DOF) and using a damper for the torsion DOF [163]. Regardless of the type of

damping under ice accretion it may lose its efficiency. The oscillation frequency may leave the design range or the mode changes due to ice accretion or the damper is iced and not working as intended. In order to avoid the formation of aerodynamically instable cross-sections anti- or de-icing methods can be used. However, they are not as wildly used as dampers. An overview of anti- and de-icing strategies is given in section 2.6. Interphase spacers are used to keep clearance between oscillating conductors of different phases. They prevent flashovers and damages due to clashing of conductors, but they do not mitigate galloping. Also larger clearances between conductors and between conductors and ground wire are used to avoid flashovers of oscillating cables. Dynamic loads arising from galloping are still present though and fatigue damages remain problematic.

2.5.6 Rolling of Conductor Bundles

Massive, eccentric ice and snow loads alone or in combination with wind loads can lead to rolling of conductor bundles. This damages spacers and conductors and can lead to service interruption. But this damage mechanism is barely investigated. So far a simplified model based on experimental tests is used to describe and predict bundle rolling [108]. As expected longer spans have lower torsional resistance and are more vulnerable than shorter spans. The application of spacers can increase the torsional resistance of the bundle, so that the bundle returns to its original position once the ice is melted. But when spacers slip on the conductors the restoration is a costly procedure. However, icing process and behaviour of iced conductor bundles still show a need for investigation. A cause of bundle rolling, the ice accretion, is investigated by the here presented model.

2.5.7 Ice Shedding as Dynamic Load

Sudden ice shedding generates high dynamic loads, which can cause severe damages on the transmission lines such as tower arm failure or even cascading failures of several towers[154]. Due to the recoil the conductor can hit another conductor, parts of the tower or the ground wire causing a flashover. The shedding ice may also threaten humans and passing vehicles or buildings in the area. Ice shedding is difficult to observe. It happens suddenly and with low damping the oscillation can last for several cycles with slowly descending amplitudes, but there is no continuous excitation like it is in case of galloping. Numerical investigations of the loads arising from ice shedding assumed a complete shedding of the whole span. That made also structural damages appear possible [30]. But observations revealed that the ice is unzipped rather than falling off in one piece. Parameter studies of iced guyed masts considered partial and full span ice shedding. They revealed that ice shedding is a minor problem for structural reliability for guyed masts [111, 112]. The actual unzipping of ice along a span was investigated on a test line and later in numerical models [126]. It showed that also for transmission lines

damages due to ice shedding are not grievous. Designing vulnerable transmission lines with enough clearance and interphase spacers in the middle span can overcome problems due to ice shedding [154]. However, so far ice shedding is not considered as a significant threat to the structural reliability of transmission lines. Further monitoring of such events would not only be interesting but also help to distinguish their damaging potential from those of galloping effects.

2.6 Mitigation of Ice Accretion

The first and fairly simple way to mitigate damages due to ice accretion on transmission lines is to avoid areas of high icing intensity, to design structures so that they cope with atmospheric icing or to use underground cables. Unfortunately the first two are not always possible and the latter is just too expensive. Therefore, considerable effort has been spent to develop strategies for mitigating the risk of atmospheric icing on electrical power networks. Different classes of mitigation strategies are possible. The two basic concepts are either to prevent ice accretion in advance or to remove ice deposits from the cables at an early stage. The first strategy is called anti-icing and the second de-icing. Each of the two include different methods, which are classified as thermal, mechanical, passive and miscellaneous [43].

Anti-icing includes all methods aiming to prevent or reduce the adhesion strength between ice and conductor surface. It can reduce the expected design loads and hence make the construction of new lines more economical. On existing lines anti-icing can increase reliability in extreme icing events, when it was not considered in advance. The methods applied for anti-icing are passive, thermal and miscellaneous.

As the name indicates, all de-icing methods begin to remove ice deposits once a certain amount of ice has accreted. Therefore they all need some kind of ice sensor to guarantee suitable operation. De-icing methods are either thermal or mechanical, whereas thermal methods need more energy, but less manpower in comparison to mechanical methods. The first is mainly applied on the conductors, but not to ground wires. In contrast to conductors the ground wires are not part of the electric circuit. They are positioned above the conductors to protect them from lightning impacts. On ground wires and in cases of urgent local de-icing, mechanical methods are usually preferred. The following sections give a brief overview of both strategies and concepts of the major methods. For more details, an overview given by Farzaneh and colleagues is recommended [29].

2.6.1 Passive Anti-Icing

Passive anti-icing methods either act on the adhesion strength between ice and conductor or prevent freezing of super-coold droplets on the surface. Icephobic and hydrophobic behaviour

Figure 2.17: Conductors sagging under heavy snow and ice load and touching the ground. (with permission of Thierauf, photo: Moog, 2005)

is closely linked. Icephobic coatings affect the adhesion strength by acting on the physical-chemical and mechanical behaviour at the interface. These coatings are made of materials with a low surface energy, such as polymers. But also new material like self-assembled monolayer or diamond-like carbon materials are examined for their hydrophobic and icephobic behaviour [29]. Roughly speaking, surface energy is the energy necessary to break the chemical bounding at the surface. In case of liquids it resembles the surface tension. It tends always to its minimum. Therefore, a solid body with a high surface energy is easily wetted by a liquid, because it tries to achieve minimum energy difference at the interface. The same liquid wets a body with low surface energy less, since the energy level differs less. The hydrophobic effect is increased if the surface of a hydrophobic material is roughened or material of low surface energy covers a rough surface [29].

Hydrophobic behaviour can be measured by two parameters: the contact angle and the sliding angle. The first is adequate to judge the hydrophobic behaviour of solid surfaces. It is measured as illustrated in figure 2.18. A contact angle of more than 90 degree characterises hydrophobic materials and an angle over 150 degree a super hydrophobic material. The rough surface is beneficial for the hydrophobic effect, since air is trapped in small gaps in the surface texture when a droplet touches the surface. Hence, the droplet rests partially on air and the total adhesion strength of the water on the solid interface is reduced.

A sliding angle, the second parameter, describes the sliding property of droplets. In the scope

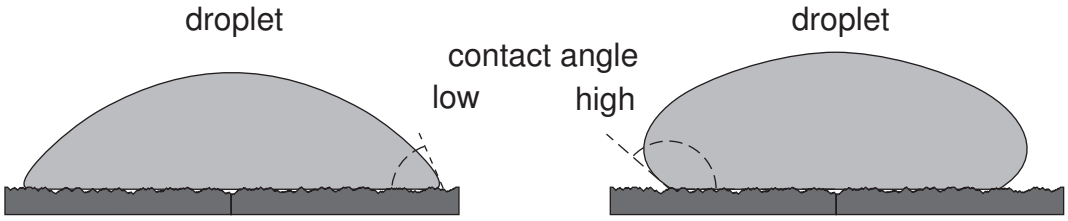

Figure 2.18: Droplet with low (left) and high (right) contact angle.

of icephobic behaviour a rough surface can also have an adverse effect. When the droplets hit the rough surface with high velocity or if the water film is deep enough to press the droplet into the small gaps while they freeze, the icing has additional anchorage which eventually leads to increased icing. Therefore sliding of droplets is also taken into account to measure icephobic properties. The sliding angel defines the inclination of a plane leading to sliding of a droplet on this formally horizontal plane (cf. figure 2.19). A low sliding angle indicates a high sliding or rolling ability of a droplet. Icephobic and hydrophobic are linked since unfrozen supercooled water droplets are a source of ice accretion. A hydrophobic surface leads to a small contact interface of the freezing droplets, which lessens the ice adhesion strength. Furthermore, hydrogen bonding seems to have an impact on the ice adhesion strength [113, 140]. Generally speaking, icephobic surfaces reduce the adhesion strength of ice. Perfect icephobic properties would reduce adhesion to such an extent that the ice sheds from its own weight or from wind action, but so far no material can achieve this. Another way to weaken the adhesion strength of ice is a temporary coating of so-called viscous icephobic materials. Industrial oils and greases can be used to decrease the adhesion strength of the ice, when they cover a surface as a thin layer. Experiments show that lithium grease and industrial lubricants can reduce the adhesion strength significantly [65]. But in the scope of electrical power networks they are not applicable, since they require continuous reapplication leading to huge maintenance costs. Beside that they are not biodegradable and therefore a threat for the environment. Another type of anti-icing methods is aimed at preventing freezing of supercooled droplets or at least keeping a thin water film at the ice-conductor interface to achieve natural ice shedding due to own weight or wind. One way is to use freezing point decreasing liquids, which are commonly used to protect aircrafts from icing. However, like the above mentioned viscous icephobic materials, they require continuous reapplication and therefore are not suitable for electrical power networks.

2.6.2 Thermal Anti-Icing

Obviously, it is also possible to prevent freezing by keeping the temperature of the conductor surface above zero. All methods for heating the conductor surface can be used for anti- as well as for de-icing. In general, de-icing requires more energy than anti-icing techniques. The thermal methods are described in more details in section 2.6.4.

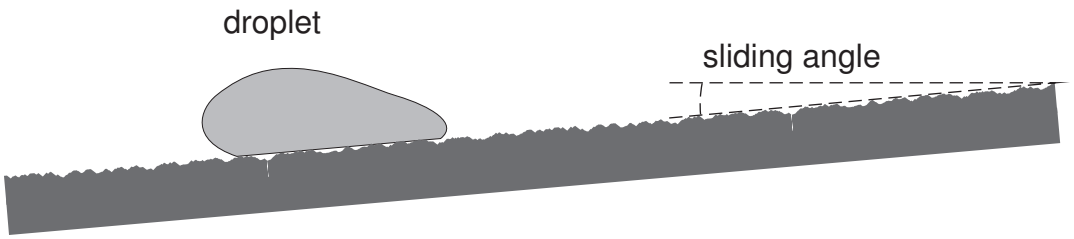

Figure 2.19: Droplet sliding on an inclined plane to measure the sliding angle.

2.6.3 Anti-Torsion Anti-icing

Anti-torsion devices like counterweights or spacers can reduce the amount of snow deposit and even accelerate the snow shedding. Due to the restrained torsion the snow accumulates on the windward side and the formation of cylindrical snow sleeves is limited. The eccentric snow load sheds easier due to wind and own weight. The same holds true for ice accretion, where the effect is smaller for glaze and for rime ice. Here anti-torsion is considered as an anti-icing strategy, since it hampers the accretion process from the beginning [117].

2.6.4 Thermal De-Icing Methods

The most efficient way of thermal de-icing is the so-called Joule heating. Joule heating is generated by the electrical current and the electrical resistance of the conductor. Alternating current (AC) as well as direct current (DC) are used to melt ice on transmission lines.

For historical reasons, high voltage power networks generally transmit in AC. In earlier days it was only possible to transform AC to higher voltages, which is necessary for an efficient transmission over distances. The phase shift of current and voltage occurring in AC circuits leads to so-called reactive losses. Due to the phase shift, current and voltage have periodically opposing signs and thereby power is induced from the customer back into the network. This reactive loss oscillates between producer and consumer. It is not usable for the customer, but it creates additional load on the network. Therefore, the required current for melting is very high for long transmission lines. Consequently, AC is efficient for de-icing when the lines are not too long, because the required melting current is not too high. Since it is possible to transform DC to higher voltages, reactive losses are avoidable. On the other hand the transformation to higher voltages also involves losses, making power transmission with DC more efficient only for long transmission lines. Thus, DC is used for de-icing only for long transmission lines. A drawback of using DC only because of de-icing is the expensive additional DC converter, when the line is supposed to transmit AC.

One approach is to shift more current load on a certain conductor to increase its temperature. But the available power load depends on the customer's demand. A minimum amount is needed to produce enough heat, whereas too much energy leads to overheating of the conductors and

eventually to failures. Furthermore, the load shifting method needs to be continuously adapted for the actual weather conditions [29].

Another method is to create a short-circuit on a section of the transmission line with a three-phase voltage source. In contrast to the load shifting method some additional equipment is needed here [29]. The method can also be applied on ground wires, but it requires a current source and the insulation of the ground wire. To avoid this effort ground wires are often designed for higher ice loads or simply replaced when they are damaged.

Special conductive coatings that are insulated from the conductor for being heated by an electric impulse to melt ice deposits. An alternative are electrode grids covering the conductor, but being insulated from it. Once ice accretes the circuit between grid and conductor is closed and the electrolysis starts. It weakens the ice adhesion strength, the produced gas acts as entrapped air in a textured surface and contributes to interfacial cracking [29].

Other thermal methods developed for de-icing of railways for example, do not use the heat generated by the conductor itself, but rely on radio-waves or steam. However they seem to be less useful for transmission line de-icing and only suitable for local interventions at accessible systems [29].

2.6.5 Mechanical De-Icing

In general mechanical de-icing is done by shattering the ice directly from the line or using shock waves or vibrations. If the lines are accessible, the ice can be shattered manually with scrapers and rollers. Due to this restriction also automatic de-icing robots are being developed. Mounted on the lines, they are supposed to run along the conductors and ground wire to remove the ice. Ice is a very brittle material at strain rates over $10^{-3}\ s^{-1}$for tensile or compression forces [114]. Mechanical energy is not dissipated in plastic deformation and therefore shock waves causing high strain rates need less mechanical energy to cause ice shedding. The mechanically induced shock waves are created manually on accessible lines using piston devices or ropes with hook heads to create the shock wave. In mountain areas also helicopters with weights attached along a rope are used to excite the conductor. Lifting and dropping the rope causes an impulse every time a weight hits the conductor. Care must be taken to avoid the rope hitting the ground and causing an outage of the line. It is also possible to create shock waves via electro-impulse. There, an electric coil is used to produce a strong magnetic field for a few milliseconds. This induces a shock wave on a conductive target attached to the line. Another way is to de-ice the lines to create forced vibrations in longitudinal or torsional direction until the ice is shed. For longitudinal vibrations the cables are excited in their natural frequency by motors with unbalanced weight, which are easily installed. Problems may arise through high amplitudes and fatigue damages. The method using torsional vibrations is safer in this sense, since the deformation is below the shear limits of the lines. The mechanism is less robust and not easy to install on the transmission lines, but it works well for all types of ice and snow accretion.

2.6.6 Applicability and Constrains to Anit- and De-Icing

All aforementioned methods have some electrical, mechanical, thermal or environmental restrictions limiting their practical application. For example, if the methods involve high frequency electric fields, electromagnetic disturbances can affect public, private and commercial infrastructure. Also flashover, lightnings and the risk of outages should be considered. Coatings need to resist the same mechanical stresses as the conductor or the ground wire, whether the stresses is coming from wind induced vibrations, shock waves due to high-current pulses caused by short-circuits or the anti/de-icing itself. The same holds true for anti- or de-icing devices attached to the transmission line. Lightning impact and service temperature of energised conductors present thermal constraints on transmission lines. Lightning causes locally high temperatures on the surface, which can even melt aluminium fibres [29]. Thus any coating or de-icing device attached to the line could be damaged by such temperatures. Service temperature depends on ambient temperature, wind velocity, electrical current and conductor design. During the winter period this is not critical, since the low ambient temperature ensures low conductor temperature. But in summer with high ambient temperature, sun radiation and no wind the conductor temperature is only limited by the current intensity. Above a certain temperature of the conductor line failures can occur due to sagging or line loss. Also U.V. radiation needs to be taken into account, since it can shorten the life time of coatings.

3 Ice Accretion Model

3.1 Model Structure

3.1.1 An Overview of the Ice Accretion Model

This section proviedes an overview of the ice accretion model. Modelling atmospheric icing includes a computation of the mass flux of icing particles as well as a determination of the icing conditions. The mass flux computation requires modelling a mixed stream of air and precipitation particles, which influence shape and to a smaller extent also density of ice deposits. Icing conditions are defined by the heat balance on the ice surface. Messinger proposed a basic scheme to investigate heat balances on ice surfaces [98]. The icing condition influences the accretion mass and furthermore the evolving ice density. Three major types of deposit, namely rime, glaze and wet snow lead to significant loads on structures. The heat balance is very sensitive in case of glaze ice and wet snow formation, because it occurs at the transition of freezing and melting and is therefore considered as wet ice growth. In contrast to that, rime ice develops in dry growing conditions. The heat transfer within the system can be neglected, because the latent heat of the droplets released during freezing is dissipated without changing the state of the ice and the surface conditions. Hence, no liquid layer arises.

Figure 3.1 shows the flow diagram of the ice accretion model described in this chapter. It displays all elements of a single simulation step. Each step assumes steady conditions over a time interval of $20 - 180$ seconds. The size of the time steps depends on the accumulated mass on the conductor. A large flux of icing particles requires smaller time steps than a low flux to adequately describe the ice growth. As consequence of assuming steady conditions during each calculation, the model can not account for transient particle flux. This flux may cause ice accretion that vanishes due to time-averaging.

The definition of simulation parameters follows a stationary computation of the air flow around the conductor bundle with a finite element (FE) model. The fluid dynamic model described in section 3.2 uses Reynolds Average Navier-Stokes (RANS) equations to calculate the two-dimensional flow. Mass flux of icing particles as well as heat balance in conductor and ice deposit are determined based on a previously determined flow field. Particle trajectories and flow field are considered as one-way coupled, which is explained in section 3.3. The heat balance is solved on the same FE mesh as already used for the flow calculation. The heat transfer model presented in section 3.4 defines the ice growing conditions, which are either dry

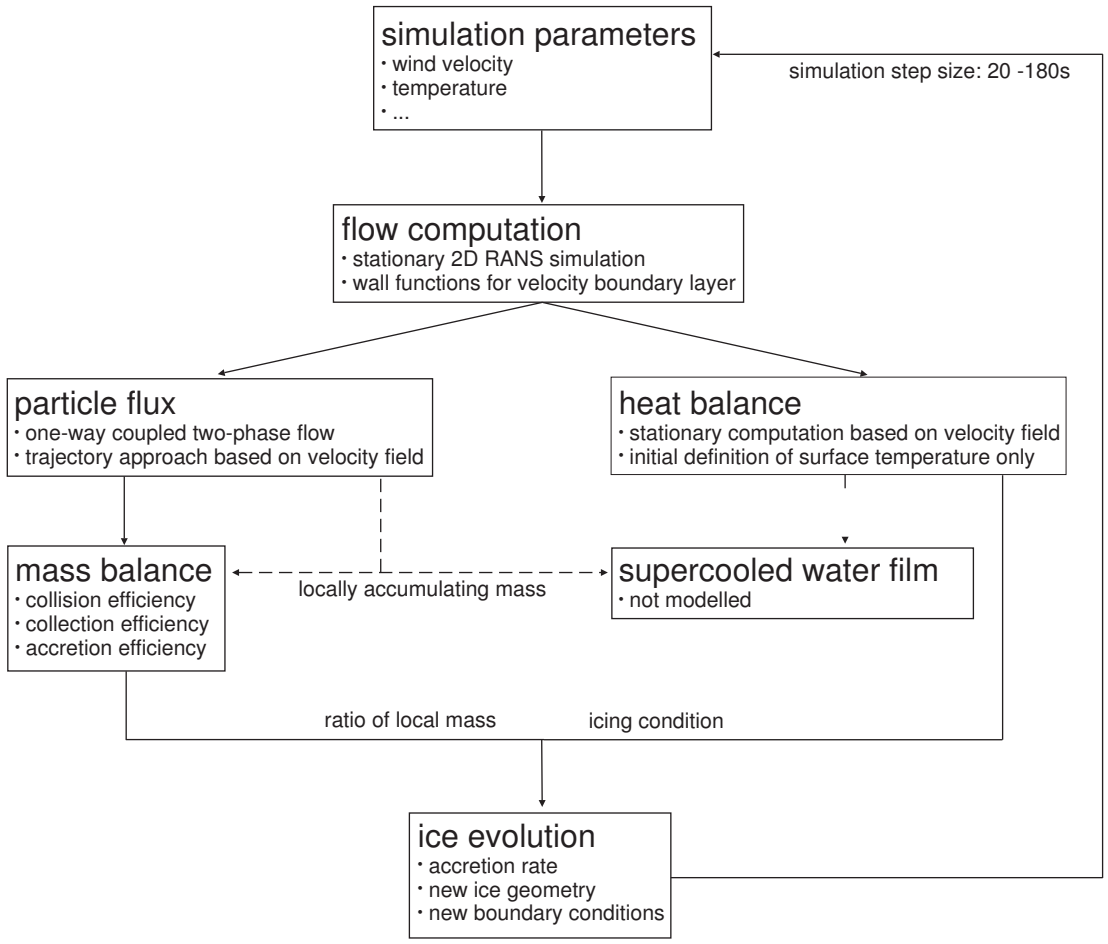

Figure 3.1: Simulation flow diagram.

or wet. In the latter case a supercooled water film arises on the ice surface, which influences ice shape and density. However, a simulation of the supercooled water film is not included in the model for reasons described in section 3.4.2. Subsequently, the ice growth model described in section 3.5 determines the mass balance on the surface, based on the mass flux of icing particles as well as on the growing condition. Each simulation step concludes with defining the new geometry of the ice body, providing the basis for the next run. The ice growth is determined by a finite difference (FD) model.

The structure of chapter 3 follows the simulation flow diagram. Hence, section 3.2 deals with the flow calculation and the mass flux of icing particles is discussed in section 3.3. The heat balance as well as the treatment of the supercooled water film is explained in section 3.4. Subsequently, the computation of the mass balance at the accretion surface and the ice growth model are described in section 3.5. One might argue that splitting the simulation into a number of models and explaining them separately is not beneficial, since the physical processes of fluid flow and heat transfer are closely linked. However, subdividing the simulation step into several elements eases the understanding of the ice accretion model. The modelling approach

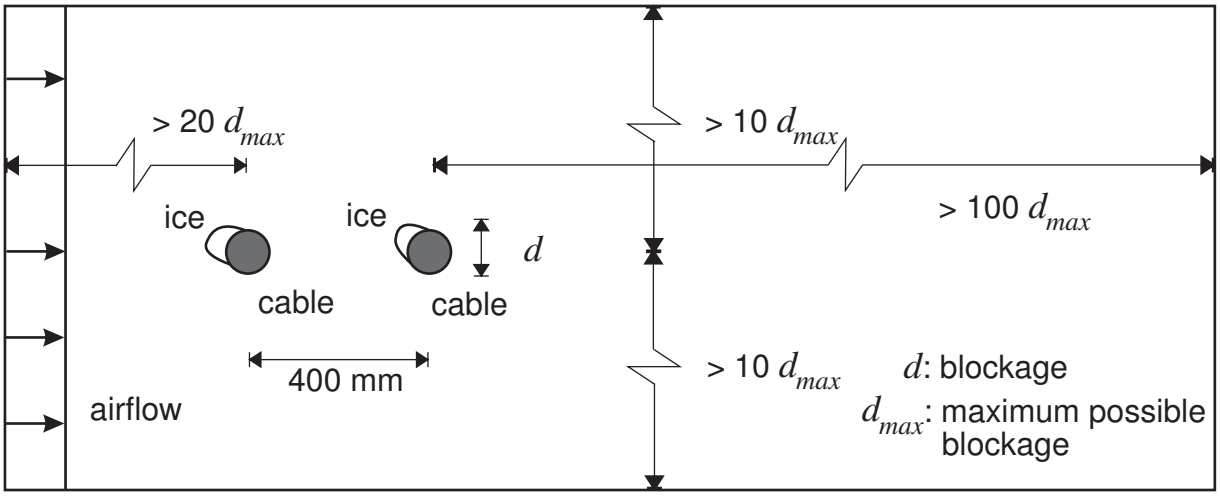

Figure 3.2: Model geometry.

and decoupling of individual computations is justified and explained in detail in each section. Furthermore, each section concludes with a discussion of the model in order to justify the decisions made during the model development.

The implementation of the ice accretion model is based on the numerical software package MATLAB R2009a. The model structure, the mass balance at the accretion surface and the ice growth model are developed using MATLAB R2009a. Flow and particle trajectory calculation as well as heat transfer computation use algorithms of the finite element software COMSOL 3.5a. The software packages are coupled, which allows using individual algorithms of both packages in one program. However, the automatic transfer of boundary conditions and geometries between MATLAB R2009a and COMSOL 3.5a creates some difficulties, when the geometry changes from one simulation step to the other with growing ice deposit. Therefore, a scheme is developed to allow for allocating boundary conditions in models with changing geometries in COMSOL 3.5a and presented in [157].

3.1.2 Model Geometry

Figure 3.2 shows the two dimensional model including a conductor bundle and ice deposits surrounded by a fluid domain. The model dimensions are chosen to provide enough clearance between the external boundaries and the iced cable. Thus, even for the largest presumed blockage in the flow, the influence of the boundaries on cable and ice body is negligible. Simulation runs were also done with smaller and higher blockages. The chosen blockage of less than 5 % proved to avoid effects of the boundaries on the flow. Furthermore, a blockage of 5 % is considered to be sufficiently small to have no influence on the results in common wind tunnel experiments [170]. At the inlet and outlet boundaries as well as on the upper and lower boundary the velocity is set to be equal to a free stream velocity. Cable and ice surface are

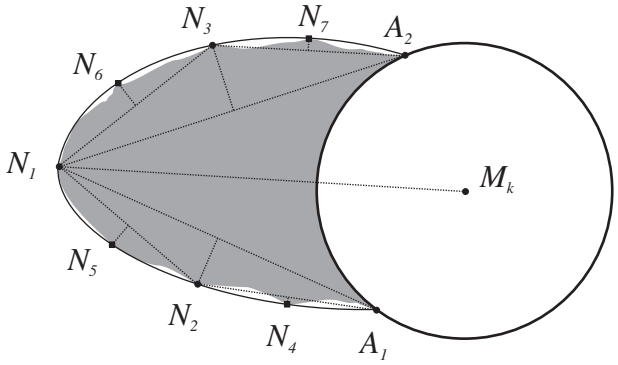

Figure 3.3: Algorithm to approximate the surface of an ice deposit, with supporting points (N_i), contact points of ice and cable surface (A_1, A_2) and centre of the cable (M_k).

modelled as a solid wall, where the velocity and temperature profile at the cable and ice surface are described by wall functions. Furthermore, a pressure boundary constraint is applied at the four external corners of the fluid domain. The thermal boundary conditions at the exterior boundaries are a predefined temperature at inlet, upper and lower boundary. The outlet allows for convective heat transfer. More details on the boundary conditions are given in section 3.2 and 3.4.

To develop an icing algorithm capable of simulating accretion on a conductor bundle, we focus on two cables in a tandem arrangement as it is shown in figure 3.2. If the algorithm proves successful for two cables, it can easily be applied to other bundle geometries with more cables. Power transmission lines are also constructed with bundles of three, four or even more cables. More details on the design of transmission lines are given in [55].

The ice surface calculated by the icing model often has coarse uneven areas. Thus, a fine resolution of the surface can lead to problems with the meshing algorithm and convergence of the solver. The mesh algorithm may fail due to a large aspect ratio of uneven areas compared to the whole domain. And the solver may not reach convergence due to pointed mesh element connections at the ice surface. However, resolving the coarse areas of the surface only has a small impact on the computation of the ice deposit. Therefore, an algorithm is developed to approximate the ice surface using splines to achieve geometry with continuous curvature already presented in [159]. Figure 3.3 shows how the algorithm works. First, the centre of the cable (M_k), the contact points of the ice and cable surface (A_1 and A_2) and the point furthest away from the cable (N_1) are determined. Then the algorithm evaluates the distance between neighbouring points and between the connecting line and the ice surface. If one of these limits is exceeded, a new point (N_i) is inserted. The algorithm also works in case of a closed ice surface, where A_1 and A_2 are at identical coordinates. If the cable, due to weak torsional stiffness, rotates under the eccentric ice load during the icing process, the ice can grow around the entire circumference of the cable.

3.2 Fluid Dynamic Model

3.2.1 Fundamentals of Fluid Dynamics

A flow is described by a set of state equations, namely the continuity, the momentum and the energy equation. The term Navier-Stokes equation originally meant only the momentum equation, but in recent literature it is also used for the whole set of state equations. These equations can allow for viscous and thermal effects and therefore they can describe turbulent and compressible flows. For many applications it is possible to simplify the problem by considering an incompressible flow. Furthermore, it is possible to model viscous properties of a flow by relating velocity gradients and shear stresses.

Viscosity of a fluid causes the formation of boundary layers, the separation of vortices and can lead to a transition from laminar to turbulent flows. In a laminar flow the fluid streams in parallel layers, which do not mix. A turbulent flow is characterised by stochastic velocity fluctuations. The kinetic energy in the turbulent flow is transferred from larger to smaller vortex structures and eventually dissipated.

A direct numerical simulation (DNS) of turbulent flows requires a very fine three-dimensional grid, because turbulences are generally three-dimensional and also small scales of a turbulent flow are important. Resolving all spatial and temporal scales of a turbulent flow is only possible for small Reynolds numbers even with high performance computers.

One strategy to reduce the numerical effort is a large eddy simulation (LES), which can use coarser grids. Large eddies are solved explicitly, smaller eddies are accounted for by subgrid-scale (SGS) models. This approach is based on the reasoning that larger scales transport the major part of kinetic energy and smaller scales are of a rather dissipative nature. Therefore, a LES resolves the large scales by the grid, while the small scales are accounted for by SGS models. Hence, LES uses special-averaging and consequently the lattice spacing has an impact on the simulation.

Another strategy to simplify the computation is to use the Reynolds-averaged Navier-Stokes (RANS) equations. This approach uses time-averaged flow variables, which significantly reduces the numerical effort. However, considering an incompressible flow, the momentum equation gets an additional, unknown term and is therefore not closed. This additional term accounts for inertial effects of momentum fluctuations that vanish due to time-averaging of flow variables. The influence of these so-called Reynolds stresses on the mean flow is similar to the effect of viscous stresses. Turbulence models are used to describe their effect on the flow in order to close the equations.

Dimensionless Quantities for Fluid Dynamics

Dimensionless quantities are widely used in fluid mechanics to characterise flow properties. In the following two quantities are presented that are useful to describe flows around conductors. The Reynolds number gives a measure of the nature of the flow while the Strouhal number characterises the transient behaviour of the stream. Both are already mentioned in section 2.5, but for formal reasons they are stated here again.

Reynolds number:
The Reynolds number is the ratio of inertial to viscous forces of a flow and it thereby gives a measure of the flow condition:

$$Re = \frac{\rho \cdot u \cdot d}{\mu} \tag{3.1}$$

where ρ is the density of the fluid, u the flow velocity, d the characteristic length and μ the dynamic viscosity. The characteristic length is used to relate the spatial extension of the geometry to the fluid properties. Streams with equal Reynolds numbers and flow conditions show the same behaviour. In general, laminar flows have smaller Reynolds numbers and above a critical Reynolds number the flow turns into a turbulent regime.

Strouhal number:
The Strouhal number describes the transient flow mechanisms based on the vortex shedding frequency f and the ratio of the characteristic length and the flow velocity:

$$St = f \cdot \frac{d}{u} \tag{3.2}$$

A Strouhal number of 0.2 is a good approximation for cylindrical structures such as a cable in wind engineering problems (cf. section 2.5.1).

The Navier-Stokes Equations for an Incompressible Flow

The Navier-Stokes equations for an incompressible flow assume a constant density, which is a reasonable approach for airflows around conductor bundles. Incompressibility is a flow property. Although, air is obviously compressible, airflows can behave incompressible for low mach numbers. Assuming an incompressible flow allows us to decouple the continuity and the momentum equation from the conservation of energy [177]. It also includes assuming the viscosity to be constant. Hence, the continuity equation of an incompressible flow becomes:

$$\nabla \mathbf{u} = 0 \tag{3.3}$$

where $\mathbf{u}$ is the velocity vector. Assuming the fluid to be Newtonian and adding the Stokes assumption the stress tensor is:

$$\tau = \mu \left(\nabla \mathbf{u} + (\nabla \mathbf{u})^T \right) \tag{3.4}$$

Therefore the momentum equation is defined as:

$$\rho \frac{\partial \mathbf{u}}{\partial t} + \rho \left(\mathbf{u} \cdot \nabla \right) \mathbf{u} = -\nabla p + \nabla \cdot \mu \left(\nabla \mathbf{u} + (\nabla \mathbf{u})^T \right) + \mathbf{F} \tag{3.5}$$

where p is the pressure and $\mathbf{F}$ is the force vector acting on the fluid volume. The conservation of energy is solved independently from the continuity and momentum equation in the heat transfer model presented in section 3.4.

3.2.2 Model Equations for Fluid Dynamics

The airflow around the conductor bundles is simulated with a Reynolds averaged Navier-Stokes model in combination with a standard k-ε turbulence model. The flow is considered incompressible and the computation is stationary. As already mentioned, assuming an incompressible flow allows us to decouple the continuity and momentum equations from the energy equation. Therefore, this section explains modelling of the continuity and momentum equations.

The energy equation is used to determine the temperature distribution in the system and is explained in section 3.4. An overview on the background of RANS modelling is given by Zienkiewicz et al. [177].

Reynolds Averaged Navier-Stokes Equations

The time averaged Navier-Stokes equations are used, because it is computationally too demanding to resolve the smallest turbulent scales. To understand the idea of RANS modelling it is helpful to express the flow variables in two parts. One component accounts for a time-average and another for fluctuations around the average. This splitting into a time-average and a fluctuation variable is referred to as Reynolds decomposition:

$$\phi = \bar{\phi} + \phi' \tag{3.6}$$

where $\bar{\phi}$ is the time-average and ϕ' the fluctuating component. When substituting them in the time-averaged state equations the average of the fluctuating component is equal to zero. Thus, the averaged incompressible flow satisfies the same continuity equation as the instantaneous flow. Substituting the decomposed flow variables in the time-averaged continuity and momentum equations leads to an expression for an averaged flow. For an incompressible

stream the continuity equation is the same as for an averaged and an instantaneous flow. The momentum equation on the other hand gets an additional unknown term. The averages of fluctuating components are equal to zero, but the product of fluctuating velocity components is not necessarily equal to zero. The stationary momentum equation is then given by:

$$\rho \mathbf{U} \cdot \nabla \mathbf{U} = -\nabla p + \nabla \cdot \mu \left(\nabla \mathbf{U} + (\nabla \mathbf{U})^T \right) - \nabla \cdot \left(\rho \overline{\mathbf{u}' \otimes \mathbf{u}'} \right) \tag{3.7}$$

where the last term on the right hand side is unknown. Considering the momentum equation this term acts as stresses and is therefore referred to as Reynolds stresses. Since they are not known, the equation is not closed. In order to solve the problem this term has to be modelled. The approach used here is based on the Boussinesq approximation. It assumes the Reynolds stresses to depend linearly on the velocity gradients, similar to shear stresses in a viscous fluid. With this assumption Reynolds stresses are reduced to an expression depending on the turbulent kinetic energy and the turbulent viscosity, also called eddy viscosity. The latter depends on the local turbulences and is not a fluid property like the molecular viscosity. The fact that the Reynolds stresses depend on the turbulences in the flow of the same scale that we are interested in, makes the closure difficult. Moreover, the Boussinesq approximation is not a very accurate approximation at curved boundaries or in case of boundary layer separation [167], which both occur in ice accretion. However, non-linear eddy viscosity models are very complex and therefore not included in common simulation tools. Hence, they are beyond the scope of the ice accretion model. More details on this challenging aspect of turbulence modelling are given in [16], for example.

Consequently, the flow is described by the following continuity and momentum equations. The time-averaged continuity equation is defined as:

$$\nabla \mathbf{U} = 0 \tag{3.8}$$

where $\mathbf{U}$ is the averaged velocity vector. The time-averaged momentum equation is given by:

$$\rho \left(\mathbf{U} \cdot \nabla \right) \mathbf{U} = -\nabla p + \nabla \left((\mu + \mu_T) \cdot \left(\nabla \mathbf{U} + (\nabla \mathbf{U})^T \right) \right) \tag{3.9}$$

where μ_T is the eddy viscosity, which in our case is determined by the standard k-ε turbulence model.

The Standard k-ε Turbulence Model

The eddy viscosity is determined by the standard k-ε turbulence model and is defined as:

$$\mu_T = \rho \cdot C_\mu \cdot \frac{k^2}{\varepsilon} \tag{3.10}$$

where $C_\mu = 0.09$ is a model constant, k the turbulent kinetic energy and ε the turbulent dissipation rate. The transport of k and ε in the flow is described by the flowing equations:

$$\begin{aligned}\rho\mathbf{U}\cdot\nabla k &= \nabla\cdot\left(\left(\mu+\frac{\mu_T}{\sigma_k}\right)\nabla k\right)+\frac{1}{2}\cdot\mu_T\left(\nabla\mathbf{U}+(\nabla\mathbf{U})^T\right)^2-\rho\varepsilon \\ \rho\mathbf{U}\cdot\nabla\varepsilon &= \nabla\cdot\left(\left(\mu+\frac{\mu_T}{\sigma_\varepsilon}\right)\nabla\varepsilon\right)+\frac{1}{2}C_{\varepsilon 1}\frac{\varepsilon}{k}\cdot\mu_T\left(\nabla\mathbf{U}+(\nabla\mathbf{U})^T\right)^2-\rho C_{\varepsilon 2}\frac{\varepsilon^2}{k}\end{aligned} \tag{3.11}$$

where the model constants are $C_{\varepsilon 1} = 1.44$, $C_{\varepsilon 2} = 1.92$, $\sigma_k = 1$ and $\sigma_\varepsilon = 1.3$. This set of model constants is commonly used and was developed by Launder and Sharma and published in Wilcox [167]. The turbulence model overestimates the production of turbulent kinetic energy at the stagnation point, the so-called stagnation point anomaly [34]. Hence, the fluid behaves more viscously than it should and the recirculation bubble dissipates faster.

Moreover, an important assumption made by this turbulence model is that turbulence formation and dissipation is in equilibrium within the boundary layer, which is not always true in real systems. Consequently, the spatial extension of the wake is usually underestimated [34].

The extension of the wake is expected to have a significant influence on the ice formation process on the downstream cable. Therefore, the simulation results can underestimate the influence of the wake on the downstream cable. Hence, any result indicating an effect of the tandem arrangement on the icing process on a downstream cable supports the assumption that there is such an effect.

Velocity Boundary Layer

The standard k-ε turbulence model is developed for a turbulent flow distant from solid walls and is therefore not valid close to a solid surface. In near wall regions the fluctuations are dampened and the viscosity of the fluid becomes dominant. Consequently, the model has to be modified. There are basically two strategies to model the turbulent flow in this region.

The first is a low Reynolds number simulation, which requires a very fine mesh to resolve the viscous sublayer of the velocity boundary layer. It solves the RANS equations down to the wall and accounts for the increasing effect of the viscosity with damping functions in the transport equations for the turbulent kinetic energy and the turbulent dissipation.

The other strategy is to bridge the region close to the wall. The domain of the RANS equations does not reach down to the wall. Instead a wall function is used to describe the flow in the near wall region. This approach is the one adopted here.

A wall function defines the velocity tangential to the surface as a function of the distance to the wall without considering pressure gradients. The non-dimensional velocity profile in the

logarithmic region of the boundary layer is described by:

$$u^+ = \frac{1}{\kappa} \cdot \ln\left(y^+\right) + C^+ \tag{3.12}$$

where $\kappa = 0.42$ is the Kármán's constant and $C^+ = 5.5$ a model constant for smooth surfaces. The dimensionless velocity parallel to the wall u^+ and the dimensionless boundary layer depth y^+ are defined as:

$$\begin{aligned} u^+ &= \frac{u}{u_*} \\ y^+ &= \frac{\rho \cdot u_*}{\mu} \cdot \delta_w \end{aligned} \tag{3.13}$$

where δ_w is the velocity boundary layer depth and u_* is the friction velocity. The latter depends on the shear stress at the surface τ_w and is given by:

$$u_* = \sqrt{\frac{\tau_w}{\rho}} \tag{3.14}$$

The shear stress at the wall is defined by the velocity gradient normal to the wall and the dynamic viscosity of the fluid:

$$\tau_w = (\mu + \mu_T) \cdot \frac{\partial u}{\partial y} \tag{3.15}$$

Wall functions describe the effect of shear stresses at a surface on the flow. The flow computation in the RANS domain and the calculation of the wall functions are coupled. Therefore, it is essential to chose the boundary layer thickness in a way that y^+ lies in the valid range for a logarithmic wall function, which means that $30 \leq y^+ \leq 300$ has to be fulfilled. Otherwise a solution is not correct even though it might converge.

Boundary Conditions for the RANS Model

The boundary conditions at the external boundary of the fluid domain are velocity and pressure conditions. At the inlet and outlet boundaries the velocity is set to be equal to the free stream velocity. Also, at the remaining external boundaries at the top and the bottom of the domain the velocity is predefined as free stream velocity. In addition pressure constraints are applied at the vortices in the corners of the domain, which ease the solution procedure of the solver. Cable and ice surface are solid walls and the velocity profile of the boundary layer forming at the surface is modelled using a logarithmic wall function. An estimation of the boundary layer thickness is required to ensure the validity of the wall function, as described in section 3.2.2. Predicting the

boundary layer thickness of a cylinder with ice deposit is not trivial. Achenbach [1] presented a distribution of the displacement thickness on a cylinder in a cross flow for subcritical Reynolds numbers derived from investigations of Blasius and Schönauer. The displacement thickness is the distance from the surface to a parallel reference plane, which devides the volumetric stream in the boundary layer into two equal parts. Based on the distribution of the displacement thickness it is possible to estimate the boundary layer thickness, considering that it is about a tenth of the boundary layer [131].

Hence, the boundary layer thickness of a cylinder in a cross flow for moderate Reynolds numbers is estimated by:

$$\delta_w = 10 \cdot \frac{d}{\sqrt{Re}} \tag{3.16}$$

where d is the characteristic length of the iced conductor. The subcritical flow regime matches the conditions of conductor icing. Furthermore, the equation yields adequate results even when the shape of the iced cylinder differs from the experimental setup.

3.2.3 Discussion of the Fluid Dynamic Model

The flow field is determined by a two-dimensional stationary RANS simulation. It is a less demanding approach. One might argue that LES is superior to RANS. But the deficits of the RANS approach are minor when considering the whole uncertainties of the ice accretion model.

Since the model does not allow for transient effects of the flow field also multiphase flow and head balance computation are limited to being stationary. As long as no liquid water film on the ice surface is modelled the latter has probably no effect. But the former presumably has an effect in case of in-cloud icing or wet snow accretion. Therefore, a transient calculation would be desirable. A transient simulation would affect the wake and therefore influence the ice formation on downstream cylinders. However, this aspect as well as a three-dimensional computation of the flow field is left for further research. A three-dimensional flow computation is not required, because the icing model cannot account for three-dimensional characteristics of ice growth.

The RANS equations are closed with a standard k-ε turbulence model. It is known for an extensive production of turbulent kinetic energy at stagnation points, which leads to an underestimation of the wake [34]. Consequently, the effect of the wake on the ice formation on a downstream conductor is also underestimated.

Other turbulence models may overestimate the extension of the wake and therefore its effect on the ice accretion, like the k-ω mode for instance. Hence, the chosen approach is on the safe side, which is beneficial for investigating whether there is an effect of tandem arrangement of conductors on the ice accretion or not.

The computation of the RANS equations is coupled with wall functions to model the boundary layer. These functions require an adequate estimation of the boundary layer thickness to ensure a convergent solution. If y^+ extensively exceeds the feasible range, the computation does not converge. The model can find a solution for small violations of the wall function constraint. In this case no measurable effect on the ice accretion is observed due to this violation. The ice accretion model is robust against errors in the boundary layer approximation. Approaches similar to the one presented here for approximating of the boundary layer thickness are already successfully used in other models as in [150], for example.

The applied wall model does not account for adverse pressure gradients in the boundary layer, meaning that the pressure decreases in flow direction. This occurs in the wake of a cylinder, for example. An approach to model this effect is not available in our model. An advanced wall model allowing for such effects is presented in [87], for example.

The quality of the finite element mesh is essential for a convergent solution and a correct result. As we will see later on, three different meshes are compared to find an appropriate mesh resolution. In order to focus the computational power where it is required, adaptive mesh refinement is used. It significantly reduces the computational effort of the model. Velocity, velocity gradient and vorticity of the flow were tested as error estimation for the mesh refinement. The test showed no differences in computed separation angle or extension of the wake. However, a mesh generated with vorticity as error estimate required slightly less elements and was therefore chosen.

In order to verify the flow computation the software package is tested with the DFG-Benchmark test for laminar flows [130]. Furthermore, the model is tested by comparison with experimental data of a flow passing a single cylinder. And simulation results of a flow around a generic conductor bundle under appropriate flow conditions are presented.

The benchmark test includes a stationary and a transient calculation of a two-dimensional flow around a cylinder with Reynolds numbers of 20 and 100. In the stationary case pressure differences between the stagnation point and the subtend point on the cylinder surface as well as the length of the recirculation zone behind the cylinder are measured. Furthermore, aerodynamic lift and drag coefficients are determined. In the transient case, also the Strouhal number is determined. A target range for all these quantities is given by the test scheme. Three meshes are used for the examination. The investigation starts with a mesh of coarse resolution and then the number of mesh elements is respectively increased by a factor of two. The solver satisfied the performance criteria for both meshes with higher resolution. Only when the coarsest mesh is used the solver fails to adequately predict the pressure on the stagnation and subtend point on the cylinder.

However, the air flow around conductor bundles is commonly characterised by Reynolds numbers in the magnitude of 10^3 to 10^4. Hence, the flow properties differ from those of the benchmark test. Moreover, the test does not account for tandem arrangement of conductors. Therefore, a comparison with other investigations is required to verify the model.

The separation angle of the boundary layer and the length of the recirculation bubble are chosen to evaluate the numerical model. These quantities are useful to characterise flow properties, especially when the extension of the wake is of interest. Experiments show that a cylinder in a flow with subcritical Reynolds numbers has a separation angle $\varphi_A = 81^\circ$ [131]. Also the length of the recirculation bubble is determined by experiments with two different measurement techniques. For a Reynolds number of 140,000 two different results are presented in the literature $x/d = 1.37$ and $x/d = 1.51$, where x is the distance behind the cylinder and d is the cylinder diameter [25].

The model is tested with three different meshes: a coarse one, a fine one and a very fine mesh. For an investigation of a single cylinder it leads to 55550 DOFs, 152084 DOFs and 357343 DOFs, including adaptive mesh refinement. The model predicts the separation angle to be $\varphi_A = 84^\circ$ for all three meshes. For the coarse mesh the near wake is determined to be $x/d = 0.32$. In contrary to this, computations with the two finer meshes lead to $x/d = 0.34$. The near wake is not to be confused with the wake. The former describes the recirculation bubble and the latter is the region where the flow is disturbed downstream of a solid body.

The number of DOFs seems to have no effect on the separation angle. This is probably due to the adaptive mesh refinement, which increases the number of elements in error prone regions such as the separation point, for instance. Compared to the experiment, the separation angle is overestimated. The deviation is not surprising, since turbulence models commonly have difficulties to correctly model massive separation as it occurs on cylinders. Moreover, due to the stagnation point anomaly the pressure distribution on the cylinder is not well predicted and hampers a precise prediction of the separation angle.

The other parameter, the near wake, is significantly underestimated for all three meshes. Furthermore, the adaptive mesh refinement does not lead to the same results for all meshes. The first seems to arise mainly from the turbulence model, which overestimates the production of turbulent kinetic energy at the stagnation point and therefore underestimates the length of the near wake. The second is probably due to the fact that the error estimator is not able to adequately represent the flow properties governing the extension of the wake.

Figure 3.4 shows the velocity distribution in the wake of a single cylinder determined by numerical models and an experiment. The comparison of experimental numerical results is satisfying. Two additional simulations are displayed in figure 3.4 to mark the range of Reynolds numbers occurring in flows around conductors. Here we consider a conductor with a diameter of 40 mm and a wind velocity of 5 m/s and 15 m/s. The separation is predicted by model to $\varphi_A = 84^\circ$ and the length of the near wake is determined to $x/d = 0.26$ and $x/d = 0.13$. Thus, the extension of the recirculation bubble decreases for smaller Reynolds numbers, which is not correct in this range. This phenomenon is difficult to simulate and commonly not well predicted.

Finally, cylinders in a tandem arrangement are examined. Unfortunately, no experimental reference data is available to review this aspect. However, figure 3.5 shows the velocity

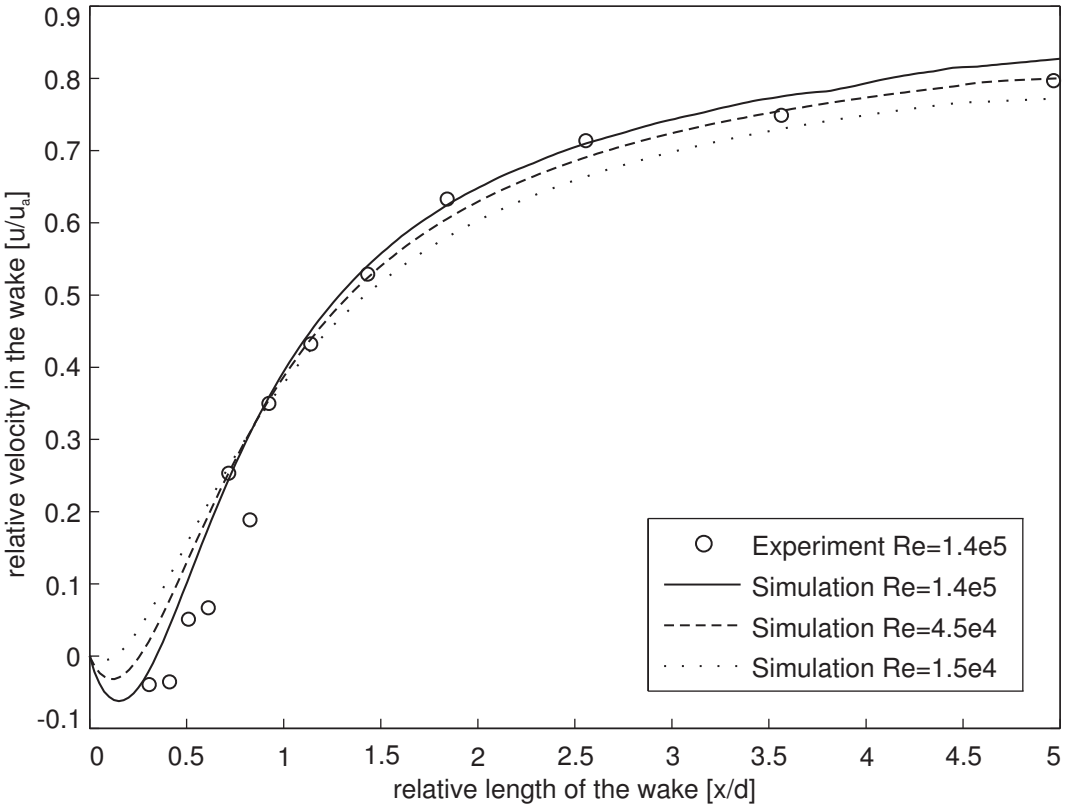

Figure 3.4: Horizontal velocity distribution in the wake of a cylinder along a centreline. Experimental results $(\circ)$ ([14] from [151]) at $Re = 140\,000$ compared to simulations with $Re = 140\,000$ $(-)$, $Re = 45\,000$ (- - -) and $Re = 15\,000$ $(\cdots)$.

distribution between two cylinders arranged in a tandem. They represent a generic conductor bundle, with a conductor diameter of 40 mm and a typical spacing for conductor bundles of 400 mm is used [55]. Obviously, the time-averaged velocity field shows a similar velocity distribution to those of a single cylinder presented in figure 3.4. Contrary to the single cylinder the velocity in the wake increases slightly slower and eventually drops in front of the downstream cylinder. Also here the near wake enlarges with increasing Reynolds numbers. But the wake behind the upstream cylinder reaches far behind the down stream cylinder. Moreover, the ratio of the velocity in the wake and the ambient velocity recovers more slowly when the Reynolds number increases.

All previously discussed simulations considered a turbulence intensity of 0.05 at the inflow to represent the conditions in a wind tunnel. When the turbulence intensity of the incoming flow is higher, the extension of the recirculation zone is expected to enlarge. To examine this effect, a flow around a single cylinder at a Reynolds number of 15,000 and a turbulence intensity of 0.1 is simulated. Again it predicts a separation angle of $\varphi_A = 84^\circ$ and the recirculation zone enlarges to $x/d = 0.37$.

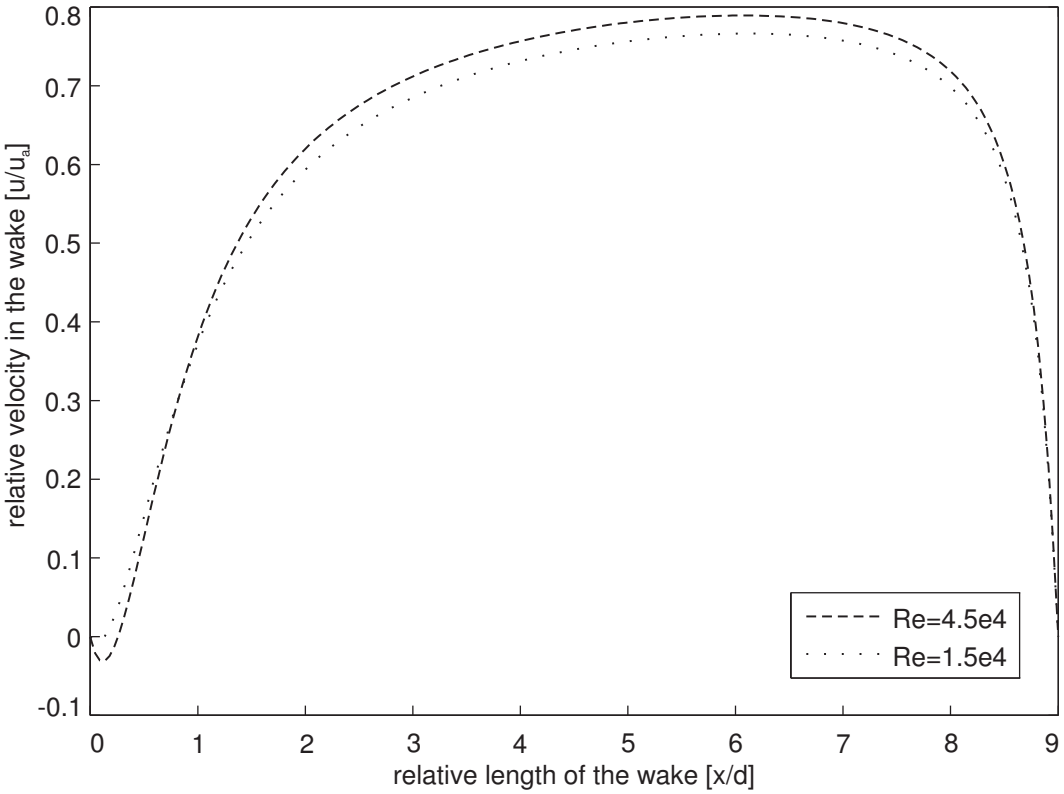

Figure 3.5: Horizontal velocity distribution between cylinders in a tandem arrangement with a common spacing of conductors in a bundle, measured along a centreline for $Re = 45000$ (- - -) and $Re = 15000$ ($\cdots$).

Modelling flows around cylinders is a challenging task and under ongoing research, but the model is adequate to simulate the flow around conductor bundles, as it is required for this investigation.

3.3 Multiphase Flow Model

3.3.1 Fundamentals of Multiphase Flow

A multiphase flow is a mixture of several different gaseous, liquid or solid phases. Such flows are a very complex phenomenon. It is possible to distinguish different categories of multiphase flows. Those categories are defined by the interaction mechanisms between the individual phases, which allows for simplified modelling approaches. A detailed overview of multiphase flows with theoretical background and modelling approaches is given by Crowe et al. [21]. In the following some principles and fundamental definitions of multiphase flows are explained in order to ease the understanding of the implemented multiphase flow model.

A two phase flow is composed of a continuous phase and a disperse phase, also known as carrier and discrete phase. Disperse phase means that discrete elements are not connected. Hence, in a mixed stream of air and precipitation the air is considered as continuous phase and the precipitation as disperse phase.

Volume Fraction and Density

The volume fraction of the disperse phase is given by:

$$\alpha_D = \lim_{V \to V_0} \frac{V_D}{V} \tag{3.17}$$

where V_D is the volume of the disperse phase in the volume V and V_0 is the volume containing a stationary average of the disperse phase. Accordingly, the volume fraction of the continuous phase is defined as:

$$\alpha_C = \lim_{V \to V_0} \frac{V_C}{V} \tag{3.18}$$

The sum of the volume fraction must obviously be equal to unity:

$$\alpha_D + \alpha_C = 1 \tag{3.19}$$

The bulk density of the disperse phase is defined by:

$$\overline{\rho_D} = \lim_{V \to V_0} \frac{m_D}{V} \tag{3.20}$$

where m_D is the mass of the disperse phase. The bulk density is related to the material density ρ_D of the droplets or particles by:

$$\overline{\rho_D} = \alpha_D \cdot \rho_D \tag{3.21}$$

Accordingly, the bulk density of the continuous phase is:

$$\overline{\rho_C} = \alpha_C \cdot \rho_C \tag{3.22}$$

The sum of the bulk densities of both phases is the density of the entire multiphase flow:

$$\rho = \overline{\rho_D} + \overline{\rho_C} \tag{3.23}$$

Response Time and Stokes Number

The time interval necessary for a phase to adapt to changes in velocity or temperature in the other phase is an important parameter to characterise multiphase flows. This so-called response time characterises the phase interaction in the flow. The momentum response time measures the interval a droplet requires to adapt to changing flow velocities. A variation in droplet temperature on the other hand is negligible here. Droplet and ambient temperature are considered to be in equilibrium for the relatively small model domain. Therefore, the model considers only the momentum response time, which is derived from the momentum equation considering drag force on a spherical particle in a fluid:

$$m_p \cdot \mathbf{a}_p = -C_D \cdot A_p \cdot \frac{\rho_f}{2} \cdot |\mathbf{u}_{rel}| \cdot \mathbf{u}_{rel} \tag{3.24}$$

where m_p is the particle mass, a_p the particle acceleration, C_D the drag coefficient, A_p the cross-section of the particle, ρ_f the fluid density and $\mathbf{u}_{rel}$ the relative velocity between particle and fluid. With the particle Reynolds number Re_p defined as:

$$Re_p = \frac{|\mathbf{u}_{rel}| \cdot d_p \cdot \rho_f}{\mu} \tag{3.25}$$

where μ is the fluid viscosity and d_p is the particle diameter. Consequently, equation 3.24 becomes:

$$\mathbf{a}_p = -\frac{18 \cdot \mu}{\rho_p \cdot d_p^2} \cdot \frac{C_D \cdot Re_p}{24} \cdot \mathbf{u}_{rel} \tag{3.26}$$

where ρ_p is the density of a particle. For low relative velocities the particle Reynolds number tends towards zero and the flow is described by the Stokes law. Hence, the second term of equation 3.26 approaches unity. The first term represents the reciprocal time and is used to define the velocity response time:

$$\tau_D = \frac{\rho_p \cdot d_p^2}{18 \cdot \mu} \tag{3.27}$$

Even though the response time was derived for very small Reynolds numbers it is also valid for higher numbers [21].

The degree of interaction between the continuous and the disperse phase is described by the so called Stokes number. It relates the response time of particles τ_D to the characteristic time of the carrier phase τ_C [21]:

$$Stk = \frac{\tau_D}{\tau_C} \tag{3.28}$$

If the Stokes number is low, the response time of a particle is smaller than the characteristic time of the fluid flow. Thus, a particle has enough time to adapt to the flow velocity. And on the contrary, when the particle response time is larger than the characteristic time of the flow, the particle motion is only slightly affected by changes in the flow. In the scope of atmospheric icing low as well as high Stokes numbers occur. The response time of cloud droplets is relatively low and thus the droplets follow the air stream. Large rain drops, on the other hand, need more time to adapt to the air flow. Consequently, they are hardly affected by local fluid forces. Snow flakes have a larger response time than cloud droplets. Due to varying density depending on the liquid water content of the flake and due to their filigree structure the interaction of air and snow is hard to define precisely.

Disperse and Dense Flow

A multiphase flow can either be described as disperse or dense. While a disperse flow is controlled by the fluid force acting on the particles, in a dense flow, the collision of particles govern the motion of the disperse phase. The flow is disperse when the particles have enough time to respond to the local fluid forces. Hence, a disperse flow is considered for:

$$Stk = \frac{\tau_D}{\tau_C} < 1 \tag{3.29}$$

The flow is dense, when the particles do not have sufficient time to respond to the flow. Then the characteristic time of the flow is smaller than the response time of the particles. Thus, it is defined by:

$$Stk = \frac{\tau_D}{\tau_C} > 1 \tag{3.30}$$

Furthermore dense flows are subdivided into collision- and contact-dominated flows. In collision-dominated flows the particle motion is governed by the collision of particles, as is the case in fluidised beds. In contact-dominated flows, continuous contact between particles controls their motion, as it occurs in granular flows. A mixed stream of air and natural precipitation as modelled here is commonly considered as a disperse flow [21].

Size Distribution and Particle Shape

Natural precipitation is obviously not uniform. The particle size is an important parameter that affects the behaviour of the disperse phase significantly. Therefore, it is important to know the distribution of particle sizes in a flow. In general, the occurrence of different particles in a flow is described by particle or droplet spectra. Spherical particles are easily classified by their diameter. For non-spherical particles an equivalent diameter is commonly defined. The term spectrum is associated with frequencies and one might argue whether it is correct

to use it, when defining the fraction of certain particles in a flow. However, particle sizes are measured and classified by occurrence frequencies of different particle sizes in a flow and hence the information is gathered in a particle or droplet spectrum. The droplet spectra of spray flows like natural precipitation are commonly characterised by their medium volume diameter (MVD). This diameter, also called Sauter mean diameter, is determined by the ratio of particle volume distribution to surface area distribution [21]:

$$MVD = \frac{\int_0^{d_{\max}} d_p^3 \cdot f_n(d_p)\, dd_p}{\int_0^{d_{\max}} d_p^2 \cdot f_n(d_p)\, dd_p} \tag{3.31}$$

where f_n is the differential quantity of the frequency function of the particle diameters.

Phase Coupling

Phase coupling can take place through mass, momentum and energy transfer between the phases [21]. Mass coupling refers to changes in the mass balance by evaporation in and condensation from the carrier phase for example. It has a negligible effect, when the volume fraction of the disperse phase is small, such as it is the case in natural precipitation [21]. Momentum coupling accounts for forces acting between different phases. Meaning drag forces acting on the particle and the wake forming in the fluid behind a particle, for example. Energy coupling accounts for transfer of kinetic and heat energy. Beside the type of coupling also the degree of phase coupling is important, when a multiphase flow is analysed. Disperse flows can include four different levels of phase coupling. The first level is called one-way coupling and is usually used to simulate sparse flows. Here the continuous phase affects the motion of the disperse phase, but there is no vice versa effect. A particle follows the vortex in the fluid, but the vortex formation is not influenced by the presence of particles, for example. The next level is the two-way coupling. It additionally includes the influence of particle motion on the continuous phase, such as increased turbulent dissipation due to a wake that forms behind a particle. Large particles tend to increase turbulence in the flow. Small particles have no effect or tend to decrease turbulence slightly. The turbulent dissipation probably increases at low particle Reynolds numbers. Larger particles have greater Reynolds numbers and hence stronger wakes, which may increase the turbulences. A turbulence model accounting for the presence of particles is successfully used in snow drift analysis [9], for example. Three-way coupling also takes into account that local disturbances of the fluid by a particle locally affect another particle's motion. A particle's wake drafts a trailing particle, for instance. Four-way coupling includes direct interaction among particles, such as trajectory deflection of colliding particles. Note that in four-way coupling for disperse flows the particle collision does not dominate the overall particle motion. Dense flows are defined in most cases as four-way-coupled flows.

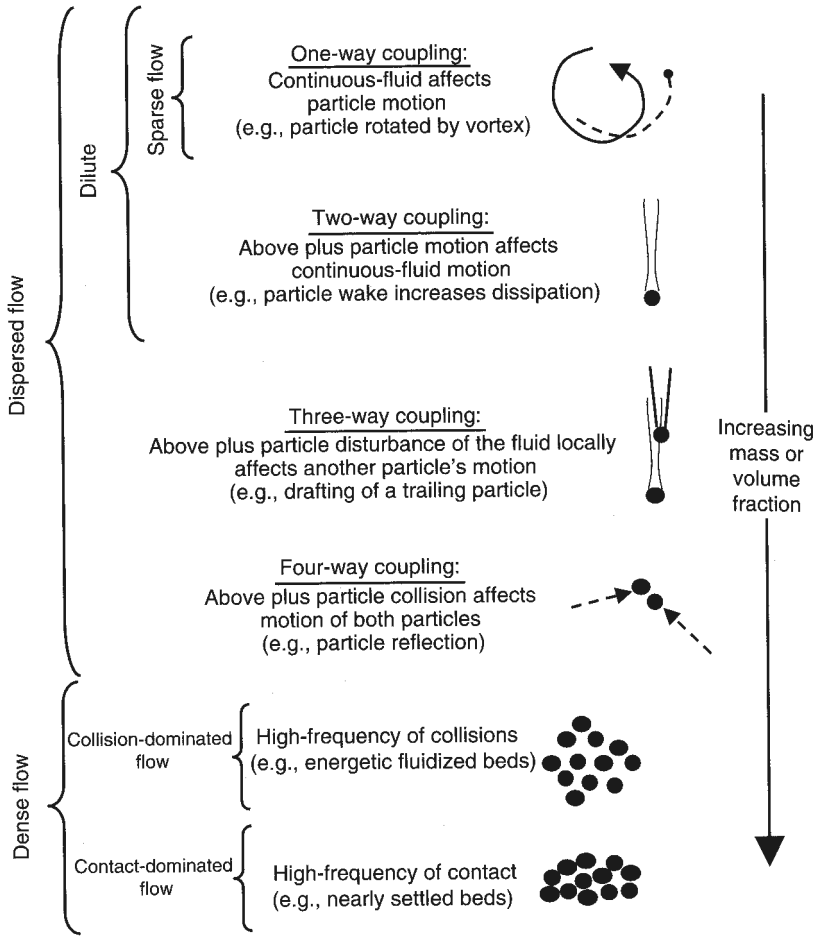

Figure 3.6: Degree of phase coupling for dense and disperse flows [21].

They are either considered as collision-dominated or contact-dominated flows. The former is defined by a high-frequency of particle collisions, the latter by nearly continuous contact between particles. Collision-dominated flows are fluidized beds, for example. On the other hand, granular flows are dominated by particle contact, for instance.

Lagrangian Versus Eulerian Approach

A Lagrangian or Eulerian approach can be used to model individual phases. The first considers a phase as discrete particles while the second describes it as a continuum. This already indicates that for modelling a two-phase flow a combination of an Eulerian approach for the continuous phase and a Lagrangian approach for the disperse phase is useful. In general, the Lagrangian approach is preferable when impact of particles on a surface, collision among particles or the behaviour of particles in a counter flow are investigated [21]. The Eulerian approach is computationally more efficient, but due to numerical diffusion high density gradients in the

disperse phase are less reliably predicted. Furthermore the discretisation of phases as individual fluids is said to be more accurate for two-way coupled flows [21]. The modelling approach also affects the impact statistic of particles on a surface. An Eulerian model leads to continuous collision efficiency, which is more suitable for dense flows. A Lagrangian approach can show discontinuous collision efficiency, which resembles dilute flow more closely. The computation of every single particle with the Lagrangian method is computationally expensive. Therefore, it is desirable to reduce the number of particles using a trajectory or a discrete element approach, for example. For dilute flows and stationary flow fields the trajectory approach is recommended [21]. It can be visualised as a stream tube limited by computed droplet trajectories. Particles are assumed to stream within each tube according to the computed particle trajectories. The number of trajectories is chosen large enough to characterise the behaviour of the flow sufficiently, but small enough to allow for an efficient calculation. Dense flows and unsteady flow fields are better described by the discrete element approach. It presumes that each computed particle movement represents the behaviour of a package of particles.

3.3.2 Model Equation for the Multiphase Flow

The multiphase flow of air and precipitation is modelled as Eulerian-Lagrange approach. An Eulerian approach is used to compute the flow field as it is described in detail in section 3.2. Based on the flow field the particle motion is determined by a Lagrangian trajectory approach, meaning that individual particle trajectories are computed for a given flow field. The mass flux of icing particles can be visualised as a stream tube starting from the undisturbed flow to the surface, limited by the computed droplet trajectories. Within each tube the particles stream from the undisturbed flow towards the surface. The following equations are used to model the mixed stream of air and precipitation droplets as a one-way coupled two-phase flow.

Particle Trajectory Calculation

The motion of the individual particles is described by Newton's second law, so the governing equation for the particle motion is:

$$m_p \cdot \mathbf{a}_p = \sum \mathbf{F} \tag{3.32}$$

where m_p is the particle mass, $\mathbf{a}_p$ particle acceleration and $\mathbf{F}$ the sum of drag, buoyancy and gravity force acting on the particle. Other forces acting on the particle are neglected and the particles are assumed to be spherical. Itemising the force vector leads to an expression for the aerodynamic drag force, depending on the relative velocity:

$$\mathbf{u}_{rel} = \mathbf{u}_p - \mathbf{U} \tag{3.33}$$

where $\mathbf{u}_p$ is the particle velocity vector and $\mathbf{U}$ is the averaged velocity vector of the fluid. Adding an expression to allow for the force due to density differences of particle and fluid we achieve the following equation:

$$m_p \cdot \mathbf{a}_p = -C_D \cdot A_p \cdot \frac{\rho_f}{2} \cdot |\mathbf{u}_{rel}| \cdot \mathbf{u}_{rel} - \rho_f \cdot V_p \cdot \mathbf{g} + \rho_p \cdot V_p \cdot \mathbf{g} \tag{3.34}$$

with C_D the drag coefficient, A_p the cross-section and V_p the volume of the particle, ρ_p the particle density, ρ_f the fluid density and $\mathbf{g}$ the gravity vector. Introducing the particle Reynolds into equation 3.34 and rearranging the equation leads to:

$$m_p \mathbf{a}_p = -\frac{C_D Re_p}{24} \cdot 3\pi \cdot d_p \cdot \mu \cdot \mathbf{u}_{rel} + \left(\rho_p - \rho_f\right) \cdot \frac{\pi \cdot d_p^3}{6} \cdot \mathbf{g} \tag{3.35}$$

where Re_p is the particle Reynolds number defined by:

$$Re_p = \frac{|\mathbf{u}_{rel}| \cdot d_p \cdot \rho_f}{\mu} \tag{3.36}$$

Particle Reynolds number and drag coefficient depend on the relative velocity of particle and fluid. For $Re_p << 1$, the drag coefficient is given by the Stokes's law:

$$C_D = \frac{24}{Re_p} \tag{3.37}$$

When the particle Reynolds number increases the Stokes's law is not longer valid. Therefore an approximation of the drag coefficient is derived from experimental tests. Such empirical equations are presented in the literature for a variety of applications. For atmospheric icing of structures due to cloud droplets, drizzle and rain drops the following set of equations was developed and published in [158]:

$$\begin{aligned}
\frac{C_D \cdot Re_p}{24} &= 1 - 0.391 \cdot Re_p^{0.3289} + 0.5648 \cdot Re_p^{0.4561} && for && 0 < Re_p \leq 10 \\
\frac{C_D \cdot Re_p}{24} &= 1 + 0.1767 \cdot Re_p^{0.6536} && for && 10 < Re_p \leq 200 \\
\frac{C_D \cdot Re_p}{24} &= 4.001 + 0.01052 \cdot Re_p^{1.048} && for && 200 < Re_p
\end{aligned} \tag{3.38}$$

The approximation is based on experiments by Langmiur and Boldgett [66]. Because they where preformed for aircraft engineering, the drag was tested over a wide range of particle Reynolds numbers, but for transmission line icing only the range of low Re_p is important. Therefore the formulae presented here are designed to fit low Re_p best. The equations have a coefficient of determination of over 99 % for $Re_p < 2000$. Beyond this range the accuracy decreases only slightly.

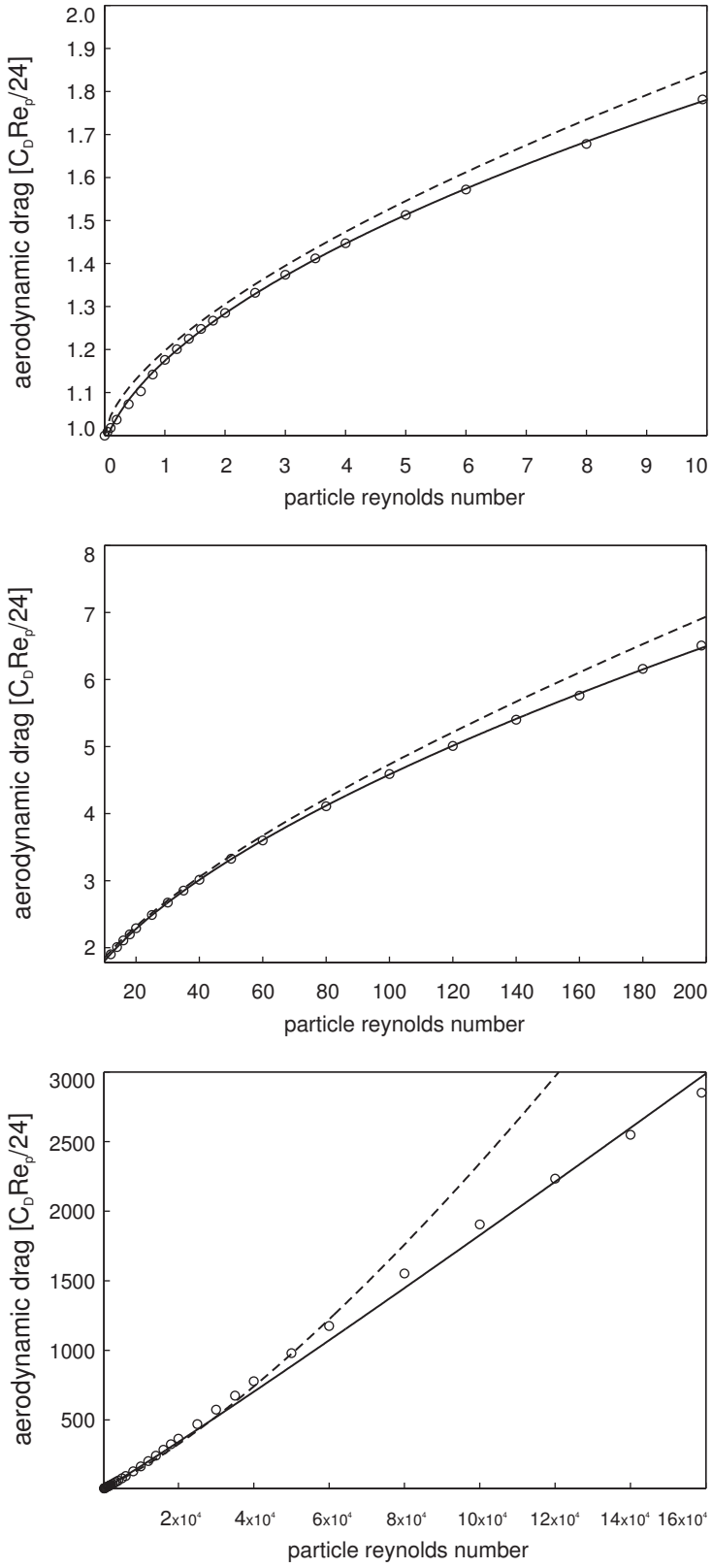

Figure 3.7: Experimental results $(\circ)$ and an empirical equation (- - -) published by Langmuir and Blodgett [66] are compared with the proposed approximation $(-)$ of the aerodynamic drag $(C_D Re_p/24)$ for Reynolds numbers of spherical particles (Re_p).

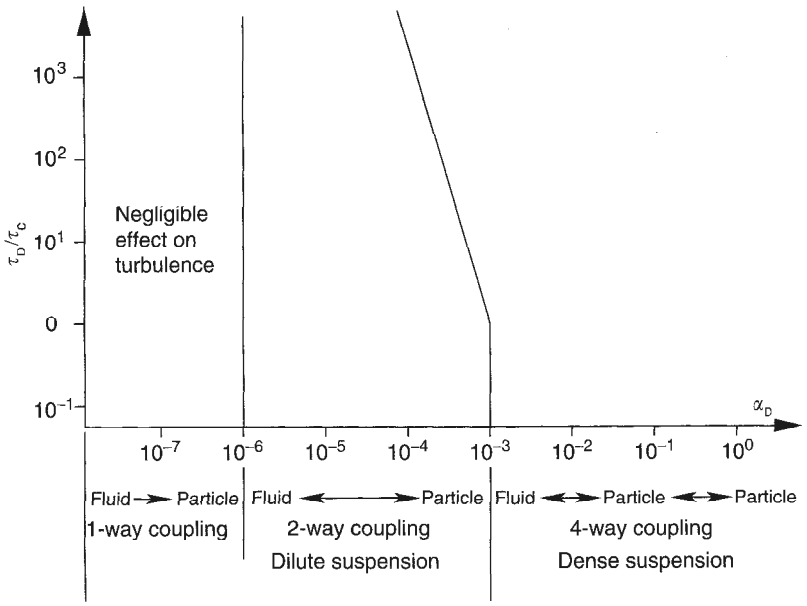

Figure 3.8: Degree of phase coupling in reference to response time. The ratio of response time of the disperse phase τ_D and the characteristic time of the continuous phase τ_C characterise the flow. The volume fraction of the disperse phase α_D determines the degree of phase coupling [21].

The distribution of droplet diameters in natural precipitation is not uniform. It can be described by droplet spectra. Calculating the motion for every single droplet diameter occurring in a given precipitation is computationally expensive. But for transmission line icing it is possible to deduce the behaviour of the whole spectrum from the motion of a droplet of medium volume diameter with sufficient accuracy [32]. The definition of the medium volume diameter assumes spherical drops, which is not accurate for larger rain drops. For theses the MVD determines an equivalent diameter. However, this inaccuracy is excusable, since the drag forces are determined by experiments and thus the mechanical effect due to deformed drops is accounted for.

3.3.3 Discussion of the Multiphase Flow Model

A Lagrangian trajectory approach is used to compute the particle motion for a stationary flow field, which is recommended for stationary dilute multiphase flows [21]. Presuming a low particle concentration in the flow, decoupling of the flow and the trajectory calculation and neglecting any effect of the particles on the air flow is justified [21]. Hence, the mixed stream of air and precipitation is modelled as one-way coupled multiphase flow. Figure 3.8 displays the feasible degree of phase coupling in a flow with reference to the volume fraction of particles in the flow and the characteristic time of disperse and continuous phase. The volume fraction

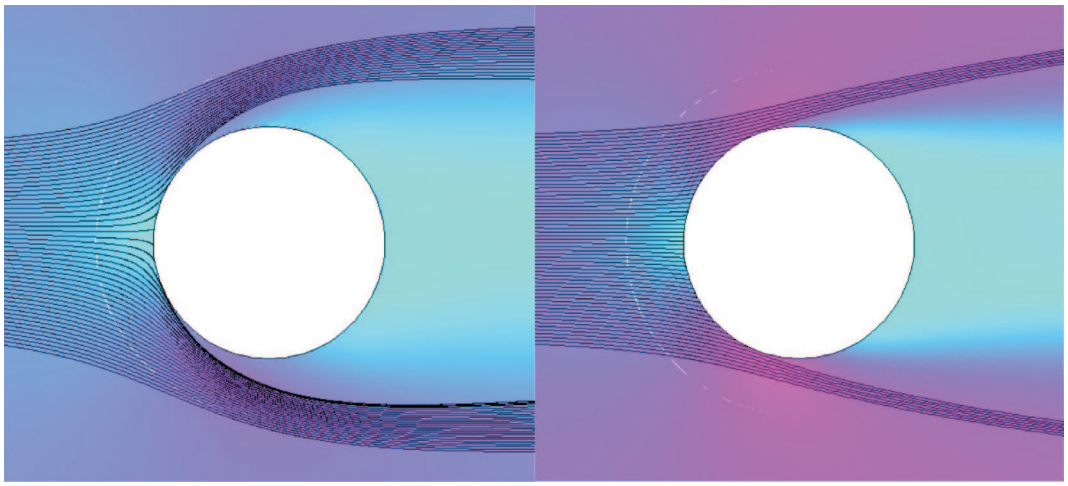

Figure 3.9: Testing particle trajectories at varying flow conditions. Here trajectories of droplets with a medium volume diameter $\mathrm{MVD} = 34\,\mu\mathrm{m}$ around a cable with a diameter $\mathrm{d} = 35\,\mathrm{mm}$ at two different wind velocities $\mathrm{u} = 0.5\,\mathrm{m/s}$ (left) and $\mathrm{u} = 5\,\mathrm{m/s}$ (right).

of natural precipitation is in the magnitude of 10^{-6}. Hence, it is possible to model natural precipitation one- or two-way coupling coupled phase flow.

Mass coupling due to evaporation or condensation of droplets is neglected, because of the low volume fraction of the disperse phase. Momentum coupling is accounted for by drag, buoyancy and gravity forces acting on the particles. Due to the one-way coupling is a vice versa effect of particles on the airflow is not considered. Coupling of heat energy is neglected, because precipitation and air are assumed to experience a negligible heat transfer in the model domain, which is very small compared to the spatial origin of precipitation. Also coupling of turbulent kinetic energy is not considered, because of the small volume fraction of particles. It would require a turbulence model allowing for the influence of particles on the turbulence formation. However, the implementation of such a model is left for further research.

Assuming the particles to be spherical is suitable, since at low particle Reynolds numbers the surface tension is high enough to sustain the spherical shape of a drop. It deforms when the Reynolds number increases. Significant deformations occur in general for $Re_p > 600$ [18]. Furthermore, the fluid forces acting on the particles are derived from experiments evaluated with reference to the particle Reynolds numbers using a droplet diameter and respectively an equivalent diameter for deformed particles [66]. Hence, deformation of droplets is accounted for. As an example, a rain drop with a diameter of 1 mm, falling with $6\,\mathrm{m/s}$ in calm wind conditions remains spherical, because it has $Re_p = 424$.

Another issue is to conclude from the behaviour of a particle of the medium volume diameter on the behaviour of the whole spectrum. Finstad et al. showed that this is the best approximation for modelling ice accretion on transmission lines by [32].

The trajectories are computed by a pair of four and five order Runge-Kutta algorithms, as described in section 3.6.2. An error can either arise from inadequate chosen solver parameters or from the implementation in the software package. The former is simply tested by examining the trajectories for various conditions that can occur during a simulation. If the trajectories are continuous for different particle diameters and wind velocities, the parameters are sensitive enough. Figure 3.9 shows two examples of such a computation, whereas continuity of the bending trajectories is examined at a high resolution. The latter is not investigated here, since there is no benchmark test available to verify the software.

3.4 Heat Transfer Model

3.4.1 Fundamentals of Heat Transfer

Heat transfer originates from three different transport mechanisms, namely conduction, convection and radiation heat transfer. Heat conduction is the transfer of thermal energy among neighbouring molecules due to a temperature gradient. The transport is directed from an area of higher temperature to an area of lower temperature and continues as long as the temperature difference is not equalized. It takes place in solids as well as gaseous or liquid fluids. In solids it appears as vibration of molecules in their lattice structure and as energy transport by free electrons. In fluids the energy is transferred by random Brownian motion. Heat transfer by large scale displacement of a fluid is termed convective heat transfer. At the interface of a solid body and a fluid a boundary layer forms. Due to friction the flow velocity decreases towards the surface. A heated surface conducts heat into the boundary layer. Fluid particles absorbing some of this heat energy are dragged off by the stream. Consequently, heat is transferred from the surface through the boundary layer into the fluid. In reference to the flow pattern two types of convection are distinguished: natural and forced convection. In case of natural convection the fluid motion is driven by density differences in the fluid due to the temperature gradient. Forced convection means that the fluid motion is driven by an external force. Heat radiation is a type of electromagnetic waves radiated from material. The intensity depends on the temperature of the body. It travels through a medium and is either absorbed or reflected by solid surfaces or trails off into the ambient space.

Dimensionless Quantities for Heat Transfer

In the following some dimensionless quantities are presented that are used to characterise heat transfer in fluids.

Prandtl number:
The Prandtl number describes the extension of the thermal boundary layer. It depends on

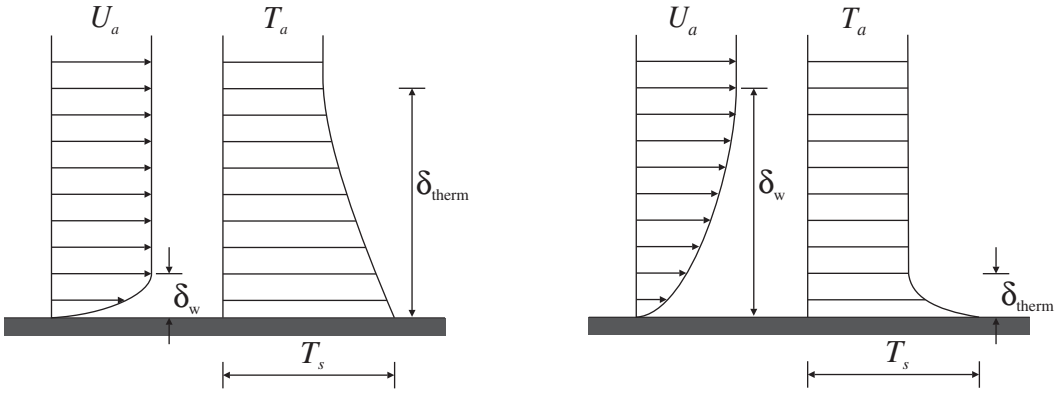

Pr<<1 (liquid metals) Pr>>1 (liquids, oils)

Figure 3.10: Boundary layer profiles with reference to the Prandtl number. U_a is the ambient velocity, δ_w the thickness of the velocity boundary layer, T_a the ambient temperature, T_s the surface temperature and δ_{therm} the thickness of the thermal boundary layer.

material properties of the fluid and is derived from the momentum and heat transport properties of a fluid. The ratio of kinematic viscosity and the thermal diffusivity defines the ration of momentum and thermal boundary layer thickness. Rearranging the ration leads of kinematic viscosity and the thermal diffusivity leads to:

$$Pr = \frac{\mu \cdot c_p}{k_f} \tag{3.39}$$

where c_p is the specific heat capacity at constant pressure, μ the dynamic viscosity and k_f the thermal conductivity of the fluid. For a large Prandtl number the thermal boundary layer is very small compared to the velocity boundary layer and vice versa as shown in figure 3.10.

Turbulences in the flow affect the momentum transport as well as the thermal diffusivity. This phenomenon is described by the ration of eddy diffusivity of momentum ε_M to eddy diffusivity of heat ε_H, the so-called turbulent Prandtl number:

$$Pr_T = \frac{\varepsilon_\mathrm{M}}{\varepsilon_\mathrm{H}} \tag{3.40}$$

It is not based on material properties, but depends on flow characteristics.

Grashof number:
The Grashof number characterises flows driven by natural convection. It is the ratio of buoyancy forces to viscous forces acting on the fluid. It is defined as:

$$Gr = \frac{g \cdot \rho \cdot \beta_{Gr} \cdot (T_s - T_a) \cdot l^3}{\mu^2} \tag{3.41}$$

where g is the gravity, T_s surface temperature, T_a ambient temperature and l characteristic length scale. Considering an ideal gas the fluid expansion coefficient is given by:

$$\beta_{Gr} = \frac{1}{T_a} \tag{3.42}$$

Nusselt number:
The Nusselt number is commonly used to describe the heat transfer properties of a fluid. It is defined as the ratio of convective to conductive heat transfer normal to a surface:

$$Nu = \frac{h \cdot l}{k_f} \tag{3.43}$$

where h is the heat transfer coefficient.

The Heat Equation

The first law of thermodynamics gives the fundamental law of heat transfer. It states the conservation of energy in a closed thermodynamic system. It is convenient to express the energy balance in terms of temperature, since it states the temperature distribution in the system:

$$\rho c_p \frac{\partial T}{\partial t} + \nabla \cdot \left(-k_f \cdot \nabla T\right) = Q - \rho c_p \mathbf{u} \cdot \nabla T \tag{3.44}$$

where Q is a heat source or sink and $\mathbf{u}$ the velocity vector. The first term on the left hand side of equation 3.44 accounts for temperature changes over time and disappears in a steady-state analysis. The second term on the left represents conductive heat transfer. On the right hand side, the first term is a heat source or sink. The other term accounts for convective heat transfer due to fluid motion. Heat dissipation due to viscous effects and pressure work are not considered. The flow is presumed to be incompressible and the air is considered as ideal gas. Thus, pressure, temperature and density are related by the following state equation for ideal gases:

$$\rho = \frac{p}{R \cdot T} \tag{3.45}$$

where p is the pressure and R is the universal gas constant. The ideal gas law presumes randomly moving, non-interacting gas particles with no spatial dimension.

Conductive Heat Transfer

Conductive heat transfer is caused by a temperature gradient. The diffusion due to a potential gradient can be described by a simple relationship. In case of a temperature gradient it is

described by Fourier's law:

$$\mathbf{q}_d = -k_f \cdot \nabla T \tag{3.46}$$

The thermal conductivity in solids can be non-isotropic. In such a case the conductivity is expressed by a tensor.

Convective Heat Transfer

Convective heat transfer describes the transport of thermal energy due to fluid motion. It is defined by:

$$\mathbf{q}_c = \rho \cdot c_p \cdot \mathbf{u} \cdot T \tag{3.47}$$

The heat transfer from a solid body into a fluid can follow two different mechanisms, namely natural and force convection. The first is driven by density differences in the fluid due to temperature gradient. In case of forced convection, the motion of the flow is primarily caused by external forces and not only by a density gradient. Both cases require consideration of the thermal boundary layer forming at the surface in order to determine the convective heat transfer.

In order to avoid modelling of the boundary layer itself it is possible to use experimentally or theoretically determined heat transfer coefficients to determine the heat transfer. It is a very efficient and accurate method for most engineering applications. A large number of empirical and theoretical correlations are available for a variety of different settings. This however, requires appropriate conditions like geometry and flow pattern. Thus, it is not possible to conclude from a certain heat coefficient to an arbitrary setting. The approach is efficient, because it avoids complex modelling of the heat transfer in the boundary layer. It is not even necessary to compute the whole flow field. For predefined settings it is sufficient to know free stream velocity, fluid properties and characteristic length of the flow geometry to define a heat transfer coefficient as it is shown in appendix B.

The following equation allows us to compute the heat transfer between a surface and a fluid using heat transfer coefficient h:

$$q_c = h \cdot (T_s - T_a) \tag{3.48}$$

For a given setting the heat transfer coefficient is defined by the dimensionless Nusselts and Grashof numbers.

Another approach is numerical modelling of the boundary layer. It requires demanding computations, because it requires a flow calculation that resolves the thermal boundary layer at the surface. The benefit of such a demanding calculation is that it allows for thermal interaction among individual bodies in the flow and for settings that are not defined by heat transfer

coefficients given in the literature. In our case of conductor bundles, the air heats up when the flow passes an energised conductor. Hence, the conditions vary between up- and downstream conductors in a bundle. Consequently, the model requires a simulation of the thermal boundary layer and the convective heat transfer in the flow. As aforementioned the velocity field and temperature distribution are independently determined.

The chosen approach to model the thermal boundary layer is similar to the concept of eddy diffusivity and wall functions used in the fluid dynamics model (cf. section 3.2). It describes the thermal boundary layer using a thermal wall function. Their influence is included in the dimensionless temperature T^+, which also depends on a computation of the velocity boundary layer. The convective heat transfer at a surface is then described by:

$$q_c = \frac{\rho \cdot c_p \cdot C_\mu^{1/4} \cdot k_w^{1/2}}{T^+} \cdot (T_s - T) \tag{3.49}$$

where T^+ is the dimensionless temperature, k_w the turbulent kinetic energy at the wall, $C_\mu = 0.09$ a model constant, T the local fluid temperature. The dimensionless temperature is given by the following relation [64]:

$$T^+ = \begin{cases} Pr \cdot y^+ & for \quad y^+ < y_1^+ \\ 15\,\mathrm{Pr}^{2/3} - \frac{500}{(y^+)^2} & for \quad y_1^+ \leq y^+ < y_2^+ \\ \frac{\mathrm{Pr}}{\kappa}\ln(y^+) + 15\,\mathrm{Pr}^{2/3} - \frac{\mathrm{Pr}_T}{2\kappa}\left(1 + \ln\left(\frac{\kappa \cdot 10^3}{\mathrm{Pr}_T}\right)\right) & for \quad y_2^+ \leq y^+ \end{cases} \tag{3.50}$$

with:

$$y^+ = \frac{\delta_w \cdot \rho \cdot C_\mu^{1/4} \cdot k^{1/2}}{\mu}$$

$$y_1^+ = \frac{10}{\mathrm{Pr}^{1/3}} \tag{3.51}$$

$$y_2^+ = 10 \cdot \sqrt{10 \frac{\kappa}{\mathrm{Pr}_T}}$$

with the Turbulent Prandtl number as proposed by Kays and Crawford [54]:

$$Pr_T = \left(\frac{1}{2\,\mathrm{Pr}_{T\infty}} + \frac{0.3}{\sqrt{\mathrm{Pr}_{T\infty}}} \cdot \frac{c_p \mu_T}{k} - \left(\frac{c_p \mu_T}{k}\right)^2 \cdot \left(1 - e^{-k \Big/ \left(0.3 C_p \mu_T \sqrt{\mathrm{Pr}_{T\infty}}\right)}\right)\right)^{-1} \tag{3.52}$$

where $Pr_{T\infty} = 0.85$ is a model constant. A flow is primarily driven by forced convection for $Gr/Re^2 << 1$ [131]. This is the case for the conditions of atmospheric icing considered here and therefore only forced convection is modelled.

Radiative Heat Transfer

Thermal radiation is heat transfer via electromagnetic waves. In general it is considered as a boundary condition between solid bodies and fluids. Radiation is regarded as emitted, absorbed and reflected at a surface or that it trails off into the ambient space. Solid bodies are either treated as transparent or opaque regarding thermal radiation. The latter means that no radiation is transmitted through the body, which is true for most solid objects. Radiative heat transfer of an opaque body includes the total incoming radiative flux G and the total outgoing radiative flux J, which is the sum of reflected and emitted radiation:

$$J = \rho_r \cdot G + \varepsilon_r \cdot \sigma \cdot T^4 \tag{3.53}$$

where σ is the Stefan-Boltzmann constant, ρ_r the reflectivity and ε_r the surface emissivity. The net outward radiative flux is then given by:

$$q_r = J - G \tag{3.54}$$

Merging equation 3.53 and 3.54 leads to a general expression for radiation heat flux at the surface of an opaque body.

$$q_r = \left(\varepsilon_r \cdot \sigma \cdot T^4 - (1 - \rho_r)\right) \cdot G \tag{3.55}$$

Most opaque bodies behave like an ideal grey body that absorb as much radiation as it emits. This assumption leads to:

$$\varepsilon_r = 1 - \rho_r \tag{3.56}$$

Consequently, the net inward radiative heat flux of an ideal grey body is given by:

$$q_r = \varepsilon_r \cdot \left(\sigma \cdot T_s^4 - G\right) \tag{3.57}$$

There are two different cases to consider, radiation between solid body and ambient space and between two solid bodies. They differ in the definition of the irradiation term G. Ambiance is treated like a black body of constant temperature with a perfect emissivity and absorptivity, but no reflectivity. Radiation from surface to surface is more complex, because it includes mutual irradiation from different surfaces. Furthermore, radiation of the ambient space depends on spatial arrangement of the bodies, which requires a view factor to appropriately describe the fraction of ambient emissivity and absorptivity along the boundary. Only the first case is included in the model. Radiation between the conductors is negligibly small and therefore the model allows only for radiation from the conductor to the ambient space. Thus, the irradiation is described by:

$$G = \sigma \cdot T_a^4 \tag{3.58}$$

Incorporating this into equation 3.57 gives the net inward radiation heat flux for an ideal grey body as:

$$q_r = \varepsilon_r \cdot \sigma \cdot \left(T_s^4 - T_a^4\right) \tag{3.59}$$

Boundary Conditions of the Heat Equation

The boundary conditions for the heat equation (cf. equation 3.44) are either defined as temperature or as heat flux. Thus, a temperature boundary condition is defined by:

$$T = T_0 \tag{3.60}$$

The heat flux boundary condition normal to the surface is given by:

$$q = q_d + q_c + q_r \tag{3.61}$$

Heating due to friction of the air on the surface, the so-called viscous heating is not considered, because it is negligibly small in case of atmospheric icing of structures. In contrary, aircraft icing models commonly allow for heating due to airflow, for example. The exterior boundaries of the model are either treated as insulated surface having a constant temperature or allowing for a convective heat flux over the boundary. The latter is a common outflow condition, where a fluid carries the heat energy out of the model domain.

3.4.2 Model Equations of the Heat Transfer

The model solves the heat equation decoupled from the fluid flow calculation, which means that the flow field is not affected by the temperature distribution. Material properties like density and viscosity are treated as constants. The temperature distribution is determined based on previously computed stationary flow field. Thus, the thermodynamic system is presumed to have enough time to find a steady state. In the following the equations are presented that are used to determine the temperature distribution in the model.

Heat Transfer in the Fluid Domain

Transforming the heat equation into a Reynolds Average Navier-Stokes (RANS) model leads to the following form of a time-averaged equation that describes the conservation of energy:

$$\rho \cdot c_p \mathbf{U} \cdot \nabla T = \nabla \cdot \left(\left(k_f + k_T \right) \nabla T \right) \tag{3.62}$$

where $\mathbf{U}$ is the time-averaged velocity vector and k_T the eddy conductivity, which is given by:

$$k_T = \frac{c_p \cdot \mu_T}{Pr_T} \tag{3.63}$$

where Pr_T is the turbulent Prandtl number (cf. section 3.4.1) and μ_T the turbulent viscosity (cf. section 3.2.2). The left hand side of equation 3.62 represents convective and the right hand side conductive heat transport.

External Boundary Condition of the Fluid Domain

The external model boundaries of the fluid domain are the inlet and outlet of the flow and two limiting boundaries at the top and the bottom of the domain (cf. figure 3.2). The inlet boundary as well as the upper and lower boundary have a predefined ambient temperature as boundary condition.

$$T = T_a \tag{3.64}$$

The boundary condition at the outlet allows for convective heat flux:

$$\mathbf{q} = \rho \cdot c_p \cdot \mathbf{u} \cdot T \tag{3.65}$$

Hence, the heat carried by the airflow leaves the model domain via the outlet boundary.

Heat Transfer in the Conductor and Ice Deposit

The heat transfer in a conductor and an ice deposit is governed by conduction and therefore determined by:

$$\nabla \cdot (-k \cdot \nabla T) = Q_i \tag{3.66}$$

where Q_i is a heat source, which is in our case an energised conductor. It originates from Joule heating and is defined by:

$$Q_i = I^2 \cdot R_c \tag{3.67}$$

where I is the electrical current and R_c the electrical resistance of the conductor.

Heat Transfer at the Freezing Interface

The heat transfer at the freezing interface defines the icing condition. It determines whether impinging precipitation freezes or not and under which growth mechanism the ice forms. Freezing can occur at the interfaces between air, conductor and ice deposit. The heat transfer at the interface is given by:

$$q_f = q_c + q_{e,s} + q_l + q_r - q_i \tag{3.68}$$

where q_f is the heat flux due to latent heat of freezing precipitation. On the right hand side q_c is the convective heat loss, $q_{e,s}$ the heat transfer due to sublimation or evaporation, q_l the heat loss due to warming supercooled droplets to freezing temperature, q_r the radiative heat flux and q_i warming of the surface due to Joule heating of a conductor. The equations for the

individual heat fluxes are as follows.

Latent heat of freezing:

$$q_f = (1-\lambda)\cdot\alpha\cdot\beta\cdot\chi\cdot F_p\cdot L_f \tag{3.69}$$

where λ is the fraction of unfrozen water within the ice. A theoretical study [78] and experimental investigations [39] show that λ is relatively independent from growing conditions and that $\lambda = 0.3$ is a reasonable approximation. The local mass flux of particles that freezes at the surface is given by $\alpha\cdot\beta\cdot\chi\cdot F_p$ (cf. section 2.3) and L_f is the latent heat of freezing.

Convective heat transfer:

$$q_c = \frac{\rho\cdot c_p\cdot C_\mu^{1/4}\cdot k_w^{1/2}}{T^+}\cdot(T_s - T)$$

which is equation 3.49 already defined in section 3.4.1.

Evaporation and sublimation heat flux:

$$q_{e,s} = \frac{\rho\cdot c_p\cdot C_\mu^{1/4}\cdot k_w^{1/2}}{T^+}\cdot\varepsilon_m\cdot L_{e,s}\cdot\frac{e(T_a) - e(0\,^\circ\mathrm{C})}{c_p\cdot p} \tag{3.70}$$

where ε_m is the ratio of molar masses of water and air, $L_{e,s}$ the latent heat of evaporation or sublimation, $e(T_a)$ the vapour pressure of the ambient air and $e(0\,^\circ\mathrm{C})$ the saturated water vapour pressure at $0\,^\circ\mathrm{C}$.

Heat flux due to warming supercooled droplets to freezing temperature:

$$q_l = \alpha\cdot\beta\cdot F_p\cdot c_p\cdot(T_s - T_p) \tag{3.71}$$

where $\alpha\cdot\beta\cdot F_p$ is the local mass flux, c_p is the specific heat capacity of water at constant pressure and T_p the droplet temperature.

Radiation heat flux:

$$q_r = q_{r,s} + q_{r,l} \tag{3.72}$$

where $q_{r,s}$ is short wave radiation and $q_{r,l}$ is long wave radiation. Short wave radiation represents heat radiation and is given by:

$$q_{r,s} = \sigma\cdot\varepsilon_r\cdot\left(T_s^4 - T_a^4\right) \tag{3.73}$$

The solar radiation $q_{r,l}$ is required as input from meteorological data or estimated by equations as presented in [46], for example. In general, it is neglected during an icing event, since the sky is covered with clouds and solar radiation is negligible [82].

Heat flux due to Joule heating of an energised conductor:

$$q_i = \frac{Q_i}{\pi \cdot d_c} \tag{3.74}$$

where d_c is the conductor diameter. Ice accretion models for aircraft sometimes consider also kinetic heat of impinging droplets and viscous heating due to friction of the airflow, for example. However, both are negligibly small, because the flow velocities are significantly smaller.

Supercooled Liquid Water Film

Under wet icing conditions a supercooled liquid water film forms on ice surfaces. This process is closely linked to the heat balance at the freezing interface. Several modelling approaches have been published on this issue (cf. section 2.3), but none of them seemed to adequately predict the behaviour of such a film. Developing a new approach exceeds the given resources. Hence, the model allows only for dry growth even when the temperature distribution would indicate wet growing conditions. Obviously, this is a significant but commonly made simplification. However, in the following some simulation schemes are presented in order to give an impression in which direction further research should go. A very promising approach is a morphogenetic model [146, 147]. It determines the local freezing of water film by a random variable derived from the global accretion efficiency of the body being iced. Hence, the local ice accretion is considered as stochastic process that satisfies the global icing conditions. Thus, the model predicts differently shaped ice deposits even under identical boundary conditions, which reproduces characteristics observed in experiments. Another more common approach is the treatment of the liquid water film as a continuous thin layer. The film flows between a fixed and a moving plate, where the motion of the plate resembles shear stresses of the airflow and gravity acting on the water. This approach includes simplifications such as assuming a continuous water film and neglecting shedding of the water film. It seems to be an useful approach, but it shows limitations when compared with experimental results [35]. However, an adequate simulation of the water film seems to require three-dimensional modelling of rivulets that form on the surface and solidification of single droplets. Such complex models are computationally expensive and not applicable for the model here presented [99, 100, 174].

Figure 3.11 displays a comparison of complex aircraft icing models that include a simulation of a liquid water film. It demonstrates how difficult it is to simulate the behaviour of a supercooled water film on an ice surface. Therefore, the model does not allow for the formation of a liquid layer. An adequate approach for transmission line icing models is left for further research.

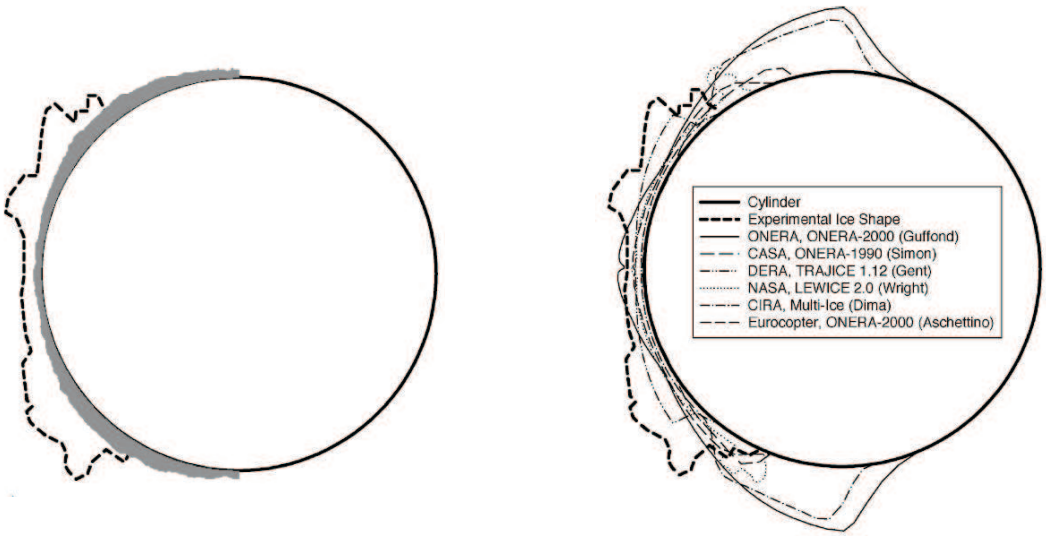

Figure 3.11: An ice accretion experiment is compared with a morphogenetic model (left) and aircraft icing models (right) [147]. It clearly shows the influence of individual liquid layer modelling on the ice accumulation. The experiments and the model runs were based on a temperature of $T_a = -2.95\,°C$, airspeed of $u = 77.2\,m/s$, a liquid water content of $LWC = 0.44\,g/m^3$, an icing duration of $5.5\,min$ and a medium volume diameter of $MVD = 18\,\mu m$ and a cylinder diameter of $6.35\,cm$.

3.4.3 Discussion of the Heat Transfer Model

The heat balance is determined by a stationary calculation for two reasons. Firstly, the temperature distribution is determined based on a given flow field, which is modelled as being stationary. The second reason is that the effort would not correspond to the other model elements and the additional information would not give any additional benefit. The formulation of the heat balance at the freezing interface is developed in agreement with other models and already presented in [160]. A difference among icing models is the treatment of Joule heating. It is either defined as boundary condition at the conductor surface or heat conduction within the cable and ice deposit is modelled. Examining the latter approach revealed very small temperature variations along the conductor surface as shown in figure 3.12, for example. Thus, it is sufficient to introduce a uniform conductor surface temperature in the icing model. Consequently, the heat balance at the conductor surface requires only a single computation for given icing conditions. The computation of the heat transfer at the surfaces requires either relative heat transfer coefficients or modelling the thermal boundary layer. The first is not possible, because there are no coefficients for iced conductors available. Furthermore, such an approach does not allow for investigating possible interaction of heated conducts in a bundle. Therefore, the temperature distribution in the flow is computed including thermal boundary layers forming on the conductor surfaces. One can argue that the applied eddy diffusivity model is not very accurate compared to advanced thermodynamic models. However, for a case such

as our conductor icing model with a two dimensional flow computation and a boundary layer described by a wall function it is a reasonable approach [53]. The formation of a supercooled water film in wet icing conditions is neglected, because an adequate modelling approach is not available. Developing such a simulation scheme is left for further research. Fu et al. investigated temperature distributions of energised conductors with ice deposits [36]. They too found only small temperature variations on the conductor surface, which supports the decision to assume a uniform temperature at the conductor surface. Moreover, their results indicate that the fundamental experiments on heat transfer coefficients of an aluminium cylinder by Achenbach [1] should only be used as rough estimate for heat transfer of energised conductors. Due to individual surface structure (torsional strands) and heat conductivity of the cables the heat conductivity significantly differs from that of a solid aluminium cylinder. Therefore, a detailed analysis of heat transfer of energised conductors and ice deposits should determine key parameters such as conductivity and heat transfer coefficients specifically for each icing conduction. Numerical simulation of the heat transfer does not lead to more precise results.

In order to validate the numerical model we compare the power generated by the energised conductor with the power taken by the flow passing the conductor. A measure to quantify the possible amount of heat energy transported in a flow is the heat capacity flux. It is given by:

$$\dot{W} = A \cdot u \cdot \rho \cdot c_p \tag{3.75}$$

where A is a reference area the flow passes. Multiplying the heat capacity flux with an increase in temperature over a certain distance gives the power taken by the flow.

Figure 3.12 shows a simulation of the temperature distribution in an energised conductor and the surrounding airflow. Considering a 1 m long section of the conductor, a flow velocity of $\mathrm{u} = 5\,\mathrm{m/s}$ and an in- and outflow reference area of 0.1 m high, then the heat capacity flux is determined to:

$$\dot{W} = 0.1 \cdot 1 \cdot 5 \cdot 1.29 \cdot 1006 = 648.9 \left[\frac{\mathrm{J}}{\mathrm{s} \cdot \mathrm{K}}\right] \tag{3.76}$$

The numerically computed temperature increase at the outflow is:

$$\Delta T = 0.071\ [\mathrm{K}] \tag{3.77}$$

Implying that heat loss through the other boundaries is neglected, the power taken by the flow is:

$$P_f = \Delta T \cdot \dot{W} = 46.1 \left[\frac{\mathrm{J}}{\mathrm{s}}\right] \tag{3.78}$$

The power generated in the energised conductor is calculated by:

$$P_c = I^2 \cdot R_c \tag{3.79}$$

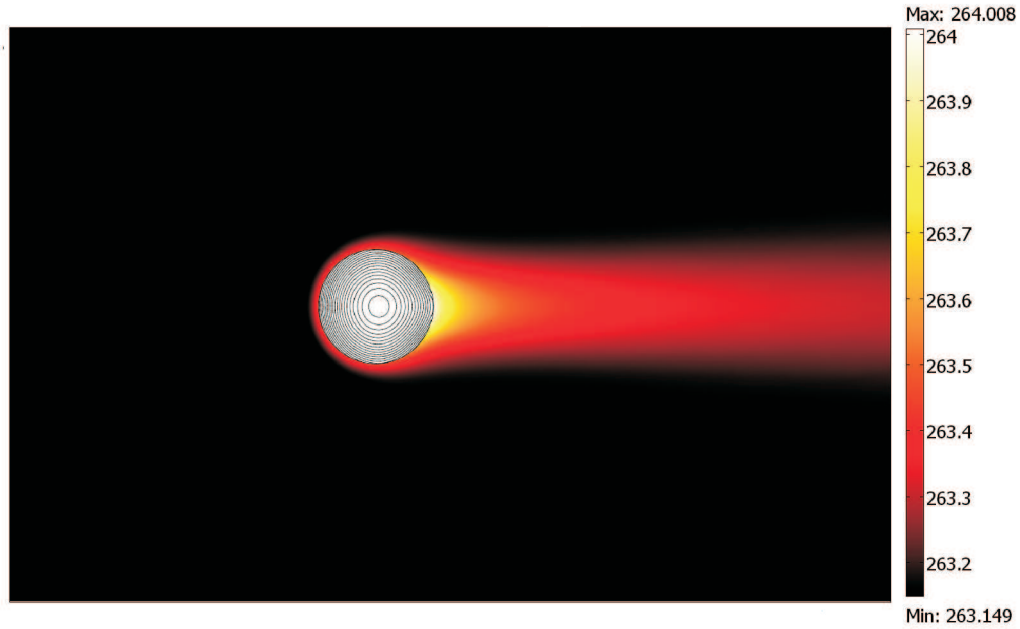

Figure 3.12: Temperature distribution of an energised conductor and a surrounding airflow. An additional contour plot is used to illustrate minimal variances in temperature distribution in the conductor. The model parameters are a flow velocity $u = 5m/s$, an ambient temperature $T_a = -10°C$ or $T_a = 263.15K$ respectively and a power generated by the conductor of $46.2J/s$.

The numerical model proves to be correct, when the calculated temperature increase in the fluid is in equilibrium with the power generated in the conductor. For the given case, the power generated in the conductor is:

$$P_c = 46.2 \left[\frac{\mathrm{J}}{\mathrm{s}}\right] \tag{3.80}$$

The difference between generated energy and energy taken up by the flow is satisfactorily small with $\Delta P_f = 0.1\,\mathrm{J/s}$.

Subsequently, the total heat flux at the cylinder surface is computed analytically and compared with the numerical result. The analytical calculation uses a heat transfer coefficient for a cylinder with the same flow conditions of the previous example. More details on the analytical calculation is given in appendix B. It results in a total heat flux of:

$$q = h \cdot (T_s - T_a) = 54.85 \cdot 0.52 = 28.52 \left[\frac{\mathrm{W}}{\mathrm{m}^2}\right] \tag{3.81}$$

The numerical model computes a heat flux of a 1 m long section of the conductor to:

$$q = 28.72 \left[\frac{\mathrm{W}}{\mathrm{m}^2}\right] \tag{3.82}$$

Thus, the deviation of both calculations is only $\Delta q = 0.2\,\mathrm{W/m^2}$, which is a satisfying result.

3.5 Ice Growth Model

3.5.1 Fundamentals of Ice Accretion

The mechanism of ice accretion is already described in detail in chapter 2. Therefore, only a brief overview of atmospheric icing is given here. The stream of precipitation particles and the heat flux at the surface govern the icing process. The first affects shape and to a smaller extent also density of ice deposits. The latter defines the icing condition, which influences the accretion mass and furthermore the evolving ice density. Rime, glaze ice and wet snow are the major types of deposit leading to significant loads on structures. Rime ice develops in dry growing conditions, where the latent heat released during freezing is dissipated without causing a change in the state of the ice and hence no liquid water occurs. Contrarily, a liquid water layer forms during the icing process in so-called wet ice growth. The heat balance on the ice surface is in a sensitive equilibrium between freezing and melting of the ice. More details on modelling ice accretion are given in [117] and further aspects of icing of power networks can be found in [29].

3.5.2 Model Equations of the Ice Growth Model

The ice growth model is the core of the ice accretion model. At the end of every simulation step it computes shape and density. The model follows the structure of icing models as described in section 3.1.The computation of the local ice growth includes four parameters based on the previously described models. Collision and collection efficiency result from the multiphase flow model presented in section 3.3.The accretion efficiency depends on the heat balance, which is computed by the heat transfer model as described in section 3.4. Finally, the accretion rate, which is calculated by the ice growth model itself. The computation of these parameters is derived in the following sections.

Collision Efficiency

The local collision efficiency is the ratio of droplet mass flux in the undisturbed incoming flow to the mass flux of droplets impinging on the surface. It is defined by:

$$\alpha = \frac{A_0}{A_i} \tag{3.83}$$

where A_0 is the initial trajectory spacing in the undisturbed flow and A_i is the corresponding spacing of the impinging locations on the surface. Thus, the ratio is governed by air flow, particle drag and inertia. Particles with a large inertia lead to a collision efficiency tending towards one. Smaller inertia results in lower collision efficiency. Consequently, the icing rate

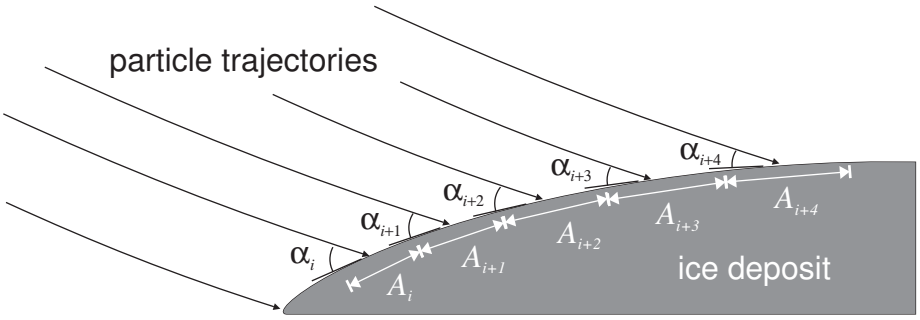

Figure 3.13: Local collection efficiency based on the trajectory approach.

decreases when particles are dragged around the object by the air flow. The large droplets of freezing rain have a local collision efficiency of approximately one, for example. In general, cloud droplets and snow flakes have a collision efficiency varying between zero and one.

Collection Efficiency

The collection efficiency accounts for those particles that impinge on the surface and stick to it. Particles which do not stick bounce from the object being iced. Sticking particles contribute directly or indirectly to the ice formation. Directly means that particles contribute to the heat balance and eventually freeze. Particles that do not freeze are only part of the heat balance and only indirectly affect the ice evolution. Thus, the collection efficiency is one, when all particles stick to the surface and freeze. The collection efficiency depends on the precipitation properties. Therefore, different approaches are used for the individual precipitation types. The collection efficiency of rime ice accretion in case of in-cloud icing is considered to be [117]:

$$\beta = 1 \tag{3.84}$$

In case of freezing rain the collection efficiency is calculated by [117]:

$$\beta = \cos(\alpha_i) \tag{3.85}$$

where α_i is the impact angle of the droplets. It accounts for splashing of droplets when they impinge on the surface at a small angle. Up to now, there is no reliable theory available to estimate the collection efficiency of wet snow. The best approximation is based on experiments by Admirate et al. [3]:

$$\beta = \begin{cases} \dfrac{1}{u_i} & for \quad 1 \leq u_i < 10 \\ 1 & for \quad 0 \leq u_i < 1 \end{cases} \tag{3.86}$$

where u_i is the impact velocity of snow flakes.

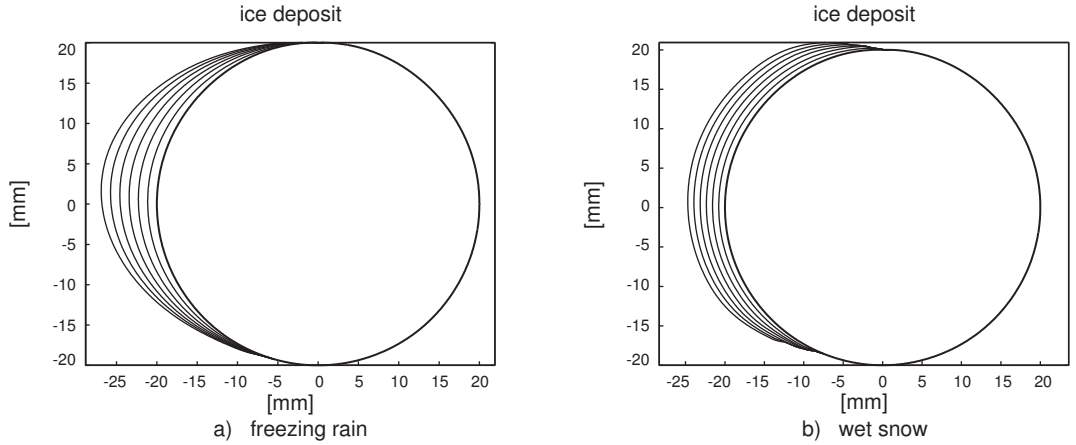

Figure 3.14: The deposit due to freezing rain formed at a wind velocity $u = 15\,\mathrm{m/s}$, particle diameter $MVD = 120\,\mu\mathrm{m}$, an ambient temperature $T_a = -5\,^{\circ}\mathrm{C}$, liquid water content in the air $LWC = 1.0\,\mathrm{g/m^3}$. Wet snow is simulated with a wind velocity $u = 5\,\mathrm{m/s}$, particle diameter $MVD = 150\,\mu\mathrm{m}$, an ambient temperature $T_a = -3\,^{\circ}\mathrm{C}$ and liquid water content in the air $LWC = 1.5\,\mathrm{g/m^3}$.

Rime ice deposits generally have a streamlined shape, whether they are caused by cloud droplets or freezing rain. However, the mechanism leading to such a shape is different for both precipitation types. In-cloud icing is characterised by a collision efficiency decreasing towards the edges of a cable being iced, because cloud droplets are dragged around edges by an air stream due to a low inertia. The collection efficiency of freezing rain decreases towards the edges, because the impinging angle decreases.

Accretion Efficiency

The accretion efficiency accounts for particles that impinge and stick to the surface and freeze eventually. It equals one, when all particles freeze. If the heat flux is too small, not all particles solidify. The unfrozen water forms a liquid film on the surface. During the icing process, the surplus of water either is enclosed in the ice deposit or leaves the surface due to wind drag and gravity. In case of rime ice accretion all impinging particles freeze instantly and no liquid water is enclosed in the ice body. The accretion efficiency for rime ice is given by:

$$\chi = 1 \tag{3.87}$$

Under wet ice growing conditions the heat balance determines the accretion efficiency, which therefore depends on the local heat fluxes and is defined by:

$$\chi = \frac{q_c + q_{e,s} + q_l + q_r - q_i}{(1-\lambda)\cdot\alpha\cdot\beta\cdot F_p\cdot L_f} \tag{3.88}$$

where the nominator includes the convective heat loss q_c, the heat transfer due to sublimation or evaporation $q_{e,s}$, the heat loss due to warming supercooled droplets to freezing temperature

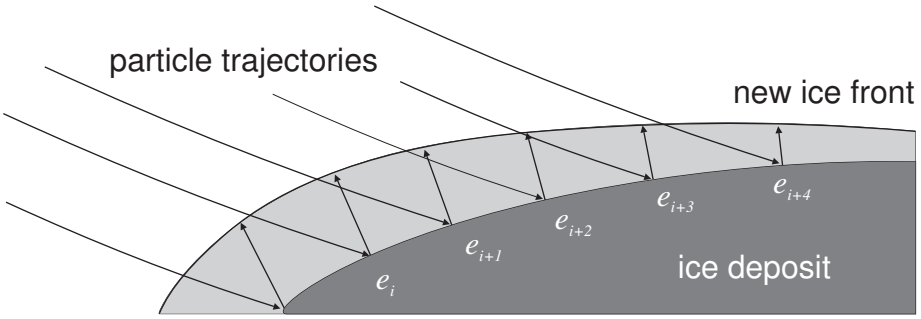

Figure 3.15: Growth of a new ice front along ice evolution vectors shifting the boundary normal to the surface.

q_l, radiative heat flux q_r and the surface warming due to Joule heating of the conductor q_i. The deviator includes the fraction of unfrozen water within the ice deposit λ, the local mass flux $\alpha \cdot \beta \cdot F_p$ and the latent heat of freezing L_f. A reasonable approximation for the fraction of unfrozen water is $\lambda = 0.3$. A theoretical study [78] and experimental investigations [39] show that λ is relatively independent from growing conditions.

Ice Accretion Ratio

The ice accretion ratio allows for the density of the precipitation fluxes and the evolving density of ice deposits. The ice density is determined by empirical equations. Following the investigation of Fu et al. [37], the equations derived by Bain and Gayet [4] are chosen here:

$$\begin{aligned} \rho_i &= 110 \cdot R^{0.76} && for && 0 < R \leq 10 \\ \rho_i &= \frac{R}{R+5.61} \cdot 10^3 && for && 10 < R \leq 60 \\ \rho_i &= 917 && for && 60 < R \end{aligned} \tag{3.89}$$

where R is the Macklin's Parameter given by [72]:

$$R = \frac{MVD \cdot u_i}{2 \cdot T_s} \tag{3.90}$$

with the medium volume diameter MVD, the impact speed u_i and the surface temperature T_s.

Similar to the collection efficiency also the density of wet snow deposits is not clearly defined. Laboratory tests are barely possible and therefore these investigations depend on field observations of wet snow events. Two different empirical equations are presented in the literature to estimate the density of wet snow deposits. One is derived from data measured in Japan [2]:

$$\rho_i = 300 + 20 \cdot u_i \qquad for \qquad u_i < 10 \tag{3.91}$$

while the other one is based on measurements in France [2]:

$$\rho_i = 200 + 20 \cdot u_i \qquad for \qquad u_i < 10 \tag{3.92}$$

Both give a similar estimate of the density. The reason for the differences is linked to the individual meteorological conditions of both observations. However, the measured data does not indicate which one is to be preferred under certain conditions. For example, one might expect deposits with higher densities, when the wind is stronger. The observation in France recorded higher wind velocities. However, for a given wind velocity, it predicts lower densities then the observation in Japan indicates. This might be linked to higher liquid water content in the snow flakes, which unfortunately is not measured. The empirical equations include significant uncertainties, especially when considering melting processes. Consequently, this has to be considered, when one of the relations is chosen for an investigation.

The ice accretion ratio is eventually derived from precipitation flux and evolving ice density time the duration of the simulation step:

$$\delta = \frac{LWC \cdot u_{p,0}}{\rho_i} \cdot t_{int} \tag{3.93}$$

where LWC is the liquid water content in the air, $u_{p,0}$ the particle velocity in the undisturbed flow and t_{int} the duration of a simulation step. Within one simulation step the flow field is unchanged.

Growth of the Ice Front

The growth of the ice front defines the new geometry of the ice deposit. It includes all aforementioned parameters and computes the new shape by shifting the ice front along a vector normal to the surface. The ice evolution vector is then expressed by:

$$\mathbf{e}_i = \alpha \cdot \beta \cdot \chi \cdot \delta \cdot \mathbf{n} \tag{3.94}$$

where $\mathbf{n}$ is the unit vector normal to the surface. A new simulation step starts on the basis of the new geometry of the ice deposit.

As an example, figure 3.14 displays simulations of ice deposits caused by freezing rain and wet snow. The effect of droplet splashing and sticking of wet snow on the conductor is clearly observable, when comparing figure 3.14a and 3.14b. The simulation of the wet snow deposit assumes the snow density to follow equation 3.92.

3.5.3 Discussion of the Ice Growth Model

In order to verify the model, two test cases where examined. The test cases consist of numerical and experimental investigations of rime ice accretion on a single conductor presented in [37].

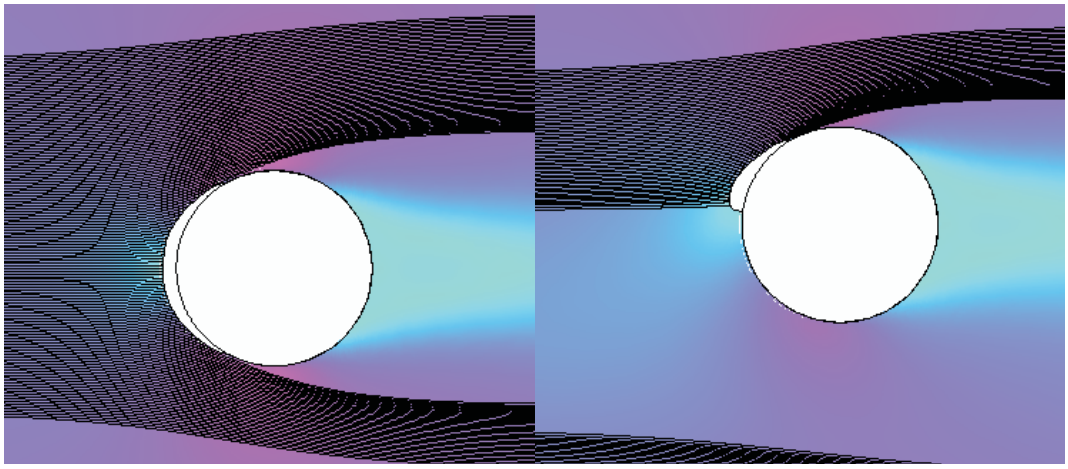

Figure 3.16: Particle trajectories around a conductor bundle with ice accretion. It shows the shielding effect of an upstream cable (left) on a downstream cable (right). The horizontal spacing between the conductors is $400\,\mathrm{mm}$ and torsional displacement of the bundle is $5.7°$. Simulation parameters are wind velocity $u = 5\,\mathrm{m/s}$, particle diameter $MVD = 28\,\mu\mathrm{m}$, ambient temperature $T_a = -15\,°\mathrm{C}$ and cable diameter $d = 40\,\mathrm{mm}$.

Experimental investigations of conductor icing are often not sufficiently documented to allow for comparison with numerical simulations, because essential information like droplet sizes or temperature are missing. Furthermore, experiments as well as simulations of glaze ice and wet snow accretion include significant uncertainties in treating the transition of ice and liquid water during the icing process. Therefore, adequate results for comparison are not available and only rime ice accretion is used as reference case.

An earlier investigation of the model already showed satisfying results [161], but it underestimated the mass accumulation at the edges of ice deposits. To overcome this problem, the resolution of the mass flux is increased, meaning that a larger number of particle trajectories with a smaller spacing is computed. Figure 3.17 shows experimentally and numerically determined ice shapes of the test cases in comparison with the model presented here. The longitudinal extension of the ice deposit computed by the model is in good agreement with experimental results. It meets the longitudinal extension of the ice body very well for both the larger and the smaller cable diameter. The vertical extension of the ice deposit at the smaller conductor deviates more than at the larger conductor. This is due to the resolution of particles impinging on the surface, which is defined by the initial particle trajectory spacing in the undisturbed flow. When using the same trajectory spacing for both conductors, the relative resolution of the larger cable is better. Meaning that relative to the curvature of the iced conductor more impinging locations of particles are computed for the larger than for the smaller conductor. Particles impinging furthest to the upper and lower edge are not necessarily as close to the edge as possible. Consequently, the surface area with no mass flux at the upper and lower edge is overestimated and less mass is caught at the upper and lower edges of the conductor. This

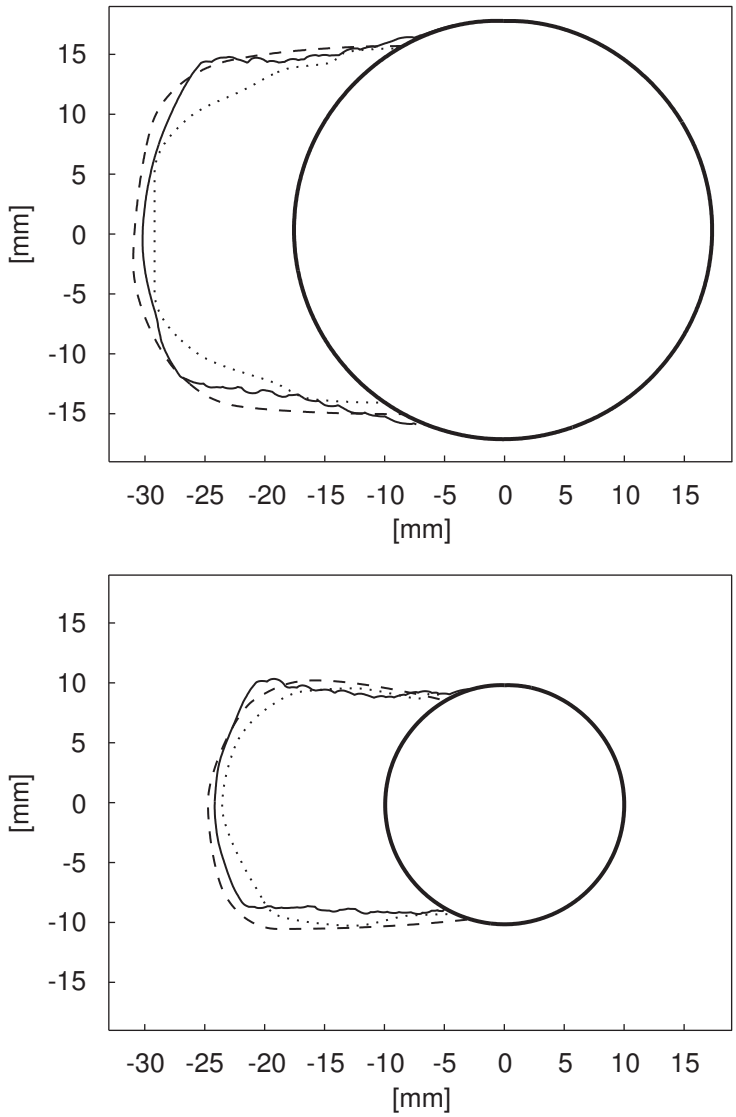

Figure 3.17: Verification of the icing model presented here $(-)$ by comparison with experimentally (- - -) and numerically $(\cdots)$ predicted ice deposits by Fu [37]. The Investigation parameters are a wind velocity $u = 5\,\mathrm{m/s}$, particle diameter $MVD = 34\,\mu\mathrm{m}$, an ambient temperature $T_a = -15\,^{\circ}\mathrm{C}$, liquid water content in the air $LWC = 1.2\,\mathrm{g/m^3}$ and an icing duration of 30 minutes. The diameter of the conductor is $d_c = 34.9\,\mathrm{mm}$ for the lager and $19.5\,\mathrm{mm}$ for the thinner cable.

effect is relatively small for the larger cable but more significant for the smaller one. Obviously, an increase in resolution meaning smaller initial trajectory spacing would solve this problem. However, the model is limited to a minimal initial trajectory spacing of $2.5 \cdot 10^{-4}\,\mathrm{m}$, because of limited computational resources. The results are satisfying, but further experimental studies should be performed to improve icing models in general as well as verify this and other models for a broader range of meteorological conditions.

3.6 Numerical Methods

3.6.1 Numerical Method of the Fluid Dynamic and the Heat Transfer Model

Finite Element Method

The fluid flow and heat transfer described in sections 3.2 and 3.4 are solved with the finite element software COMSOL 3.5a. Methods used by this software are briefly explained in this section. More details on the implementation are given in the software manual [20]. A closer look on the background of finite elements is given by Zienkiewicz et al. [176, 177].

For many physical problems no analytical solution is available . Most of those interesting for engineers and scientists are described by partial differential equations. To solve these problems numerical discretisation techniques like the finite element method are necessary. Given a problem that is described by the following differential equation:

$$A(\phi) + b = 0 \qquad \Omega \tag{3.95}$$

with the differential operator $A(\phi)$ and source term b in the domain Ω. The weak or integral form of the differential equation is given by:

$$\int_{\Omega} a\,(A(\phi) + b)\,d\Omega = 0 \tag{3.96}$$

where a is an arbitrary function chosen to satisfy the equation. If this is true, equation 3.95 is satisfied in the domain. Then we assume an approximation of the state variable:

$$\begin{aligned} \phi \approx \overline{\phi} &= N_1 \cdot x^1 + \ldots + N_m \cdot x^m \\ &= \mathbf{N}_a \cdot \mathbf{x}_a \end{aligned} \tag{3.97}$$

where $\mathbf{N}_a\mathbf{x}_a$ is a test or shape function. Using the approximation function, equation 3.96 does not longer satisfy the differential equation and therefore leaves a residual:

$$\int_{\Omega} a\left(A\left(\overline{\phi}\right) + b\right)\,d\Omega = R_G \tag{3.98}$$

Minimising the residual R_G consequently leads to the best approximation. The residual is driven towards zero by a convolution of R with a weight function W_G:

$$\int_{\Omega} W_G * R_G\,d\Omega = 0 \tag{3.99}$$

The weight function used by the Galerkin weighted residual method is simply the shape function already used in equation 3.97.

This method is very successful in solving elliptical differential equations like the Laplace equation for stationary heat transfer or potential flows for example. Here the information propagates in all directions. Problems with a hyperbolic character, where the information propagates in a dominant direction, show numerical oscillations in the solution. Examples for such problems are flows dominated by the convection term, as it is the case in our fluid dynamic model. The oscillations arise from the approximation, which does not account for the propagation direction. To overcome this problem Streamline-Upwind-Pertove-Galerkin (SUPG) stabilisation techniques can be used. The method used here is called Galerkin Least-Squares (GLS) stabilisation. It adds the differential operator $A\left(\overline{\phi}\right)$ to the weight function:

$$W_G = \mathbf{N}_a + \lambda_s \cdot A\left(\mathbf{N}_a\right) \tag{3.100}$$

where λ_s is a stabilisation parameter. It is important to note, that this approach is consistent and therefore does not perturb the original equation. More details of the implementation in COMSOL 3.5a are given in the user guide [20].

The idea is to solve the problem with a finite number of parameters, the so-called degrees of freedom (DOFs), approximated using the method described above. Therefore, the domain is subdivided into a number of elements. Each of them is specified by a set of shape functions governing the interaction of DOFs located at the element nodes. In a local coordinate system each shape function equals one at a particular node and equals zero at all the other nodes. The order of the shape function defines the order of the elements. We speak of a linear element when the course between the nodes is linear. Furthermore, the elements need to fulfil continuity requirements for physical reasons, to avoid gaps and overlapping of elements. The elements used in this model are Lagrange elements with C_0-continuity. This means that the approximation is continuous at the transition from one to the other element, but not its derivative. Hence, the approximated values are continuous, but not their slope. Elements with C_1-continuity also ensure continuity of the derivatives, such as Hermite polynomials allowing for continuity of computed displacements and stresses, for example. In order to link the individual finite elements with the global coordinate system geometry shape functions are required as transformation functions. When these functions are of the same order as the shape functions we speak of isoparametric elements. At curved boundaries it is beneficial to improve the approximation by using curved elements. Hence, when linear elements are used it would be favourable to use geometry shape functions of higher order. Such elements are called superparametric. In our case mainly isoparametric linear Lagrange elements are used. At curved boundaries linear Lagrange elements with second order geometry shape functions are applied. These elements are only used at the boundary, because there is no reason to make them curved when they do not touch a curved boundary.

Finite Element Mesh

In the previous section we introduced the method of finite elements. Now we take a look at how to discretise the domain of the problem using a mesh of finite elements. The mesh generation is an error-prone process. A structured mesh is created by decomposing the domain into subdomains that are easy to mesh. Such mapping methods are often used to generate a mesh of quadrilateral elements. This strategy usually produces meshes of good quality, but the division in subdomains requires human intervention. Unstructured mesh algorithms can generate meshes for domains of any shape independently. They are especially useful, when element size is supposed to vary in different regions of the domain.

In our case an advancing front algorithm is used to create a two-dimensional mesh of triangular elements. This fully automatic meshing algorithm starts from an initial boundary. It generates elements along a front advancing into regions to discretise until the mesh covers the whole domain. The meshing procedure starts with the generation of nodes along the boundaries. Then it creates elements within the discretisied boundaries of the domain. At the final stage the mesh quality is improved by a mesh smoothing algorithm. The node connections of the elements are not altered, but the nodes are repositioned to achieve a smooth mesh.

One can argue that a triangular mesh is not adequate for fluid dynamic calculation, because of inaccuracies arising from adverse in- and outflow angles at the element boundaries. But due to large number of elements and their random orientation we can consider this effect as negligible for our application. Boundary layer meshes are a particular type used in fluid dynamic problems. They are generated in the vicinity of solid surfaces to accurately resolve the boundary layer. They consist of elongated rectangular elements with a fine discretisation normal to the surface. However, the algorithm tends to fail in generating an appropriate mesh, when the surface curvature is not continuous. The boundary layer meshes created in our ice accretion simulations often showed problems at the transition between ice and cable surface. Therefore, only a mesh of triangular elements with a very fine resolution in the surface region is used. The boundary layer itself is modelled by wall functions.

It is possible to reduce the error in a finite element calculation by mesh refinement. The so-called adaptive mesh refinement improves the approximation by refining the mesh resolution according to the error of the computation. Hence, a fine resolution efficiently focuses the computing power on those regions where it is needed. The three main adaption strategies are h-refinement, r-refinement and p-refinement. Combinations of these are also possible.

The h-refinement changes the topological structure of the mesh by refining or enlarging elements with respect to an error indicator of the previous solution. The simplest strategy for this type of refinement is the subdivision of elements. Another strategy is remeshing of the domain. It is usually time consuming, but in general the meshes are of better quality. A method without changing the number of nodes is the r-refinement. It keeps the total number of elements constant and only adjusts their shape to improve the approximation. Contrarily,

the p-refinement does not change the topology of the mesh. Number and shape of elements are left unchanged. It only alters the order of the elements and consequently the accuracy of the approximation. Choosing an appropriate error indicator is essential for the quality of the refinement. In fluid dynamic problems, a gradient of a solution variable is recommended, such as vorticity [177]. Consequently, the vorticity of the air flow is used as error indicator governing the remeshing with a h-refinement.

Summaries, the mesh is created by an advancing front algorithm generating a mesh of triangular isoparametric linear Lagrange elements. At curved boundaries the geometry shape order is increased to the second order. The maximum initial element size at the ice and cable surface is 10^{-4} m. The element size grows with distance to the surface by a factor of 1.3. An adaptive mesh refinement with two iteration steps is used in a preliminary calculation to provide an optimised mesh for the main calculation. With each remeshing, the number of elements is increased by a factor 1.7. A solution gradient of the flow velocity, the vorticity, is taken as error indicator.

Boundary Layer Treatment

A particular issue of fluid dynamic and heat transfer problems is the treatment of the boundary layer, which forms in a fluid that passes a solid surface. The so-called velocity boundary layer describes the velocity profile and the thermal boundary layer accordingly describes the heat transfer in vicinity of the solid surface. An adequate fine resolution of the boundary layer requires a costly computation, which is not reasonable for the given case. Therefore, wall functions are used to describe the boundary layers and thereby simplifying the simulation. The domain solved by finite elements and the region described by wall functions are coupled and iteratively solved [177].

It is presumed that the temperature has no influence on the flow. Therefore, the computation of flow field and heat transfer are decoupled as explained in section 3.2 and 3.4. The temperature distribution is calculated based on a given flow field and likewise the temperature boundary layer is based on the already determined velocity boundary layer. The thermal boundary layer is modelled as a convective boundary condition at the interface between fluid and solid for a given velocity profile. Details on the equations governing the boundary layers are given in section 3.2 and 3.4.

Finite Element Solver

The equation system of the flow and the heat transfer computation are solved by a segregated solver algorithm. The variables are divided in groups to solve the whole system iteratively. Velocity components of the flow and pressure compose the first group. Turbulent kinetic energy and turbulent dissipation are the second group. The third group includes the variables

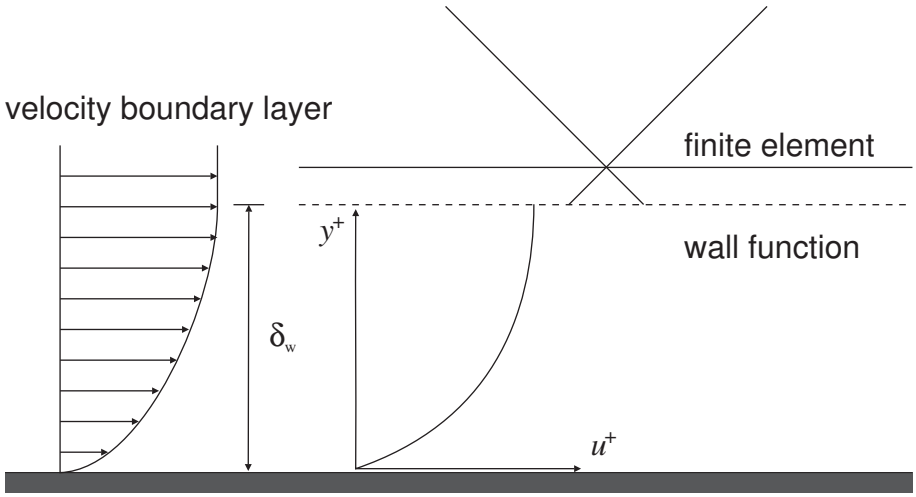

Figure 3.18: Coupling of finite element and wall function domains. The velocity boundary layer is described by a wall function (u^+, y^+) coupled with the computation of the main flow field in the finite element domain.

temperature and radiosity of the heat transfer calculation. Each group is solved by the linear system solver Pardiso [128, 129]. During each step of the segregated solver, each group run through a predefined number of iteration steps. When the estimated error of all groups satisfies the solver criteria, the next step of the segregated solver can start. It terminates, when the estimated error of all groups is smaller than the predefined tolerance [20]. The tolerance of the final error estimate for all groups is $e < 0.001$. More fundamentals of numerical procedures and solver methods are given by Ferziger and Milovan in [31].

3.6.2 Numerical Method of the Multiphase Flow Model

Runge-Kutta Algorithm

The mixed stream of air and precipitation droplets is modelled as a one-way coupled two-phase flow. The motion of the individual particles is described by Newton's second law. To solve this second order ordinary differential equation (ODE), the equation is transformed into a pair of coupled first order ODE. Fourth and fifth order Runge-Kutta algorithms are used to compute two equations in each direction, one for velocity and one for spatial location. The difference between the fifth and fourth order result is used as error estimator [20].

In order to explain the basic procedure of this method, a fourth order Runge-Kutta algorithm is applied on two first order ODE with two variables. More details on these methods can be found in [26]. Generally speaking a Runge-Kutta algorithm is used to solve initial value problems for ordinary differential equations. Supposing two coupled differential equations with two

variables:

$$\begin{aligned} x' &= a_1(t,x,y) \\ y' &= a_2(t,x,y) \end{aligned} \tag{3.101}$$

where x and y are variables and t is the time. The basic idea is to approximate the ODEs in stages. Each step starts from the current value x_n at t_n and ranges to $t_n + h_n$, where h_n is the step size. The value of $a(t_n + h_n, x, y)$ is approximated by a weighted average of values in the interval of $[t_n, t_n + h_n]$. Obviously, the same is done with both variables:

$$\begin{aligned} x_{n+1} &= x_n + h_n \cdot \left(\frac{k_1}{6} + \frac{k_2}{3} + \frac{k_3}{3} + \frac{k_4}{6} \right) \\ y_{n+1} &= y_n + h_n \cdot \left(\frac{j_1}{6} + \frac{j_2}{3} + \frac{j_3}{3} + \frac{j_4}{6} \right) \end{aligned} \tag{3.102}$$

where

$$\begin{aligned} k_1 &= f(t_n, x_n, y_n) \\ j_1 &= g(t_n, x_n, y_n) \\ k_2 &= f\left(t_n + h/2, x_n + k_1 \cdot h_n/2, y_n + j_1 \cdot h_n/2\right) \\ j_2 &= g\left(t_n + h_n/2, x_n + k_1 \cdot h_n/2, y_n + j_1 \cdot h_n/2\right) \\ k_3 &= f\left(t_n + h_n/2, x_n + k_2 \cdot h_n/2, y_n + j_2 \cdot h_n/2\right) \\ j_3 &= g\left(t_n + h_n/2, x_n + k_2 \cdot h_n/2, y_n + j_2 \cdot h_n/2\right) \\ k_4 &= f(t_n + h_n, x_n + k_3 \cdot h_n, y_n + j_3 \cdot h_n) \\ j_4 &= g(t_n + h_n, x_n + k_3 \cdot h_n, y_n + j_3 \cdot h_n) \end{aligned} \tag{3.103}$$

Starting with initial values, the algorithm approximates the solution progressively.

Runge-Kutta Solver

The solver rewrites the equation of particle motion into a pair of coupled first order ODE, as already described in the previous section. Velocity and spatial location are solved for each direction with a fourth and fifth order Runge-Kutta algorithm. The difference between both solutions is used to obtain the error estimate [20]. Velocity as well as spatial location are computed with an error tolerance of $e < 10^{-6}$. The step size of the solver is automatically determined based on the error tolerance and the acceleration. Another important solver parameter is the edge tolerance. It controls how close to a boundary the trajectories are cut, when they leave their model domain. The tolerance is set to $e < 10^{-6}$, which is two orders of magnitude lower than the resolution of the finite difference model. It ensures smooth coupling of the trajectory calculation with the computation of the mass balance at the accretion surface.

3.6.3 Numerical Method of the Ice Growth Model

Finite Difference Method

The geometry of the ice deposit is computed by a finite difference model. The nodes are located at the surface of the conductor and ice deposit with a spacing of 10^{-4} m. The node closest to each particle impact is chosen for the ice growth computation 3.5. Impinging locations of the particles on the surface are defined by the multiphase flow model (cf. section 3.3). Based on impact location, angle and velocity the ice growth model determines the local mass accumulation. Then the ice evolution vectors are computed, including input parameters such as precipitation type and surface temperature. Those vectors are orientated normal to the surface and their length defines the extent of local ice formation. Eventually, the ice surface is shifted along these vectors and new nodes are inserted with the previous spacing of 10^{-4} m. The surface of conductor and ice deposit is described by parametric equations:

$$s(z) = \begin{pmatrix} x(z) \\ y(z) \end{pmatrix} \tag{3.104}$$

where x and y are global coordinates and z is the free parameter. The distribution of nodes along the surface is defined by a cubic spline interpolation that uses piecewise polynomials:

$$\mathbf{S}(z) = \begin{cases} S_0(z) & z \in [z_0, z_1] \\ S_1(z) & z \in [z_1, z_2] \\ \dots & \dots \\ S_{n-1}(z) & z \in [z_{n-1}, z_n] \end{cases} \tag{3.105}$$

with $S_i(z)$ being cubic polynomials. Due to the piecewise polynomials the interpolation error is very small. The first two derivatives are continuous between the polynomials. Hence, a spline has continuous slope and curvature.

The new ice surface defines the geometry for the next simulation step which starts with a new flow calculation.

Finite Difference Solver

The finite difference model is built with functions and methods implemented in MATLAB R2009a. All mathematical operations, such as matrix manipulations or spline interpolations, used by the model are based on the numerical methods of the software package. Their solver procedure is not discussed here, further details on the software are given in [92].

4 Parameter Studies

4.1 Introduction to the Parameter Studies

In this chapter parameters are studied that define the characteristics of ice accretion. Icing events, like the winter storm in Münsterland in 2005 for instance, are not investigated. Such an event would require a simulation ranging over several days of ice accretion and it would also demand modelling of ice shedding which is not included in the model. Those events are only describable by empirical models, which are able to give a rough estimate of occurring static ice loads, as for example presented in [86]. But these models can neither describe an influence of conductor bundles on ice accretion nor can they define the shape of ice deposits, which is required to compute aerodynamic forces.

Wind velocity, particle size and conductor temperature are the parameters here investigated to illustrated characteristics of ice accretion. Ambient temperature is not considered, because it would effect only the heat transfer during an icing event. Since for dry ice growth only an initial computation of the heat balance is required, the ambient temperature has no impact on the ice formation. Also the mass of the deposits is computed, such as it would form on a one meter long section of a conductor. This is not aimed at defining design loads, but rather at comparing the influence of varying parameter.

Subsequently, the temperature distribution in ice deposits is examined to illustrate the heat transfer mechanism of different icing conditions.

Torsion of conductors under ice load is not investigated, because twisting of conductor bundles and eventual capsizing of a bundle would require additional simulation algorithms which so far are not included in the model. Furthermore, torsion of individual cables in a bundle and of the whole bundle depends on the properties of the conductor itself and also on length of the span, number, spacing and design of conductor spacers that keep distance between the cables, which gives a variety of parameters to test that requires an investigation of its own.

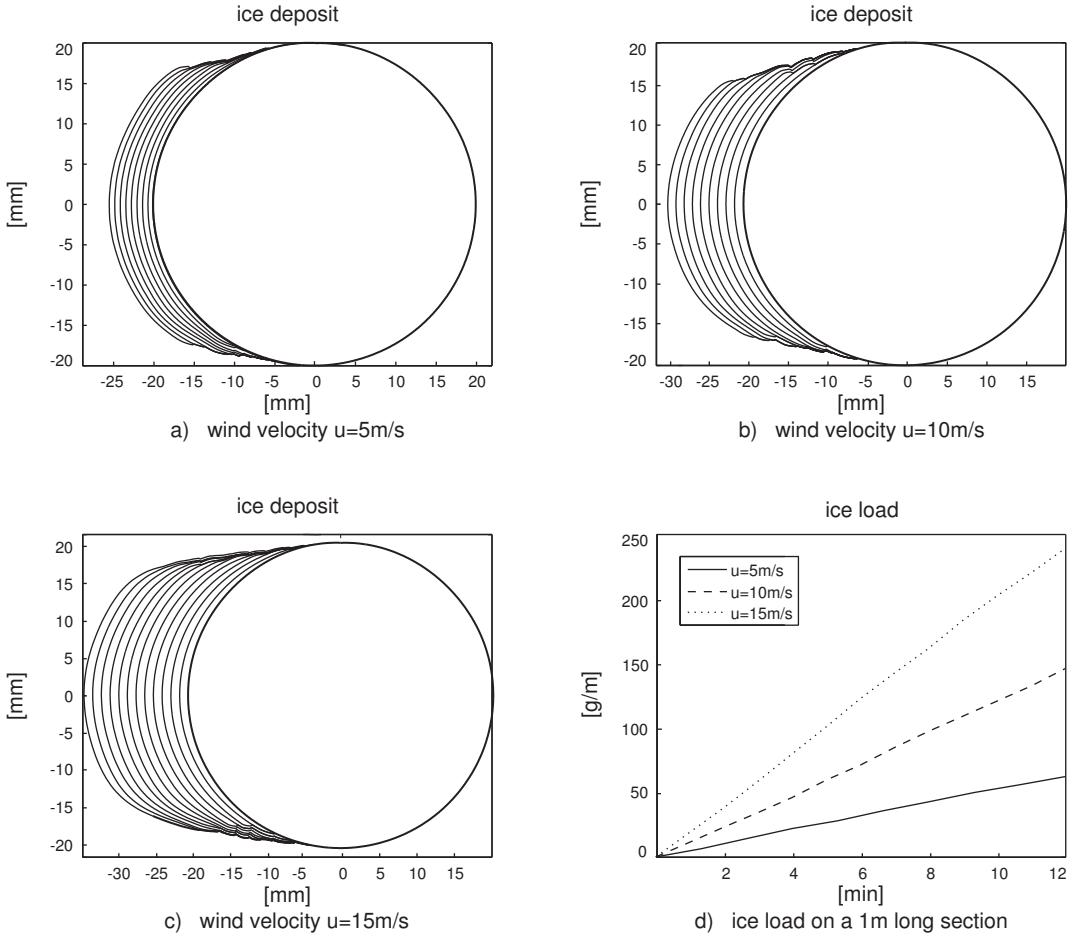

Figure 4.1: Influences of wind velocity on ice formation considering a medium volume diameter $MVD = 30\,\mu\text{m}$, a conductor surface temperature $T_s = -5\,^\circ\text{C}$ and a liquid water content in the air $LWC = 1.5\,\text{g}/\text{m}^3$.

4.2 Influences of Wind Velocity

The difference in size of ice deposits is the most obvious influence wind velocity has on ice accretion. Greater flow velocity means a larger mass flux of icing particles and consequently faster growth of ice. Moreover, a greater velocity of the airflow also causes particles to impinge further to the upper and lower edge as we can see in figure 4.1a and 4.1b. The latter figure also shows that the ice body becomes slightly streamlined with increasing wind velocity. Another effect is also the influence on the evolving ice density. Obviously, a faster airflow increases the particle velocity which then has a higher impact speed. With increasing impact velocity the ice density increases, because the particles are more densely packed when impinging on the surface. But the variation in ice load, we observe in figure 4.1d, is mainly due to differently sized ice mass caused by the variation in wind velocity.

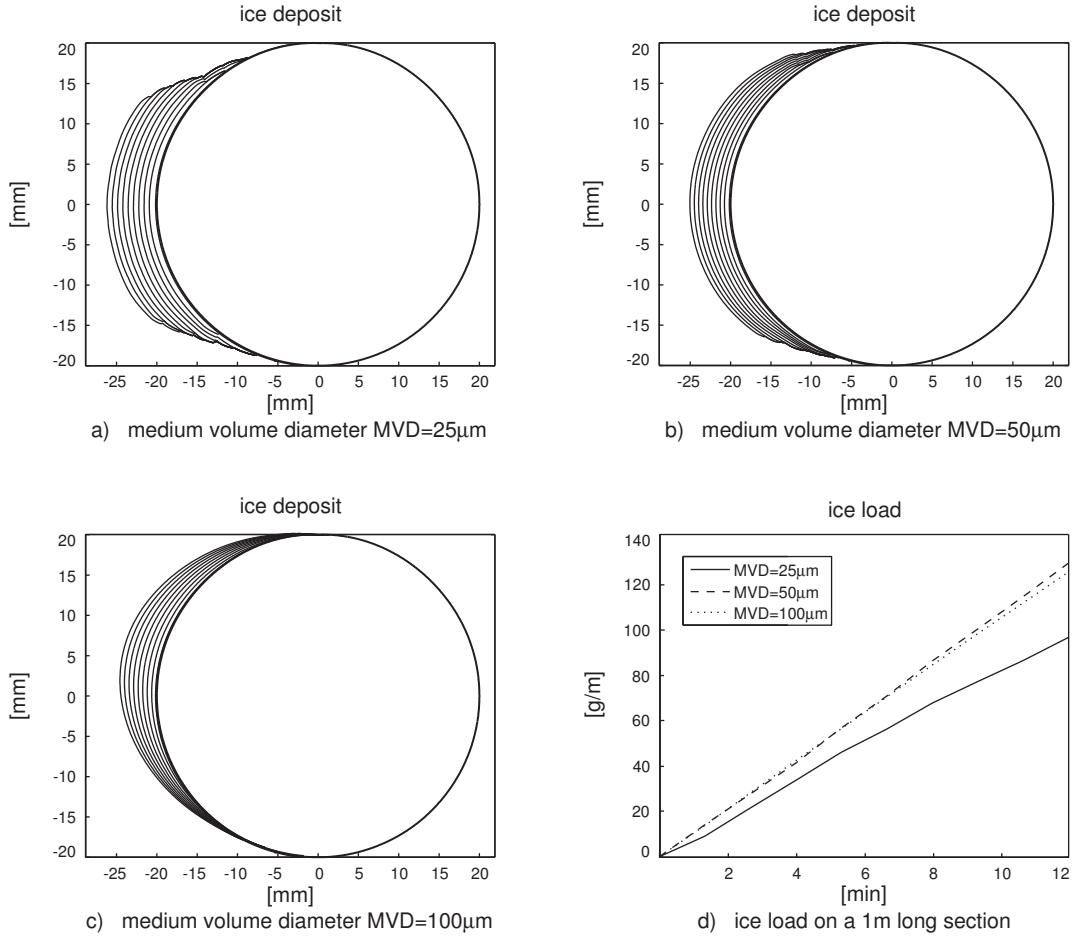

Figure 4.2: Influences of medium volume diameter on ice formation considering a wind velocity $u = 5\,\mathrm{m/s}$, a conductor surface temperature $T_s = -5\,^{\circ}\mathrm{C}$ and a liquid water content $LWC = 1.2\,\mathrm{g/m^3}$.

4.3 Influences of Medium Volume Diameter

A analysis with different medium volume diameters illustrated the influence of the type of precipitation and the droplet spectra. In figure 4.2a we can see that a fraction of particles are dragged around the conductor by the wind due to their low inertia. Therefore, the ice body becomes more streamlined than it is the case for larger droplets as displayed in figure 4.2b for example. Here, the ice deposit has almost the curvature of the conductor underneath. It is not streamlined, because the inertia of the droplets is too high to allow them to follow the airstream. The larger droplets also cause a higher density which leads to greater ice loads as displayed in figure 4.2d. The mechanism defining the collection of particles on the surface changes for droplets larger than those considered in the two previous cases. In figure 4.2c we can see that the ice deposit becomes even more streamlined than in the case of small cloud droplets shown in figure 4.2a and 4.2b. This is due to splashing of freezing raindrops when

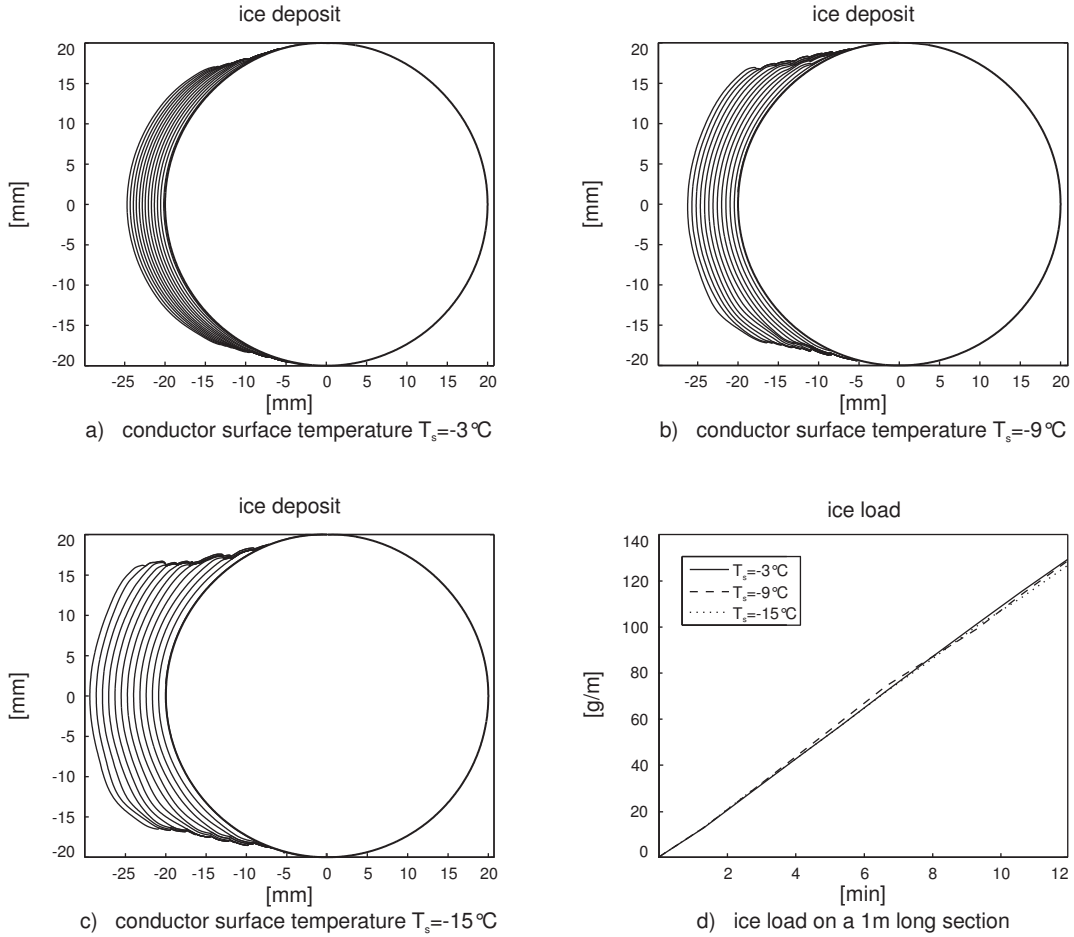

Figure 4.3: Influences of conductor surface temperature on ice formation considering a wind velocity $u = 5\,\mathrm{m/s}$, a medium volume diameter $MVD = 40\,\mu\mathrm{m}$ and a liquid water content $LWC = 1.2\,\mathrm{g/m^3}$.

they impinge on the surface. The fraction of particles sticking to the surface depends on the impact angle and therefore ice is growing faster at the center of the conductor cross-section. The larger droplets also cause higher ice loads, which is due to a greater density. Furthermore, we can observe that in figure 4.2a and 4.2b the ice grows horizontally, because the mass of the droplets is so low that gravity hardly affects their trajectories. Due to a larger mass trajectories of rain drops are inclined due to their larger mass. Hence, the ice displayed in figure 4.2c is inclined, because it grows towards the particle flux.

4.4 Influences of Conductor Temperature

An investigation of different conductor surface temperatures shows no effect on shape and mass of the ice deposits under dry growing conditions as shown in figure 4.3. Both quantities are

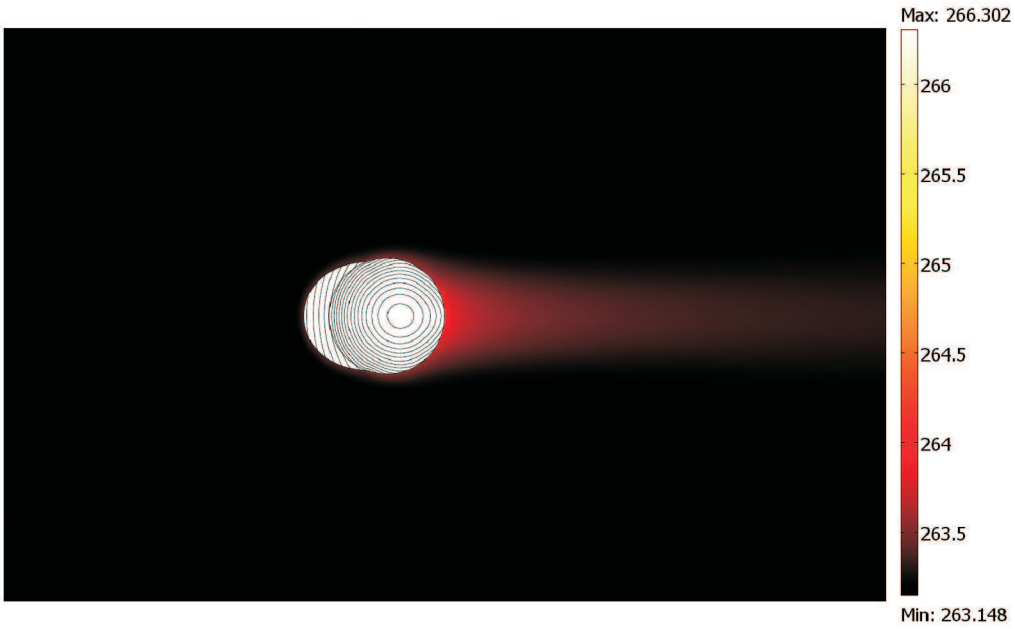

Figure 4.4: Temperature distribution of an energized conductor with rime ice accretion and a surrounding airflow. There is no precipitation and consequently no further ice growth.The simulation parameters are a wind velocity $u = 5\,\mathrm{m/s}$, an ambient temperature $T_a = -10\,^{\circ}\mathrm{C}$ or $T_a = 263.15\,\mathrm{K}$ respectively and a power generated by the conductor of $46.2\,\mathrm{J/s}$.

insensitive to the conductor temperature under such icing conditions, because heat transfer does not cause melting and therefore the ice density is only marginally effected. Only a simulation of wet growing conditions would show an effect on ice shape and density. But this is not possible, because the icing model can not account for a liquid layer forming under wet growing conditions.

4.5 Temperature Distribution in Wet and Dry Ice Formation

An analysis of an iced conductor shows small variations in temperature within conductor, ice deposit and surrounding airflow. The differences are small enough to consider a uniform temperature at the conductor surface. However, the contour plots reveal interesting characteristics of temperature distributions in different icing conditions. Figure 4.4 displays an energised conductor with rime ice deposit.

The ice does not grow and no precipitation contributes to the heat balance. Concentric contour lines in the conductor show that the temperature declines more sharply towards the ice deposit than towards the air. This is due to the conductive heat transfer between ice and conductor,

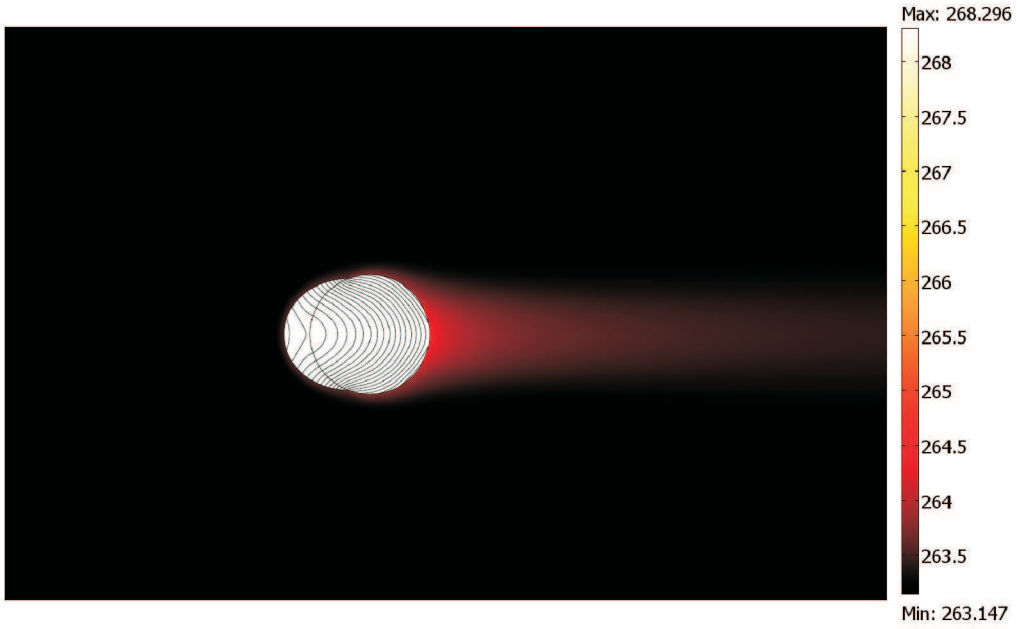

Figure 4.5: Temperature distribution of an energised conductor with rime ice accretion under dry growing conditions. Precipitation contributes to the heat balance at the freezing interface. The simulation parameters are a wind velocity $u = 5\,\mathrm{m/s}$, an ambient temperature $T_a = -10\,^{\circ}\mathrm{C}$ or $T_a = 263.15\,\mathrm{K}$ respectively and a power generated by the conductor of $46.2\,\mathrm{J/s}$.

which is larger than the convective heat transfer between air and conductor. Within the ice deposit the heat energy is conducted towards the surface. Consequently, the temperature declines with distance to the conductor surface. The temperature distribution changes when the ice deposit starts growing. At the tip of the ice body more ice forms than at the edges and more heat energy released during freezing has to be dissipated at the tip as we can see in figure 4.5. Close to the upper and lower edge the heat flux is smaller, which is a consequence of less ice forming there.

Finally, a conductor under wet ice growing conditions is examined as displayed in figure 4.6. A liquid water layer covers the surface of the ice accretion. This water film is at the transition to freezing and therefore the temperature at the freezing interface is considered to be $0\,^{\circ}\mathrm{C}$. As we can see the temperature within the ice deposit decreases with distance to the ice surface, which is at $0\,^{\circ}\mathrm{C}$. This uniform temperature at the surface is due to the heat transport within the film. The temperature distribution in the conductor is similar to the case presented in figure 4.4, where the contour plot shows a concentric decrease in temperature which is steeper towards the ice deposit.

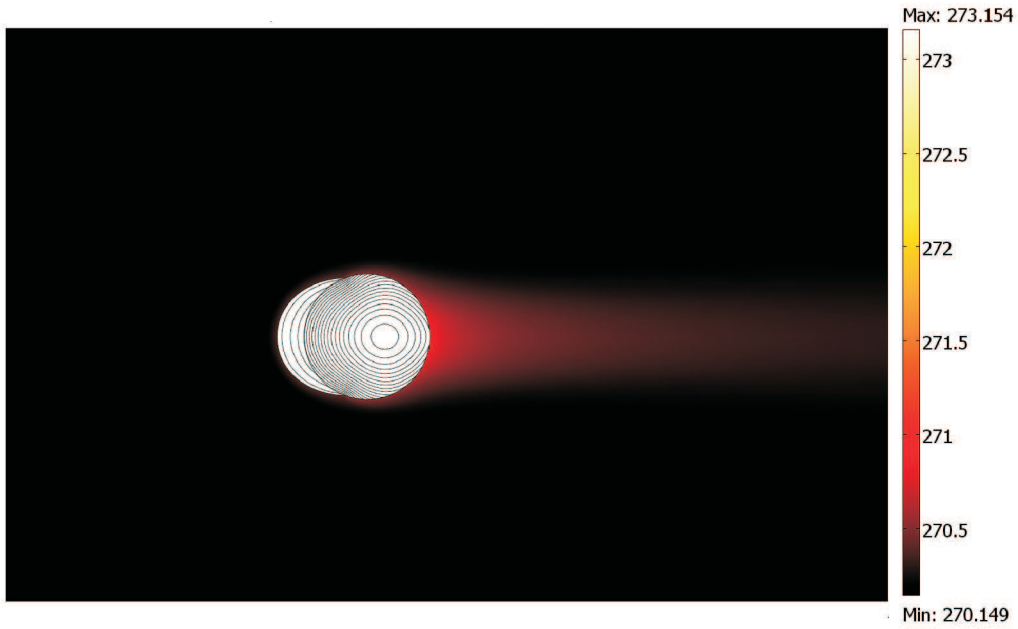

Figure 4.6: Temperature distribution of an energised conductor with glaze ice accretion under wet growing conditions. The temperature at the freezing interface is therefore $0\,^{\circ}\mathrm{C}$. The simulation parameters are a wind velocity $u = 5\,\mathrm{m/s}$, an ambient temperature $T_a = -3\,^{\circ}\mathrm{C}$ or $T_a = 270.15\,\mathrm{K}$ respectively and the conductor generates a power of $46.2\,\mathrm{J/s}$.

4.6 Characteristics of Icing of Conductor Bundles

In order to evaluate screening effects in conductor bundles two conductors arranged inline are examined. Figure 4.7 shows an example of ice accretion on such a bundle with different degrees of inclination. Neither the cables nor the whole bundle experience torsional displacements during the simulation. The reasoning is that in doing so we can compare the collection efficiency of up- and downstream conductor by comparing the accumulated ice mass. Each computation considers six minutes of icing for a fixed inclination of the bundle. The first simulation with a torsional displacement of $\psi = 0\,\mathrm{rad}$ leave the downstream cable without any ice deposit. Only the upstream conductor catches icing particles that form the deposit shown in figure 4.7b. With increasing inclination the downstream cable moves upwards out of the shadow caused by the upstream conductor. Figure 4.7c shows how a small ice deposit forms on the upper edge of the cable. The screening effect diminishes as the torsion increases further, so that the ice body displayed in figure 4.7d is only affected at the lower edge. Eventually, the downstream conductor leaves the shadow of the upstream one and the ice forms identically on both cables as we can see by comparing figure 4.7b and 4.7e. Taking the ice mass on the upstream cable as reference, we observe an ice accretion of 11 % for a torsional displacement of $\psi = 0.0167\,\mathrm{rad}$, of 86 % for $\psi = 0.0333\,\mathrm{rad}$ and of almost 100 % for $\psi = 0.05\,\mathrm{rad}$.

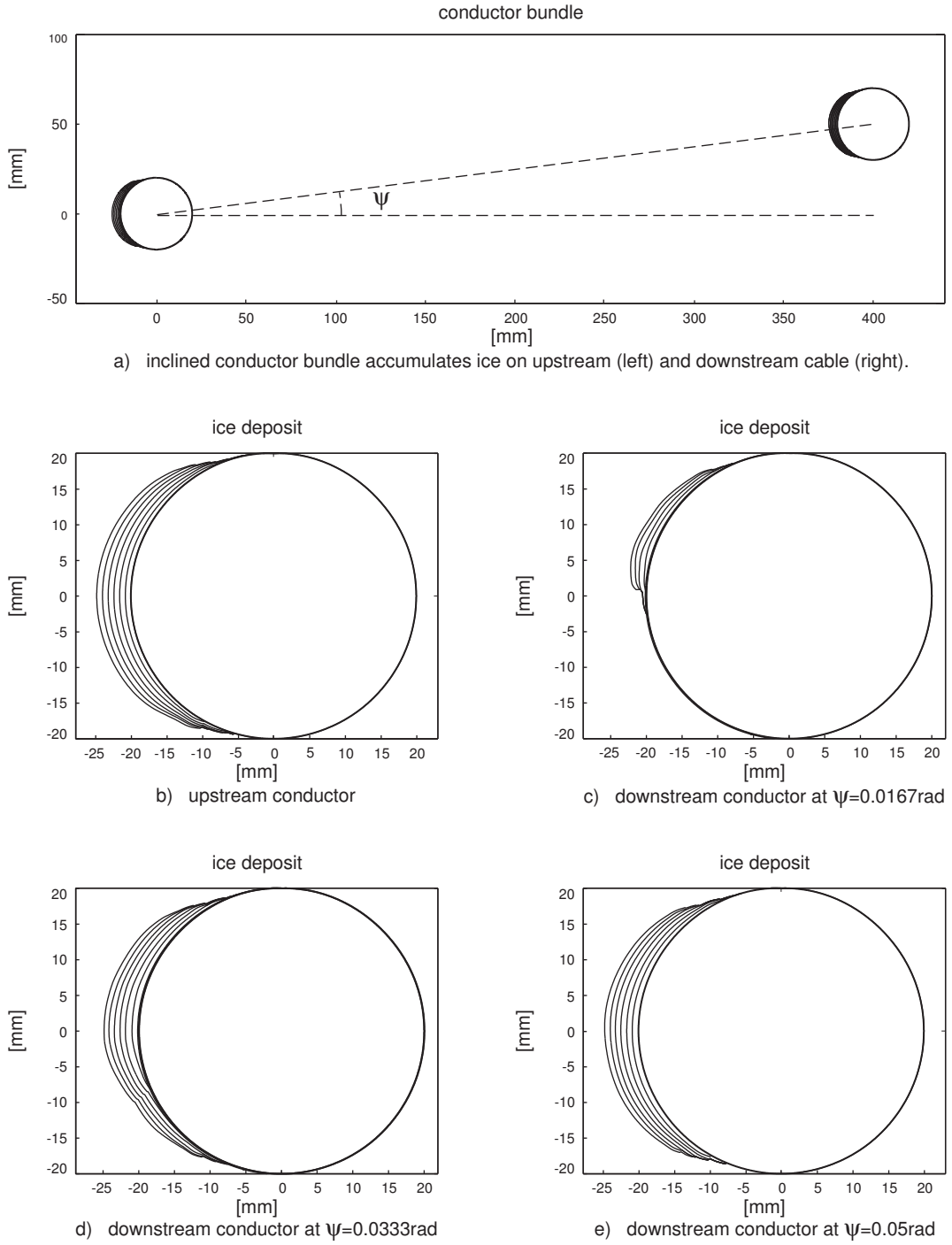

Figure 4.7: Influence of bundle torsion on ice formation on a generic conductor bundle. The bundle consists of two conductors with a diameter of $40\,\mathrm{mm}$ arranged inline with a spacing of $400\,\mathrm{mm}$. The simulation parameter are a wind velocity $\mathrm{u} = 10\,\mathrm{m/s}$, a medium volume diameter $\mathrm{MVD} = 28\,\mu\mathrm{m}$, a conductor temperature $\mathrm{T_s} = -5\,^{\circ}\mathrm{C}$ and a liquid water content $\mathrm{LWC} = 1.2\,\mathrm{g/m^3}$.

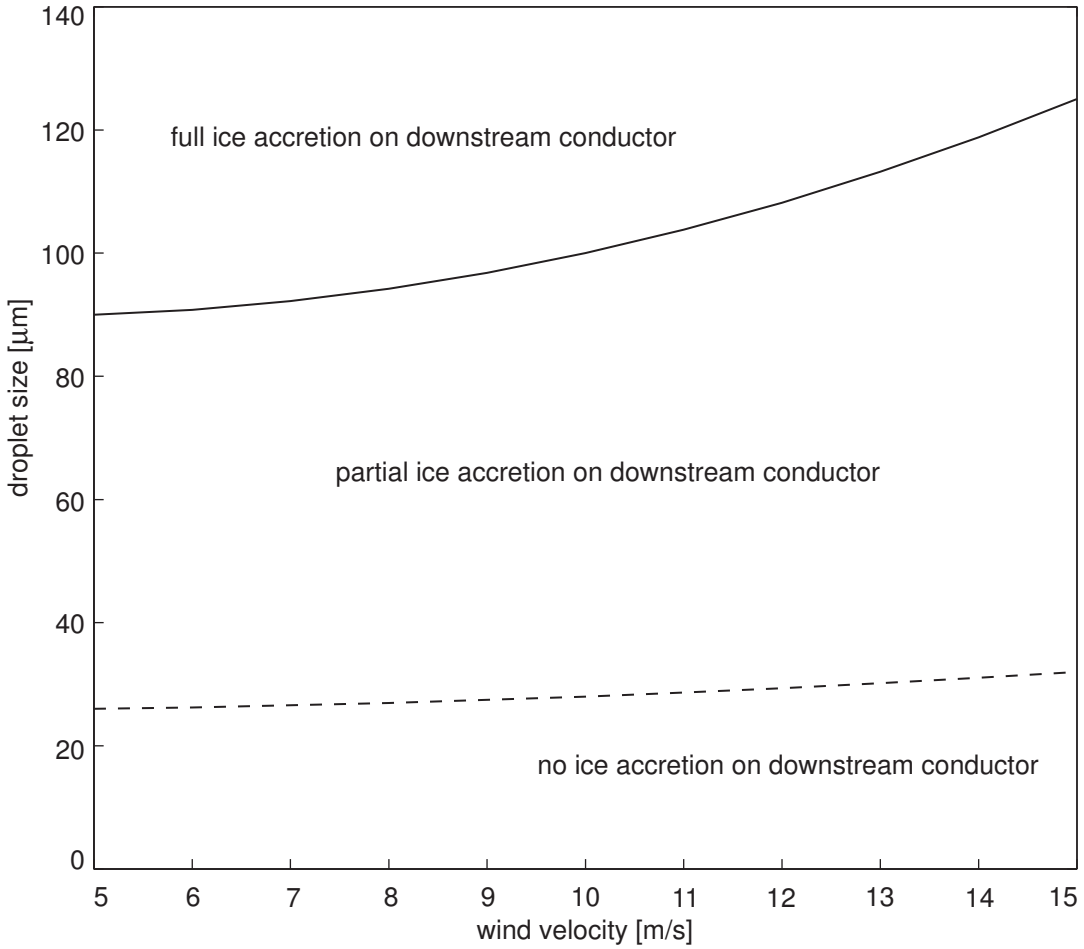

Figure 4.8: Influence of wind velocity and droplet size on ice accretion on a generic conductor bundle. The bundle consists of two conductors with a diameter of $40\,\mathrm{mm}$ arranged inline with a spacing of $400\,\mathrm{mm}$.

Figure 4.8 indicates that tandem arrange of conductor can reduce or even prevent ice formation on a downstream cable. The investigation analyses wind velocities that are associated with major ice loads. Higher as well as lower wind speeds are commonly not examined in atmospheric icing of structures. The first does not seem to occur together with precipitation leading to notable ice accretion. And the latter does not lead to significant ice loads, because the mass flux of precipitation particles on the conductor surface is too low. Whether it is beneficial or not to increase torsional stiffness of a conductor bundle to reduce the total static ice load is not clear. An increased torsional stiffness would improve the galloping behaviour of a bundle (cf. section 2.5.2). However, unevenly iced conductors can cause twisting of the whole bundle, which can lead to significant damages and therefore an evenly loaded bundle might suffer less severe damages during an icing event. If it is possible to reduce static ice loads on transmission lines by increasing torsional stiffness while also preventing twisting of bundles due to ice loads would be an interesting field of research.

Inline arrangement of three conductors could benefit from screening effects of the upstream cylinder and also reduce twisting, for example. The centre of gravity remains close to the conductor in the middle, since the ice load on the upstream cylinder is balanced by the last cable in the row.

5 Risk and Variance in Hazard Duration

5.1 Risk Management Framework

Understanding and evaluating risks is not a trivial task. The concept of risk was first introduced in economics, later in health science and more recently it has been introduced in civil engineering. A risk management framework presented by Urban gives an overview on risk definitions and their implication for civil engineering [153]. This section will explain his framework which consists of four major parts: identifying, assessing, treating and reviewing risk.

Risk identification is commonly a domain of authorities and society stakeholders. Therefore it is not discussed in detail here. Engineering research mostly focuses on risk assessment and treatment. However, the exchange of information between the different parties is important.

Risk assessment is composed of risk analysis and risk evaluation. The analysis is further subdivided in hazard analysis, determination of damage and loss assessment. All aspects of hazardous events regarding intensity and occurrence probability are incorporated in the hazard analysis. The determination of damage includes structural damages or malfunctions of a system. The link between the hazard intensity and the resulting damage is defined as vulnerability. It is important to distinguish between structural damages or malfunctions of a system and loss, which is the monetary consequence of structural damages or malfunctions.

Loss comprises both direct and indirect cost of an event. Direct consequences are immediately related to the damages. Indirect consequences may be understood as follow-up costs due to absence of functionality after destruction. It is possible to further subdivide the consequences

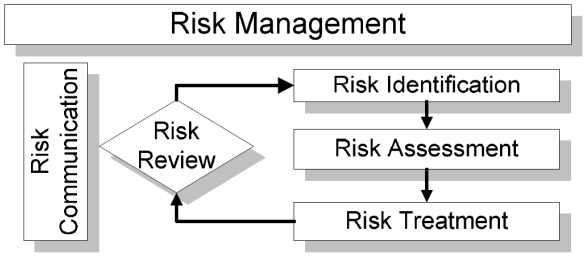

Figure 5.1: Risk management [153].

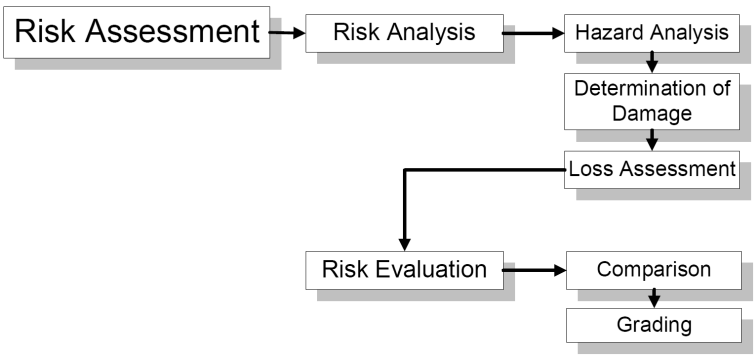

Figure 5.2: Risk assessment includes hazard analysis, damage determination and loss assessment as well as comaprison and grading of risks [153].

in tangible economical losses and intangible losses such as human lives, ecological damages or social, cultural and historical losses. Obviously, intangible losses are difficult to assess and further questions may arise. Considering a system with a number of elements in a hazard scenario, we refer to the individual element as element at risk and the whole number of elements is called a system. In addition to Urban's framework we introduce the term hazard scenario to describe the element at risk due to a certain event. In other words, it is the exposition of elements at risk to a given hazard. Subsequently, the results of the risk analysis are compared and graded in the risk evaluation, where risk classes or acceptable risk levels are defined.

The risk treatment follows the risk evaluation. It consists of decisions and actions to handle the risk. Depending on the risk evaluation actions are undertaken and projects are implemented. If the risk lies within an acceptable range, it is accepted and no further actions are necessary. If the risk is classified as too high, it is rejected and reduction strategies are evaluated. One strategy would be the transfer of the risk to an insurance company, for instance. Another strategy could be the mitigation of risk by technical improvements, for example. Obviously, a combination of both is also possible. Risk mitigation includes disaster management considering technical prevention, social or organisational preparedness and response activities to a disaster. The time interval necessary to reach the pre-disaster state is called recovery time.

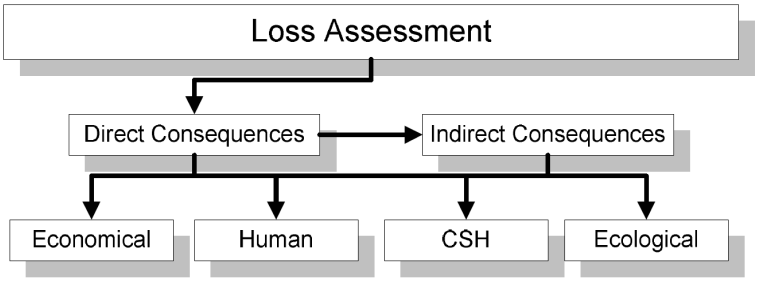

Figure 5.3: Loss assessment considers loss of human lives, economical and ecological damages as well as cultural, social and historical (CSH) losses [153].

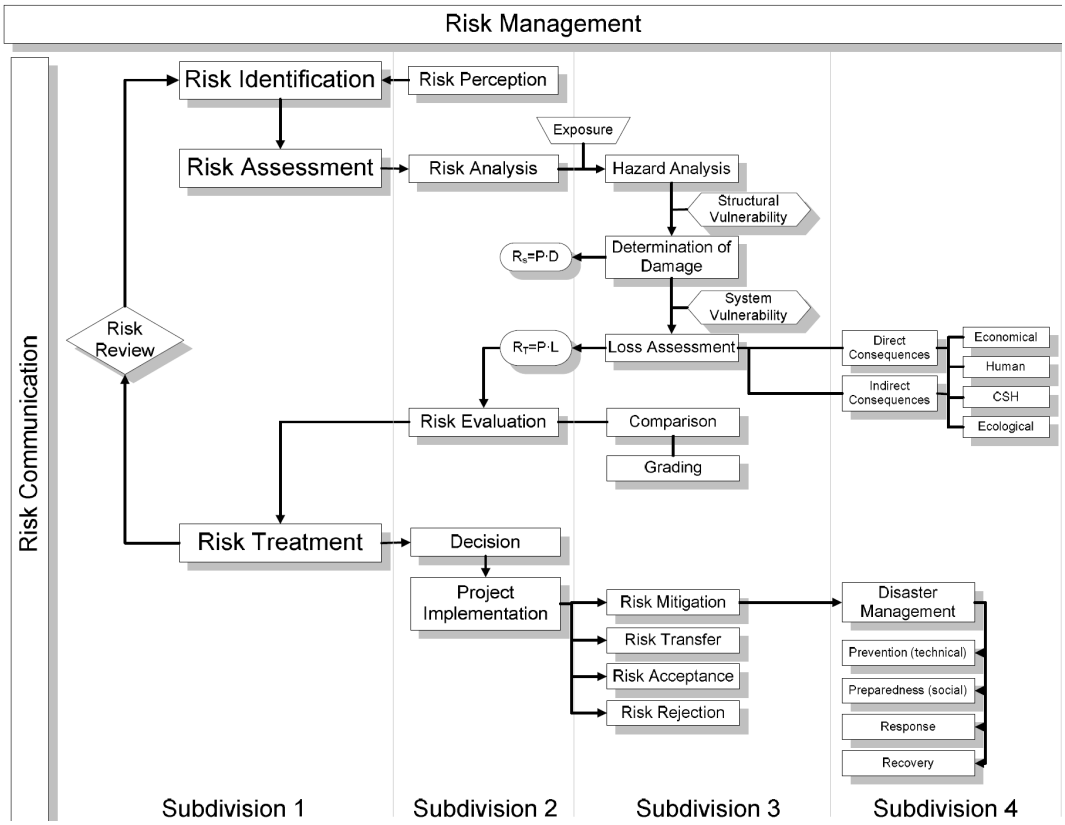

Figure 5.4: Risk management framework [153].

Finally, the risk review gathers all information and experiences of the previous steps to enhance the risk management process. Additionally, during the risk review, risk identification can be reassessed and adjusted as well as risk assessment and risk treatment.

5.2 Risk Aspects of Electricity Blackouts

Based on the risk management framework a multi-hazard scenario of wind and ice action on transmission lines is considered. The origin and the course of an electricity outage due to winter storms have a variety of aspects. There are occurrence probability and intensity of meteorological phenomena like freezing rain and the general influence of geographic characteristics. On a smaller scale there are factors such as topography, the turbulent wind field and the mechanism of atmospheric icing, which have an effect on wind and ice action. Obviously, not only the loading but also the vulnerability of the structure to fatigue damages or even sudden failure of towers, conductors or insulators is important. Winter storms are not commonly considered as natural hazards such as earthquakes or floods, even though they have devastating consequences for towers and power transmission lines [6, 48]. In January 1998 such an event caused a major blackout in Northern America. In Canada alone over two million

people where left without electricity for weeks. About 1300 high voltage power-line towers and roughly 35 000 distribution-line towers failed under ice and wind loads. The incident caused significant monetary damage amounting to billions of dollars [82]. A much smaller event occurred in Germany in November 2005. It left approximately 250 000 people without electricity for up to a week and caused monetary losses of over 100 million Euro [13, 86, 142]. However, not only major events cause enormous damages. A large number of single structures failing due to minor events cause significant damages when seen in total [70, 104]. The major problem is not structural damages themselves, but the resulting monetary losses due to a blackout. A short circuit is not necessarily a consequence of structural damages, also iced insulators or clashing of oscillating conductors can cause outages, as already described in section 2.5. Moreover, such a short circuit can trigger a so-called cascading failure within the power network. As a consequence of the short circuit relays with hidden faults can produce a local overload within the network. When the overload exceeds a certain threshold, the failure can propagate throughout the network [101].

With the increasing demand of energy and increasing usage of network capacities the vulnerability of modern societies to blackouts grows. Therefore, the German Federal Office of Civil Protection and Disaster Assistance (Bundesamt für Bevölkerungsschutz und Katastrophenhilfe (BBK)) conducted a disaster simulation in order to investigate likely consequences of blackouts for modern societies [11]. The simulation scheme of LÜKEX2004 assumed an extensive electricity outage in the region of Baden-Württemberg (Germany). A winter storm in combination with heavy snow fall was assumed to have caused the collapse of major power lines. The storm was chosen to have a magnitude of the storm Lothar, which left severe damages in central Europe in 1999.

An obvious outcome of this investigation is the interference with telecommunication, internet and online money transfer. Emergency electricity of landline communication networks lasts only for a few hours. Wireless networks for mobile phones even shorter. Hence, lacking electricity also means lacking the prerequisite for modern telecommunication systems such as telephones and internet.

A less obvious problem arises from modern food production, which is organised like industrial facilities. Chicken farms or rather chicken factories need air conditioning to keep the animals alive. Without energy, a majority of them dies within half a day due to a lack of oxygen, which leaves a huge number of dead animals to deal with. Another problem arises from interruption of public transport with tram lines or high speed trains. Private traffic is disturbed, because traffic lights are not working. Moreover, petrol stations need electricity to pump the fuel. Since they rarely have emergency electricity or the possibility to use manual pumps, most of automobile traffic will stop within a few days. Hence, after a certain time also transportation becomes difficult.

Furthermore, a blackout limits commercial activities and industrial production. From a scientific point of view this field is most suitable for determining monetary losses and consequently

Figure 5.5: Failed transmission line towers due to ice loads in Münsterland (Germany) 2005 [12]. (with permission of RWE)

the risk of power outages. However, with time also gas and water supply as well as waste disposal is interrupted or at least affected. Even essential needs like medical services are affected. In consequence of limited communication and transportation also food supply is in danger. An average supermarket receives new goods once a day. The products are delivered by truck, needing fuel. Logistic centres need communication lines to distribute the goods and organise the trucks. Additionally, cool storages need a lot of energy. Once the products are in the shops the electronic accounting systems do not work. People may run out of cash money after a few days, since cash machines also need electricity and counters in banks are probably overcrowded, if the service can be provided at all. Debit or credit cards do not work either.

So far, the consequences for police, fire brigades and ambulances have not been mentioned. Moreover, continuing electricity outage may provoke prison breaks. It is probably easier to escape and additionally the police will have difficulties to chase the escapee. Some of the above mentioned problems can be solved or reduced by unconventional or just practical approaches. Experienced employees in a logistic centre might be able to keep the processes running without the entire infrastructure working. Fuel could be pumped with self made equipment. However, the overall scenario remains.

All aforementioned problems deal either with the exposure, the vulnerability or the damage of the scenario and subsequently with losses. Thus, they contribute to the risk equation of

damages:

$$R_D = P \cdot D \tag{5.1}$$

where P is the occurrence probability and D is the damage or malfunction. The risk equation in terms of losses is given by:

$$R_L = P \cdot L \tag{5.2}$$

where L is the monetary damage. In this section we will focus on economic losses. In case of blackouts, the major risk lies in monetary damages. Compared to earthquakes, the number of human casualties - if any at all - caused by the direct impact of blackouts is likely to be very small. The economical estimation of losses is based on the assumptions of marked prices, quantities of certain commodities and average construction costs just to mention some parameters. Therefore, it comprises many uncertainties that need to be modelled to estimate the risk. Doing so, leads to questions like the following:

- Can we treat blackouts like earthquakes or floods in terms of loss assessment?
- What if the risk evaluation determines an equivalent risk for completely different events?
- How is the risk function to be handled, if there are several elements at risk and focusing response activities to one element could shorten the recovery period of this element?
- What do focused response activities mean for other elements?
- Do focused activities change the total recovery time of all elements, even though the magnitude and the occurrence probability of the damage are unchanged?

The loss estimation of blackouts presented in the literature show some characteristics. A closer look on this aspect is given in the following section.

5.3 Variance in Hazard Duration

A particular characteristic of costs of blackouts is their exponential increase over time [156]. No matter which type of consumer or which method of investigation is used, the cost functions are always increasing exponentially with time. There are three categories of methods to investigate the cost of outages. Analytical investigation methods estimate the cost of electricity interruption by associated indices affected by foregone production, for example. These methods can be applied relatively easily by using available data, which on the other hand is linked to limiting assumptions [156]. Outage costs of extensive blackouts can also be assessed by case studies of historical events. Even though those studies are based on a particular case and not necessarily easy to generalise, they indicated that indirect costs are much higher than direct costs [156]. Probably the best method to estimate direct, short-term costs of outages is a customer survey.

But this is a costly and time consuming approach [156]. Independent of investigation methods the course of the function seems to be always exponential. This is true also when different types of energy consumers are distinguished. For example, a study on commercial, industrial and residential customers showed different cost functions for each sector, but they all where exponential functions[51]. Also if a special cause of the electricity outage or a single region is considered, the characteristic is the same, as shown for example by a study on wildlife-caused outage costs in California [143].

In order to investigate the risk of blackouts and the effect of the duration we consider a generalised cost function with low initial costs and an exponential increase (cf. figure 5.6). None of the functions presented in the literature are considered here, because they investigate specific cases. We focus on the general effect of variance in hazard duration and what consequences it may have in comparison to other disastrous events. For this comparison we require another cost function of a different disaster. An event with high initial cost and a linear increase over time, for instance. To the author's knowledge, there only are investigations on cost accumulation over time after blackouts. This might support the idea that the exponential increase of cost is a particular characteristic of outages. For comparison, we assume a dam failure, having a distinct cost function with high initial cost due to the damages on the dam and the flooded area (cf. figure 5.6). The cost increases linearly over time, because of business interruption and alternative residences for inhabitants of the flooded area. The spatial extension of such an event is relatively small compared to a widespread blackout. Losses of human lives are not accounted for here. Losses of human lives are an important issue in risk management, but estimating the value of human live is beyond the focus of this work and is therefore omitted here. The crucial point of this investigation is:

- How can we asses risk, when two different events imply the same risk?
- How should we distribute our response activities, when there are several elements at risk?

Therefore we look at an electricity blackout and a dam failure bearing an equivalent risk. For both cases occurrence probabilities and magnitude of the initiating event are presumed to be fixed. Just the recovery time and therefore the losses may vary. The accumulated losses due to the outage L_E and the dam failure L_D are given by:

$$L_E = CST_E\left(t_E\right) \tag{5.3}$$

and

$$L_D = CST_D\left(t_D\right) \tag{5.4}$$

where CST_E is the cost function depending on t_E the recovery time of the blackout and CST_D and t_D are cost function and recovery time of the dam failure respectively (cf. figure 5.7). Hence, the monetary risk of an electricity outage is calculated by:

$$R_{L,E} = P_E \cdot L_E \tag{5.5}$$

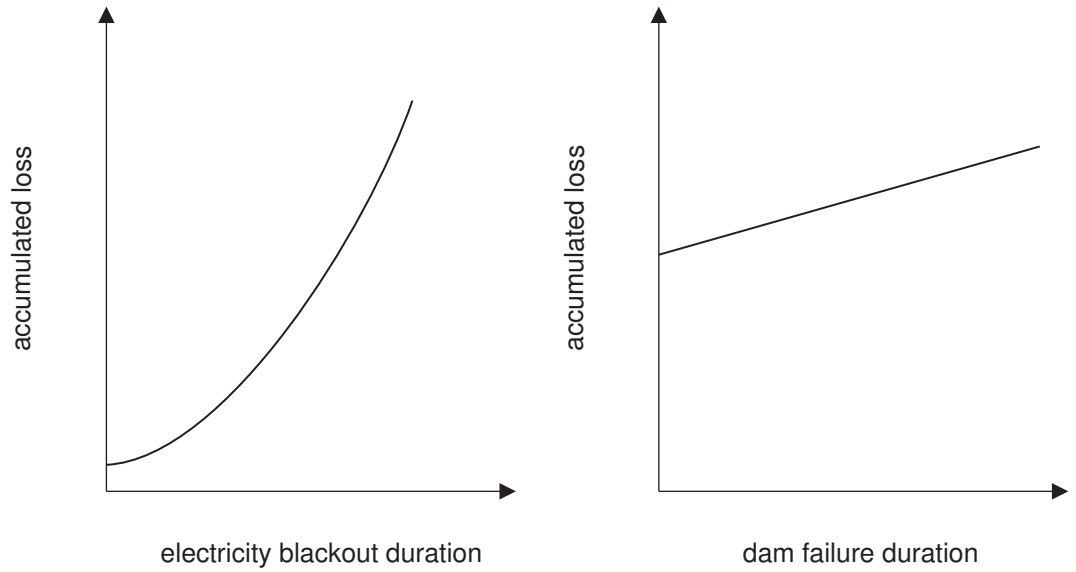

Figure 5.6: Assumed generalised cost functions over time for blackout and dam failure.

where P_E is the occurrence probability of the outage. Likewise the monetary risk of the dam failure is determined by:

$$R_{L,D} = P_D \cdot L_D \tag{5.6}$$

where P_D is the occurrence probability of the dam failure.

Obviously, examining the losses due to blackouts includes assumptions regarding the duration. Thus, a variance in duration can be measured in a variance of risk, considering all other parameters to be fixed.

Figure 5.7 shows the effect of time on both functions. In order to account for uncertainties in time we assume a distribution of relative time deviation: that is to say, a deviation in presumed recovery duration is expressed as percentage of the recovery time. The distribution of relative time deviation is unknown. Here we assume a centered normal distribution. One might argue, quite convincingly, that there are technical constraints requiring a minimum time interval to establish the pre-disaster state. Thus, it might be more reasonable to use a Gamma distribution starting with zero at the minimum possible time interval increasing towards the expected value of recovery duration and tending again to zero towards plus infinity. However, for the sake of simplicity and due to the fact that no data is available to establish such a distribution, we choose a centered normal distributed relative time deviation here (cf. figure 5.8). The variance of the centered normal distribution is not known. In order to avoid a randomly chosen variance, a range of variances is tested. For each variance the 95%-quantile of the distribution is computed. It is used to account for the upper limit including 95 % of the time deviation. It leads to a total loss in case of delayed recovery of:

$$L_{E,D,0.95} = CST_{E,D}\left(t_{E,D} \cdot (1 + q_{95\%})\right) \tag{5.7}$$

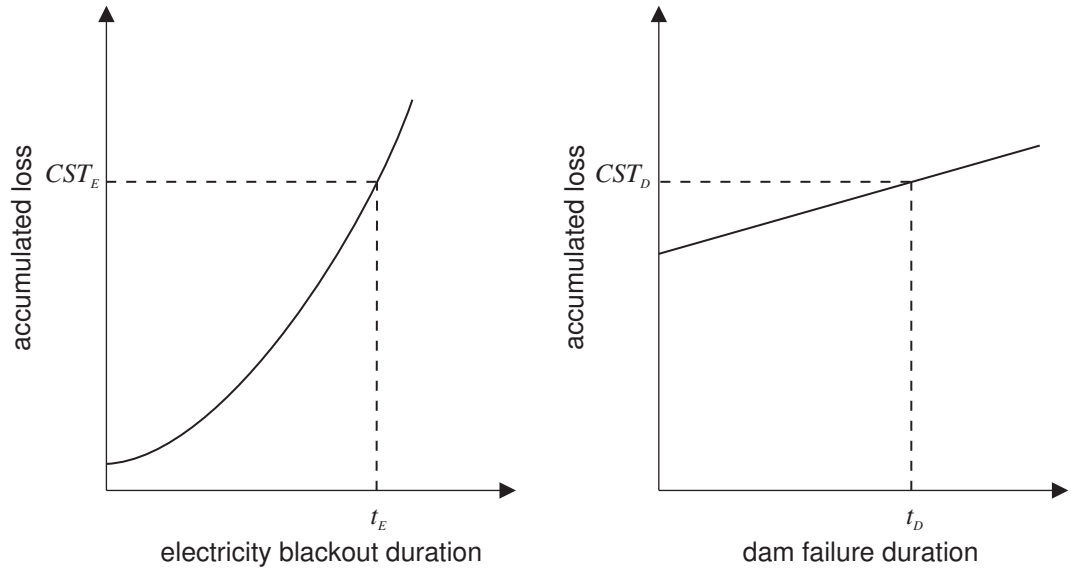

Figure 5.7: Costs due to electricity blackout CST_E and dam failure CST_D after a time interval t_E or t_D respectively.

where $q_{0.95}$ is the 95%-quantile. Subtracting instead of adding the 95%-quantile gives the lower limit of losses, which is exceeded by 95 % of the time deviation:

$$L_{E,D,0.05} = CST_{E,D}\left(t_{E,D} \cdot (1 - q_{95\%})\right) \tag{5.8}$$

The benefit, meaning the money saved, of a fast recovery is calculated by:

$$\Delta L_{E,D,\min} = L_{E,D} - L_{E,D,0.05} \tag{5.9}$$

To determine the maximum and minimum expected loss, we take the average upper and lower loss limit $\overline{L_{E,D,0.95}}$ and $\overline{L_{E,D,0.05}}$. The average includes the losses calculated with the distributions of the tested variances. Then the maximal risk of each event is defined by:

$$R_{L,E,\max} = P_E \cdot \overline{L_{E,0.95}} \tag{5.10}$$

and

$$R_{L,D,\max} = P_D \cdot \overline{L_{D,0.95}} \tag{5.11}$$

Keeping in mind that both risk $R_{L,E}$ and $R_{L,D}$ are equal, we now need to compare which of them includes the higher potential risk in case the duration of the hazard is larger than assumed initially. In order to determine the chance of risk reduction due to a fast recovery one can calculate the minimum risk by:

$$R_{L,E,\min} = P_E \cdot \overline{L_{E,0.05}} \tag{5.12}$$

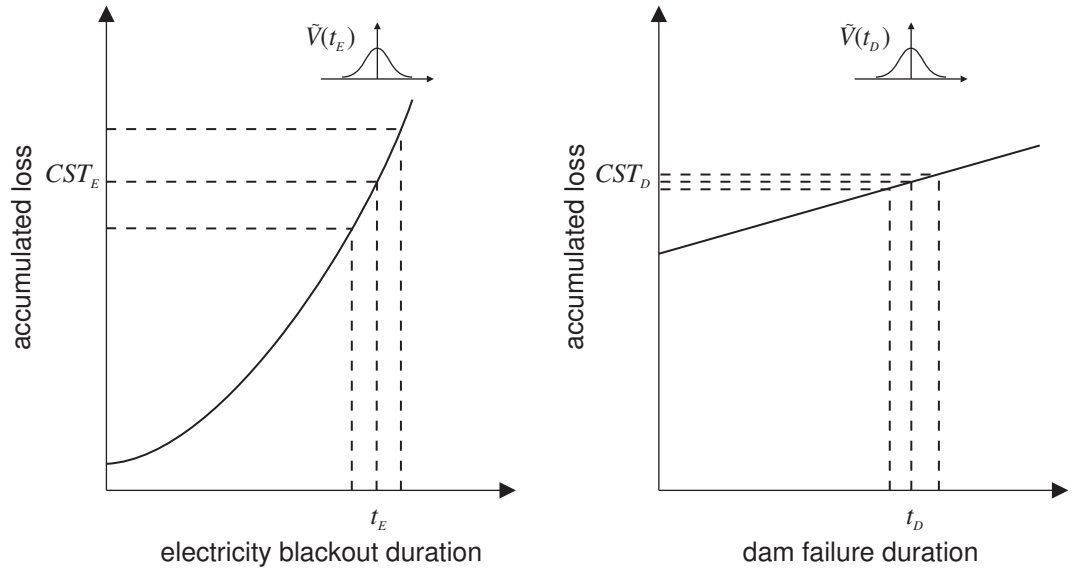

Figure 5.8: Cost due to an electricity blackout C_E and a dam failure C_D after a time interval t_E and t_D under variances in duration are $\tilde{V}(CST_E)$ and $\tilde{V}(CST_D)$ respectively.

and

$$R_{L,D,\min} = P_D \cdot \overline{L_{D,0.05}} \tag{5.13}$$

A measure to evaluate an enhanced disaster response can be defined as:

$$\Delta R_{L,E,D,\min} = R_{L,E,D} - R_{L,E,D,\min} \tag{5.14}$$

One can argue that the whole approach is fairly simple. However, it seems to be a reasonable approach to illustrate the complexity of risk management and the lack of information we may suffer, when risk is reduced to a single quantity.

Finally, we test our considerations with a simple example. All chosen parameters are an educated guess, considered to be sufficient to highlight the problem. Assuming a return period of an extensive blackout of 100 years and 1000 years for a major dam failure leads to $P_E = 10^{-2}$ and $P_E = 10^{-3}$. The cost functions which determine the losses for both events are defined as:

$$CST_E(t_E) = 10^5 \cdot e^{0.06908 \cdot t_E} \tag{5.15}$$

and

$$CST_D(t_D) = 10^6 \cdot t_D + 9 \cdot 10^8 \tag{5.16}$$

They are developed in order to result in the same magnitude of risk for t_E equals 100 hours and t_D equals to 100 weeks. The first means an electricity outage of about four days and the second leads to a time interval of almost two years to establish the state before the dam failure.

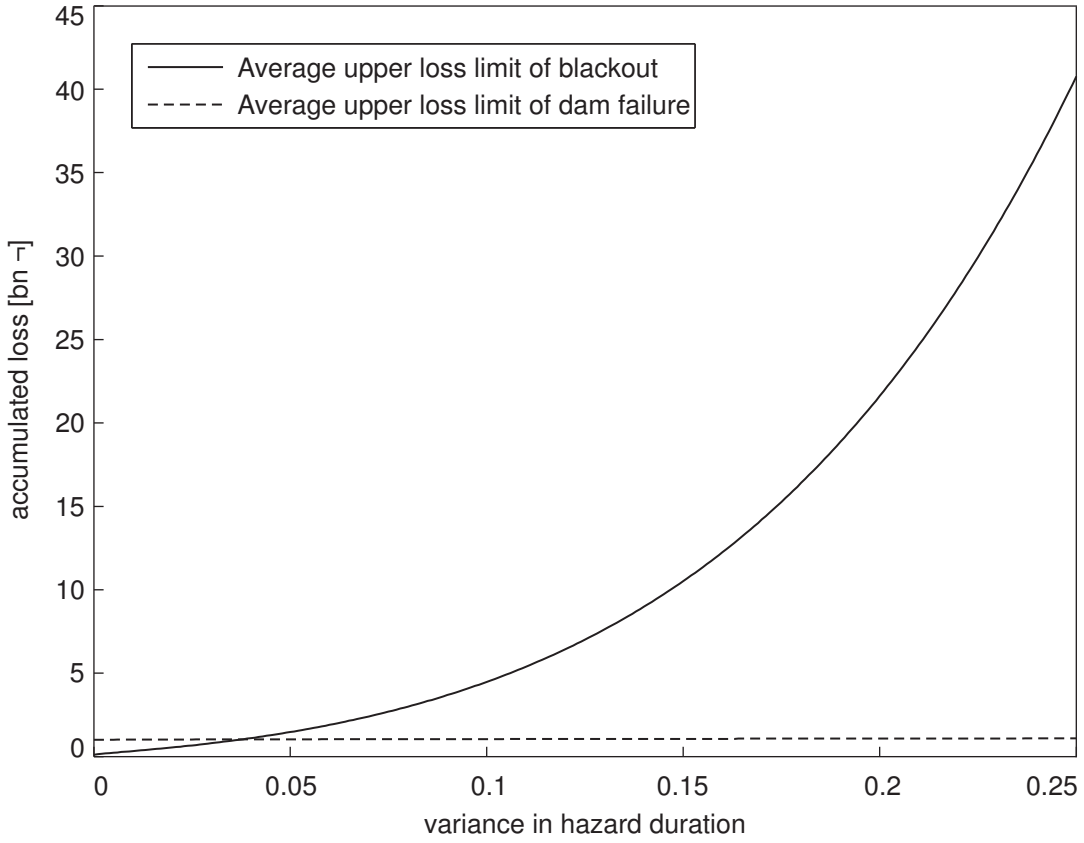

Figure 5.9: Average upper loss limit of blackout $(-)$ and dam failure (- - -) with respect to the variance in relative time deviation.

A relative time deviation ranging from $-80\,\%$ to $+80\,\%$ is chosen as reasonable guess. Hence, the variance of the centered normal distributed relative time deviation is tested in steps of 0.001 over an interval $\tilde{V}\left(CST_E\right) \in [0, 0.25]$ and $\tilde{V}\left(CST_D\right) \in [0, 0.25]$.

In our scenario the risk of both events is one million Euro per annum. This is the consequence of the assumptions we have made. We consider a blackout causing monetary losses of 100 million Euro with an occurrence probability of 10^{-2} per year and a dam failure that accumulates losses of one billion Euro with an occurrence probability of 10^{-3} per year.

Considering the time deviation the maximal risk $R_{L,E,\max}$ exceeds 113 million Euro per annum for electricity outage. Thus, the average of a delayed recovery in a range of 0 to $80\,\%$ increases the risk by a factor of 113. The effect on a dam failure is negligible compared to that. The risk $R_{L,D,\max}$ is only 58 thousand Euro per annum larger than the risk without considering a delay.

The average lower limit of losses due to a faster recovery of up to $80\,\%$ leads to minimum risks of $R_{L,E,\min}$ equal to 56 thousand and $R_{L,D,\min}$ equals 942 thousand Euro per annum. This means that the benefit of a fast recovery is significantly smaller for the dam failure than for the blackout.

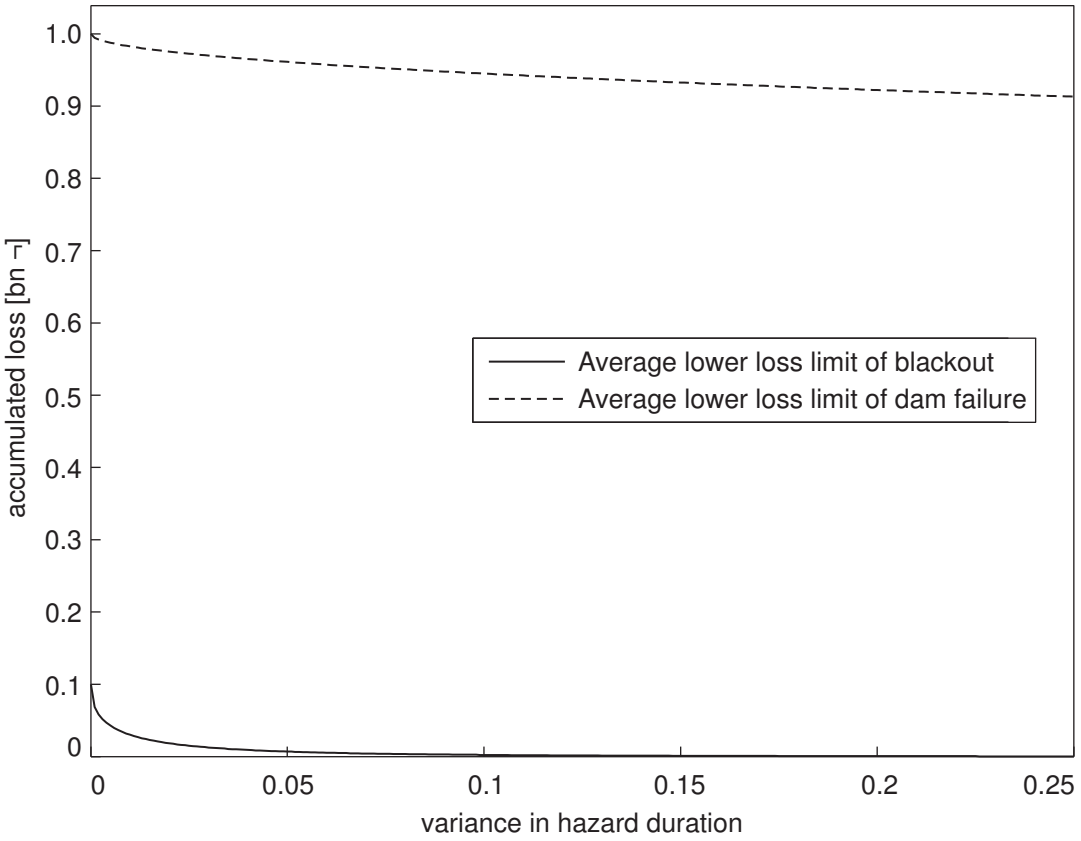

Figure 5.10: Average lower loss limit of blackout $(-)$ and dam failure (- - -) with respect to the variance in relative time deviation.

The risk reduction for a blackout $\Delta R_{L,E,\min}$ is 944 thousand Euro per annum and for a dam failure $\Delta R_{L,D,\min}$ it is equal to 58 thousand Euro per annum. Consequently, a faster recovery in a range of 0 to 80 % would safe on average 944 thousand or respectively 58 thousand Euro per annum. Hence, on the one hand, it would be reasonable to invest, for example, 900 thousand Euro per annum in the power network to decrease the expected losses to the average lower limit of the current state. On the other hand, investing only up to 58 thousand Euro per annum would be reasonable to improve the response to dam failure. In other words, when a blackout occurs and recovery time increases we would face maximal monetary loss of 11.3 billion Euro for an extensive blackout instead of the expected 100 million Euro. A shorter recovery time would safe on average only 94 million Euro compared to the expected loss of 100 million Euro. For a dam failure the monetary loss increases or decreases by 58 million Euro, when a variation in recovery time is considered. Obviously this reasoning is based on a very simple approach.

Finally, a sensitivity analysis is preformed to illustrate the influence of the variance in relative time deviation on the loss. In figure 5.9 and 5.10 show the influence of the variance on upper and respectively lower loss limit of electricity outage and dam failure with respect to the variance in hazard duration.

Figure 5.10 reveals a significant increase in losses due to blackouts, if the hazard duration were to increase due to a variance in recovery time. As expected, dam failures do not show such characteristics. A relative delay in recovery would not lead to significant additional losses. A faster recovery would yield a loss reduction as shown in figure 5.10. Again, changes in hazard duration could have a less pronounced effect on losses due to dam failure. A relative reduction in recovery time almost linearly decreases the losses. Contrarily, losses due to blackouts could be significantly reduced b even a small reduction in recovery time. Not addressed, however, is the question how expensive an accelerated recovery would be, which obviously is important when evaluating possible mitigation strategies.

6 Conclusion

6.1 Summary

The work presented here examines the risk of winter storms on transmission lines. Therefore, a numerical model is developed to simulate ice formation on conductor bundles to learn more about atmospheric icing. Subsequently, risk aspects of blackouts are investigated and a concept is presented to compare consequences of power outages with those of other hazards.

Atmospheric icing of structures occurs when freezing raindrops, supercooled cloud droplets or snow flakes hit a structure. Icing can cause significant damage to electric power transmission networks, especially in combination with wind. Therefore, shape and density of ice forming on conductors are of major interest to estimate the risk of blackouts. Large amplitude oscillations at low frequencies, or also twisting due to asymmetrical icing of cables, can cause fatigue damages and in extreme events even the collapse of numerous towers and power lines. Growing energy demand of modern societies and increasing capacity utilisation lead to increasing application of conductor bundles. Furthermore, meteorological observations show that such tandem arrangements of cylinders have an effect on the icing process. The experimental investigation of a large number of different icing conditions is extremely expensive. Therefore, it is beneficial to simulate ice accretion numerically. Existing numerical icing models are restricted to single cables due to the assumptions made in the flow calculation.

To overcome this restriction a Finite Element (FE) model is used to compute an incompressible, two dimensional flow field around conductor bundles. Resolving the smallest turbulent scales of the flow is computationally costly. Therefore, time averaging of the flow variables with Reynolds Average Navier-Stokes (RANS) equations is used to compute the turbulent flow field. The Reynolds stresses generated by the time averaging procedure are modeled with the standard k-ε turbulence model.

The mixed flow of air and precipitation droplets is modelled as a one-way coupled multiphase flow. Any effects of the particles on the fluid flow are neglected. A Lagrangian approach is used to calculate the individual particle trajectories based on the flow field calculation. To compute the forces acting on the particles it is necessary to approximate the drag coefficient. Therefore, an approximation function is derived from experimental results. The particle trajectories provide the impinging location of the droplets on the cable or respectively on the ice surface. The mass flux of icing particles can be visualised as stream tubes reaching from

the undisturbed flow to the surface, limited by the computed droplet trajectories. Within each tube the particles stream from the undisturbed flow to the surface, where the evolution of the ice front is determined.

Icing conditions on the surface are defined by the heat balance. Ice forms either under dry or wet growing conditions. The heat balance on the ice surface is very important for wet icing conditions, because a liquid layer forms on the surface and the equilibrium of freezing and melting is very sensitive. Glaze ice forms under this condition. Wet snow accretion is also considered as wet ice growth, but here also the heat transfer within the deposit is important. Rime ice forms under dry growing conditions. Here the heat transfer within the system can be neglected, because the latent heat of the droplets released during freezing is dissipated without changing the state of the ice and the surface conditions, hence no liquid layer arises. The heat equation accounts for convective and conductive heat transfer in the fluid and for conductive heat transfer in the ice deposit and conductor. Radiation and the heat equilibrium at the freezing interface are modelled as boundary conditions. The convective heat transport from the surface into the fluid is modelled with thermal wall functions.

The accretion mass is derived directly from the heat balance, whereas the ice density is computed by empirical equations depending on surface temperature, particle size and impact speed. The model calculates ice accretion iteratively, accounting for geometrical changes due to ice deposit in the flow calculation.

The investigation showed the influence of wind velocity on shape and accumulated ice mass. As expected, with increasing velocity the deposits become more streamlined, the density increases and eventually mass accumulates faster on the conductor. The characteristics of ice deposits forming due to cloud droplets, freezing rain and wet snow that are observed in experiments and field observations are clearly visible in the simulated ice deposits. The simulation also supports the assumption that under dry growing conditions ice shape and density are only marginally affected by the surface temperature of the conductor.

Furthermore, the model can show the nature of heat transfer under different icing conditions. In case of rime ice formation on an energized conductor the heat dissipates from the area where ice grows fastest. When it stops growing due to a lack of precipitation the heat flux spreads from the centre of the conductor to the surface. Under wet ice growing conditions the surface of an ice deposit has a uniform temperature. This causes the temperature gradient within the ice to varying with the thickness of the accumulated ice. The uniform temperature at the ice surface is sustained by heat transport within the liquid water film on the surface.

Tandem arrangement of conductors can reduce or even prevent ice formation on downstream cylinders depending on wind velocity, particle size, conductor spacing and bundle geometry. Generally speaking, a generic bundle of two conductors with a spacing of 400 mm and a diameter of 40 mm shows little or no ice on a downstream cylinder when clouds with a MVD $< 35\,\mu$m cause ice accretion. With increasing droplet size this effect vanishes and for freezing rain with MVD $< 120\,\mu$m full ice accretion is also expected on downstream cylinders.

Finally, a risk management framework and its implications on electricity outages are presented. It confirms that monetary losses due to blackouts increase exponentially with time. Therefore, a basic approach is developed to evaluate variations in outage duration and to compare the risk of blackouts to other types of disasters.

The investigation shows that a relatively small increase in power outage duration can cause severe losses. In contrast, a longer recovery period of the same relative magnitude after a dam failure, for instance, causes only marginal additional losses. Therefore, hazard duration in case of blackouts is a sensitive parameter to evaluate their risk appropriately, without which essential information about the risk would be lost. Furthermore, this concept can also help to evaluate recovery strategies when a number of different objects are affected and to efficiently focus resourses.

6.2 Outlook

Further research on modelling ice accretion on transmission lines should consider some of the following aspects. The first items listed below can be realized by continuing the work presented here. They are followed by an enumeration of aspects requiring significant computational resources, new modelling approaches and experimental investigations. Follow-up research could start with:

- A transient flow computation allows for transient effects on the particle flux. Hence, particle motion could be considered that vanishes in a time-averaged flow calculation. Following a transient flow field a discrete particle approach would be beneficial, where the motion of each computed particle is considered to represent the behaviour of a larger number of particles. This requires modelling the spreading of the discrete particles when they impinge, which is not trivial.
- In order to avoid problems arising from coupling different software packages and model schemes it could help to transfer the ice growth model from a FD model into a FE code by implementing the ice growth model as finite element.
- Incorporating an approach to estimate shedding of ice deposits, because this determines the maximum ice load of the icing event. Thus, it is required for defining design loads.

However, further improvements of the numerical models require significant computational resources. Presuming they are available, the research should focus on:

- An LES approach can enhance the flow computation including advanced turbulence models. Furthermore, the turbulence model can be improved to allow for two-way coupling of airflow and precipitation.
- Conductor oscillation and twisting have an influence on ice formation. To allow for cable motion in the simulation of icing processes requires modelling of an interaction between

airflow and moving conductor. However, such a model is computationally demanding.

- Related to improvements in the flow calculation is three-dimensional modelling of flow field and ice growth. The latter can include effects of a rough ice surface as well as the formation of icicles or the inclined orientation of particle flux and transmission line. However, this would require significant computational resources.
- Multiphase flow phenomena, such as deformation and splashing of droplets, are an interesting research field, but their effect on the icing process is rather small and therefore of minor significance.

Moreover, there is no convincing modelling approach available sofar for some aspects of the ice accretion process such as:

- Modelling the melting of ice also contributes to the estimation of design loads. Such an approach could include heat transfer within wet snow to determine the fraction of liquid water and eventually the snow density.
- Three-dimensional modelling of a supercooled water film forming on the ice surface would be a very important improvement of ice accretion models. It would require extensive computational power.

Finally, further experimental and numerical studies could focus on:

- Other transmission line equipment should be examined such as insulators and transmission line towers.
- The investigation of mixed precipitation is already possible, but adequate reference data is missing to verify model results.
- More experimental data is required to better verify ice accretion models.

Research on risk assessment of blackouts could continue with the approach presented here. The influence of the variance in hazard duration in risk assessment could be examined by the following aspects:

- Application on data of past events could help to evaluate the basic approach.
- Examination of periodic events could be worthwhile, when recovery strategies are executed differently from one occurrence to another.
- Improving the stochastic tools of the approach.

I would like to conclude by wishing colleagues who decide to work in one of the aforementioned fields a successful and interesting research time.

Bibliography

[1] ACHENBACH, E.: The effect of surface roughness on the heat transfer from a circular cylinder to the cross flow of air. in: *International Journal of Heat and Mass Transfer* 20 (1977), pp. 359-369

[2] ADMIRAT, P.: Wet Snow Accretion on Overhead Lines. in: FARZANEH, M. (ed.): *Atmospheric Icing of Power Networks*. Springer, 2008, pp. 119-170

[3] ADMIRAT, P. ; MACCAGNAN, M. ; DEGONCOURT, B.: Influence of Joule effect and climatic conditions on liquid water content of snow accreted on condators. in: *4th International Workshop on Atmospheric Icing of Structures*, 1988, pp. 367-371

[4] BAIN, M ; GAYET, J. F.: Contribution to the modeling of the ice accretion process: Ice density variation with the impact surface angle. in: *Annals of Glaciology* 4 (1982), pp. 19-23

[5] BARBER, S. ; WANG, Y. ; CHOKANI, N. ; ABHARI, R. S.: The effect of ice shapes on wind turbine performance. in: *13th International Workshop on Atmospheric Icing of Structures*, 2009

[6] BENDEL, W. B. ; PATON, D.: A review on the effect of ice storms on the power industry. in: *Journal of Applied Meteorology* 20 (1981), pp. 1445-1449

[7] BEST, A. C.: The size distribution of raindrops. in: *Quarterly Journal of the Royal Meteorological Society* 76 (1951), pp. 16-36

[8] BEYER, B. M. W. M. Waechter: Modeling transient snowdrift development around complex three-dimensional structures. in: *Journal of Wind Engineering and Industrial Aerodynamics* 96 (2008), pp. 1603-1615

[9] BINTANJA, R.: Snowdrift suspension and atmospheric turbulence. Part I: Theoretical backround and model description. in: *Boundary-Layer Meteorology* 95 (2000), pp. 343-368

[10] BRUYN, J. R.: On the formation of periodic arrays of icicles. in: *Cold Regions Science and Technology* 25 (1997), pp. 225-229

[11] BUNDESAMT FÜR BEVÖLKERUNGSSCHUTZ UND KATASTROPHENHILFE (BBK): *Zusammenfassung der Katastrophenübung LÜKEX 2004*. 2006. – [in German, classified]

[12] BUNDESNETZAGENTUR: *Untersuchungsbericht über die Versorgungsstörung im Net-*

zgebiet des RWE im Münsterland vom 25.11.2005. Bundesnetzagentur für Elektrizität, Gas, Untersuchungsbericht Telekommunikation Post und Eisenbahnen, Bonn, 2006

[13] BUNDESNETZAGENTUR FÜR ELEKTRIZITÄT, GAS, UNTERSUCHUNGSBERICHT TELEKOMMUNIKATION POST UND EISENBAHNEN: Über die Versorgungsstörung im Netzgebiet des RWE im Münsterland vom 25.11.2005. 2006. – [in German]

[14] CANTWELL, B. ; COLES, D.: An experimental study of entrainment and transport in the turbulent near wake of a circular cylinder. in: *Journal of Fluid Mechanics* 136 (1983), pp. 321-374

[15] CASPAR, W. ; SANDRECZKI, A: Eisablagerungen aus meteorologischer Sicht. in: *Elektrotechnische Zeitschrift* 16(26) (1964), pp. 763-767. – [in German]

[16] `http://www.cfd-online.com/Wiki/Reference_section`

[17] CHABART, O. ; LILIEN, J. L.: Galloping of Electrical Lines in Wind Tunnel Facilities. in: *Journal of Wind Engineering and Industrial Aerodynamics* 74-76 (1998), pp. 967-976

[18] CLIFT, R. ; GRACE, J. R. ; WEBER, M. E. ; JOVANOVICH, Hacourt B. (ed.): *Bubbles, Dropls and Particles*. Academic Press, 1978

[19] CLOBES, M. ; WILLECKE, A. ; PEIL, U.: Eine vereinfachtes Lastmodell für abgespannte Maste in böigem Wind. in: *VDI-Bericht Nr. 2063*, 2009

[20] COMSOL MULTIPHYSICS AB (ed.): *COMSOL 3.5 User's Guid*. COMSOL Multiphysics AB, 2009

[21] CROWE, T. C. ; MICHAELIDES, E. E.: Basic Concepts and Definitions. in: CROWE, T. C. (ed.): *Multiphase Flow Handbook*. CRC Press Inc. Taylor & Francis Group, 2006 (1), pp. 1-78

[22] DEN HARTOG, J. P.: Transmission line vibration due to sleet. in: *Transactions A. I. E. E.* 1 (1932), pp. 1074-1086

[23] DIEM, M.: Höchstlasten der Nebelfrostablagerungen an Hochspannungsleitungen. in: *Archiv für Meteorologie, Geophysik und Bioklimatologie* B7 (1955), pp. 87-95. – [in German]

[24] DIN 1055: Einwirkungen auf Tragwerke - Teil 5: Schnee- und Eislasten / DIN Deutsches Institut für Normung e.V., Beuth Verlag GmbH, Berlin. 2005. – [in German]

[25] DJERIDI, H. ; BRAZA, M. ; PERRIN, R. ; HARRAN, G. ; CID, E. ; CAZIN, S.: Near wake turbulence properties around a circular clinder at high Reynolds numbers. in: *Flow, Turbulences and Combustion* 71 (2003), pp. 19-34

[26] DORMAND, J. R. ; PRINCE, P. J.: A familiy of embedded Runge-Kutta formulae. in: *Journal of Computational and Applied Mathematics* 6(1) (1980), pp. 19-26

[27] EC1 DIN EN-1991, TEIL 1-3: Allgemeine Einwirkungen, Schneelasten / DIN Deutsches Institut für Normung e.V., Beuth Verlag GmbH, Berlin. 2005. – [in German]

[28] FARZANEH, M. ; CHISHOLM, A.: Effects of Ice and Snow on the Electrical Preformance of Power Network Insulators. in: FARZANEH, M. (ed.): *Atmospheric Icing of Power Networks*. Springer, 2008, pp. 269-326

[29] FARZANEH, M. ; VOLAT, C. ; LEBLOND, A.: Anti-icing and De-icing Techniques for Overhead Lines. in: FARZANEH, M. (ed.): *Atmospheric Icing of Power Networks*. Springer, 2008, pp. 229-265

[30] FEKR, M. R. ; MCCLURE, G. ; HARTMANN, D.: Investigation of transmission line failure due to ice shedding effects using dynamic analysis. in: *8th International Workshop on Atmospheric Icing of Structures*, 1998

[31] FERZIGER, J. H. ; MILOVAN, P.: *Numerische Strömungsmechanik*. Springer, 2008. – [in German]

[32] FINSTAD, K. J. ; LOZOWSKI, E. P.: On the medium volum diameter approximation. in: *Journal of Atmospheric Science* 45 (1988), pp. 4008-4012

[33] FINSTAD, K. J. ; LOZOWSKI, E. P. ; E. M. GATES, E. M.: A computational investigation of water droplet trajectories. in: *J. Atmos. Oceanic Technol.* 5 (1988), pp. 160-170

[34] FRANKE, J.: *Introduction to the prediction of wind effects on buildings by computational wind engineering (CWE) in Wind Effects on Buildings and Design of Wind-Sensitive Structures*. Springer, 2007

[35] FU, P.: *Modelling and simulation of the ice accretion process on fixed or rotating cylindrical objects by boundary element method*, University of Quebec, PhD thesis, 2004

[36] FU, P. ; FARZANEH, M.: Numerical modeling of snow accretion over a cable span. in: *12th International Workshop on Atmospheric Icing of Structures*, 2007

[37] FU, Ping ; FARZANEH, Masoud ; BOUCHARD, Gilles: Two-dimensional modelling of the ice accretion process on transmission line wires and conductors. in: *Cold Regions Science and Technology* 46 (2006), pp. 132-146

[38] FUCHS, L. ; SZASZ, R-Z.: Ice accretion on wind-turbines. in: *13th International Workshop on Atmospheric Icing*, 2009

[39] GATES, E. M. ; LIU, A. ; LOZOWSKI, E. P.: A stochastic model of atmospheric rime icing. in: *Journal of Glaciology* 34 (1988), pp. 26-30

[40] GOODWIN, E. J.: Predicting ice and snow loads for transmission lines. in: *1st International Workshop on Atmospheric Icing of Structures*, 1983, pp. 267-273

[41] GRENIER, J. C. ; ADMIRAT, P. ; MACCAGNAN, M.: Theory and modelling in the growth of wet snow sleeves. in: *EDF:EDF/DER/ERMEL/TA/HM/ 25288 Technical Report* 8 (1985), pp. 68

[42] HARDY, C. ; VAN DYKE, P.: Field observations on wind-induced conductor motions. in: *Journal of Fluids and Structures* 9 (1995), pp. 43-60

[43] HESSE, K.: The management of the devastating ice storms. in: *3rd International Workshop on Atmospheric Icing of Structures*, 1988

[44] HITSCHFELD, W. ; RIGBY, E. C. ; MARSHALL, S. J.: The development of the size distribution of raindrops during their fall. in: *Journal of Meteorology* 11 (1954), pp. 362-372

[45] IMAI, I.: Studies on ice accretion. in: *Research on Snow and Ice* 1 (1953), pp. 35-44

[46] IQBAL, M.: *An introduction in solar radiation*. Academic Press Canada, 1983

[47] ISO 12494: Atmospheric icing of structures / American National Standards Institute (ANSI). 2001

[48] JONES, K. F.: An Evaluation of the Severity of the January 1998 Ice Storm in Northern New England / Report for FEMA Region 1. 1998

[49] JONES, K. F.: A simple model for freezing rain ice loads. in: *Atmospheric Research* 46 (1998), pp. 87-97

[50] JONES, K. F. ; PEABODY, A. B.: The application of a unifom radial ice thickness to structural sections. in: *Cold Regions Science and Technology* 44 (2006), pp. 145-148

[51] KARIUKI, K. K. ; ALLAN, R. N.: Applications of customer outage costs in system planning, design and operation. in: *IEE Proceedings - Generation, Transmission and Distribution* vol. 143, 1996, pp. 305-312

[52] KARTSCHALL, K. ; PIEHL, H. D.: Eisablagerungen / Klimadaten der Deutschen Demokratischen Republik. 1988 (11). – [in German]

[53] KAYS, W. M.: Turbulent Prandtl Number - where are we? in: *Journal of Heat Transfer* 116 (1994), pp. 284-295

[54] KAYS, W. M. ; CRAWFORD, M. E.: *Convective Heat and Mass Transfer*. McGraw-Hill, 1993

[55] KIESSLING, F. ; NEFZIGER, P. ; KAINTZYK, U.: *Freileitungen: Planung, Berechnung, Ausführung*. Springer, 2001. – [in German]

[56] KIESSLING, F. ; NEFZGER, P. ; NOLASCO, J. F. ; KAINTZYK, U.: *Overhead Power Lines - Planing, Design, Construction, Power Systems*. Springer, 2003. – 321-348 S.

[57] KIRCH, A. ; PEIL, U.: Berechnung der Flatterwindgeschwindigkeit zweidimensionaler Modelle aeroelastischer Systeme — Untersuchungen zu Näherungsformeln / Interner Bericht des Instituts für Stahlbau an der TU-Braunschweig. 2010. – [in German]

[58] KNUDDSEN, J. G. ; KATZ, D. L.: *Fluid dynamics and heat transfer*. McGraw-Hill, 1958

[59] KOLLAR, E. L. ; FARZANEH, M.: Modeling the evolution of droplet size distribution in two-phase flows. in: *International Journal of Multiphase Flow* 33 (2007), pp. 1255-1270

[60] KOLLAR, E. L. ; FARZANEH, M. ; KAREV, A. R.: Modeling droplet collision and coalescence in an icing wind tunnel and the influence of these processes on droplet size distribution. in: *International Journal of Multiphase Flow* 31 (2005), pp. 69-92

[61] KOLLAR, L. ; FARZANEH, M.: Wind-tunnel investigation of icing of an inclined cylinder. in: *International Journal of Heat and Mass Transfer* 53 (2010), pp. 849-861

[62] KOLLAR, L. E. ; FARZANEH, M.: The effects of droplet collision, evaporation, gravity and turbulent dispersion on the droplet size distribution of an aerosol cloud under icing conditions. in: *12th International Workshop on Atmospheric Icing of Structures*, 2007

[63] KÜSSNER, H. G. ; SCHWARZ, L.: Der schwingende Flügel mit aerodynamisch ausgeglichenem Ruder. in: *Luftfahrtforschung* 17 (1940), pp. 337-354. – [in German]

[64] LACASSE, D. ; TURGEON, E. ; PELLETIER, D.: On the judicious use of the k-ε model, wall function and adaptivity. in: *International Journal of Thermal Sciences* 43 (2004), pp. 925-938

[65] LAFORTE, C. ; BEISSWENGER, A.: Icephobic material centrifuge adhesion test. in: *11th International Workshop on Atmospheric Icing of Structures*, 2005

[66] LANGMUIR, I. ; BLODGETT, K.B.: A Mathematical Investigation of Water Droplet Trajectories / AAF Technical Report 5418. 1946

[67] LARCOMBE, P. J. ; POOTS, G. ; SKELTON, P. L. I. ; SHILLOR, M.: Mathematical models for ice accretion on conductors using free streamline theory Part I: Single conductor. in: *IMA Journal of Applied Mathematics* 41 (1988), pp. 217-236

[68] LENGGENHAGER, K.: Über wellige, stumpfe, glatte und spitze Eiszapfen. 1. Wellige und Stumpfe Eiszapfen. in: *Zeitschrift für Meterologie* 28(5) (1978), pp. 292-197. – [in German]

[69] LENHARD, R. W.: An indirect method for estimating the weight of glaze on wires. in: *Bulletin of the American Meteorologic Society* 36 (1955), pp. 1-5

[70] LLINCA, A. ; LLINCA, F. ; IGNAT, I.: Numerical study of iced conductors aerodynamics. in: *7th International Workshop on Atmospheric Icing of Structures*, 1996

[71] LOZOWSKI, E. P. ; STALLABRASS, J. R. ; HEARTY, P. F.: The icing of an unheated, nonrotationg cylinder. Part I. A simulation model. in: *Journal of Climate and Applied Meteorology* 22 (1983), pp. 2053-2061

[72] MACKLIN, W. C.: The density and structure of ice formed by accretion. in: *Quarterly Journal of the Royal Meteorological Society* 88 (1962), pp. 30-50

[73] MAENO, N. ; MAKKONEN, L. ; NISHIMURA, K. ; KOSUGI, K. ; TAKAHASHI, T.: Growth rates of icicles. in: *Journal of Glaciology* 40 (1994), pp. 319-326

[74] MAENO, N. ; TAKAHASHI, T.: Studies on icicles. I. General aspects of the structure and growth of an icicle. in: *Low Temperature Science* 43 (1984), pp. 125-138

[75] MAENO, N. ; TAKAHASHI, T.: Studies on icicles. I. Wave- forms, spikes and bent icicles general aspects of the structure and growth of an icicle. in: *Low Temperature Science* 43 (1984), pp. 139-147

[76] MAKKONEN, L.: Estimating intensity of atmospheric ice accretion on stationary strucutres. in: *Journal of Applied Meteorology* 20 (1981), pp. 595-600

[77] MAKKONEN, L.: Modelling of ice accretion on wires. in: *Journal of Climate and Applied Meteorology* 23 (1984), pp. 929-939

[78] MAKKONEN, L.: Salinity and growth rate of ice formed by sea spray. in: *Cold Regions Science and Technology* 14 (1987), pp. 163-171

[79] MAKKONEN, L.: A model of icicle growth. in: *Journal of Glaciology* 34(116) (1988), pp. 1-7

[80] MAKKONEN, L.: Estimation of wet snow accretion on strucutres. in: *Cold Regions Science and Technology* 17 (1989), pp. 83-88

[81] MAKKONEN, L.: Modeling power line icing in freezing precipitation. in: *Atmospheric Research* 46 (1998), pp. 131-142

[82] MAKKONEN, L.: Models for the growth of rime, glaze, icicles and wet snow on structures. in: *Phil. Trans. R. Soc. London* 358 (2000), pp. 2913-2939

[83] MAKKONEN, L. ; AHTI, K.: Climatic mapping of ice loads based on airport weather observations. in: *Atmospheric Research* 36 (1995), pp. 185-193

[84] MAKKONEN, L. ; FUJII, Y.: Spacing of icicles. in: *Cold Regions Science and Technology* 21 (1993), pp. 317-322

[85] MAKKONEN, L. ; STALLABRASS, R. J.: The effect of roughness on the rate of ice accretion on a cylinder. in: *Annals of Glaciology* 6 (1985), pp. 142-145

[86] MAKKONEN, L. ; WICHURA, B.: Simulating wet snow loads on power line cables by a simple model. in: *Cold Regions Science and Technology* 61 (2010), pp. 73-81

[87] MANHART, M. ; PELLER, N. ; BRUN, C.: Near-wall scaling for turbulent boundary layers with adverse pressure gradient. in: *Theoretical and Computational Fluid Dynamics* 22 (2008), No. 3, pp. 243-260

[88] MARSHALL, S. J.: Precipitation trajectories and patterns. in: *Journal of Meteorology* 10 (1953), pp. 25-29

[89] MARSHALL, S. J. ; PALMER, McK. W.: The distribution of raindrops with size. in: *Journal of Meteorology* 5 (1948), pp. 165-166

[90] MARSHALL, S. J. ; PALMER, McK. W. ; LANGILLE, C. R.: Measurement of rainfall by radar. in: *Journal of Meteorology* 4 (1947), pp. 186-192

[91] MASON, B. L.: *Clouds, Rain and Rainmaking*. Cambridge University Press., 1962

[92] MATHWORKS (ed.): *MATLAB R2009a*. MathWorks, 2009

[93] MCCOMBER, P.: Numerical simulation of cable twisting due to icing. in: *Cold Regions Science and Technology* 8 (1984), pp. 253-259

[94] MCCOMBER, P. ; DRUEZ, J. ; LAFLAMME, J.: A comparison of selected models for estimating cable icing. in: *Atmospheric Research* 36 (1995), pp. 207-220

[95] MCCOMBER, P. ; MORIN, G. ; MARTIN, R. ; VAN, L. V.: Estimation of combined ice and wind load on overhead transmission lines. in: *Cold Regions Science and Technology* 6 (1983), pp. 195-206

[96] MCCOMBER, P. ; PARADIS, A.: A cable galloping model for thin ice accretions. in: *Atmospheric Research* 46 (1998), pp. 13-25

[97] MELLOR, M. ; MELLOR, A.: Some characteristics of falling snow. in: *Cold Regions Science and Technology* 15 (1988), pp. 201-206

[98] MESSINGER, B. L.: Equilibrium temperature of an unheated icing surface as a function of air speed. in: *Journal of the Aeronautical Sciences* 20 (1953), pp. 29-41

[99] MEYERS, T. G. ; CHARPIN, J. P. F.: A mathematical model for atmospheric ice accretion and water flow on a cold surface. in: *International Journal of Heat and Mass Transfer* 47 (2004), pp. 5483-5500

[100] MEYERS, T. G. ; CHARPIN, J.P.F. ; CHAPMAN, S.J.: *The flow and solidification of a thin fluid film on an arbitrary three-dimensional surface*, 2007

[101] MILI, L ; QUI, Q. ; PHADKE, A. G.: Risk assessment of catastrophic failures in electric power systems. in: *International Journal of Critical Infrastructures* 1 (2004), pp. 38-63

[102] MIRI, A. M. ; SCHWAB, A. J. ; BÜCHE, R.: Modellbildung winderregter Leiterseilschwingungen großer Amplitude. in: *Elektrizitätswirtschaft* 6 (1989), pp. 307-315. – [in German]

[103] MITTEN, P. T. ; MAKKONEN, L. ; MORRIS, R. J.: Development of an perational ice and wind loading model for transmission lines. in: *Canadian Electrical Association (CEA) Conference*, 1988

[104] MUHLERIN, N. D.: Atmospheric icing and communication tower failure in the United States. in: *Cold Regions Science and Technology* 27 (1998), pp. 91-104

[105] NAKAMURA, Y.: Galloping of bundled power line conductors. in: *Journal of Sound and Vibration* 73(3) (1980), pp. 363-377

[106] NATERER, G. F.: Multiphase flow with impinging droplets and airstream interaction at a moving gas/solid interface. in: *International Journal of Multiphase Flow* 28 (2002), pp. 251-477

[107] NATERER, G. F.: Coupled liquid film and solidified layer growth with impinging

supercooled droplets and Joule heating. in: *International Journal of Heat and Fluid Flow* 24 (2003), pp. 223-235

[108] NIGOL, O. ; CLARK, G. J. ; HAVARD, D. G.: Torsional stability of bundle conductors. in: *IEEE Paper* F 77 (1977), pp. 224-229

[109] NOVAK, M. ; DAVENPORT, A. G. ; TANAKA, H.: Vibration of towers due to galloping of iced cables. in: *Journal of the Engineering Mechanics Devision* 1 (1978), pp. 457-472

[110] OTTA, S.P. ; ROTHMAYER, A.P.: Instability of stagnation line icing. in: *Computers & Fluids* 38 (2009), pp. 273-283

[111] PEIL, U. ; NÖLLE, H.: Zur Auswirkung von Vereisung auf die Beanspruchung abgespannter Masten. in: *Bauingenieur* 68 (1993), pp. 237-245. – [in German]

[112] PEIL, U. ; RUFF, D.: Seile unter Eislast - Risiken und Reaktionen. in: *1st International Cable Structure Symposium Cable Structure Symposium*, 2005

[113] PETRENKO, V. F. ; PENG, S.: Reduction of ice adhesion to metal by using self-assembling mono-layers (SAMs). in: *Canadian Journal of Physics* 81 (2003), pp. 387-393

[114] PETROVIC, J. J.: Mechanical properties of ice and snow. in: *Journal of Material Science* 38 (2003), pp. 1-6

[115] PHAN, C. L. ; LAFORTE, J.-L.: The influence of electro-freezing on the ice formatuion on high-voltage DC trandmission lines. in: *Cold Regions Science and Technology* 4 (1981), pp. 1525

[116] PIEHL, H. D.: Zum Problem der orographischen Unterschiede der Nebelfrostgefährdung / Abhandlungen des Meteorologischen Dienstes der DDR. 1973 (107(14): pp. 20-25). – [in German]

[117] POOTS, G. ; KENDALL, P. C. (ed.): *Ice and Snow Accretion on Structures*. Research Studies Press LTD., 1996

[118] POOTS, G. ; SKELTON, P. L. I.: Further aspects of dynamical models for rime-ice and snow accretion on an overhead line conductor. in: *International Journal for Numerical Methods in Engineering* 37 (1994), pp. 1863-1880

[119] POOTS, G. ; SKELTON, P. L. I.: The effects of aerodynamic torque on the rotation of an overhead line conductor of finite torsional stiffness: snowload, liquid water content and snow shedding. in: *Atmospheric Research* 36 (1995), pp. 251-260

[120] POOTS, G. ; SKELTON, P. L. I.: A numerical study of mechanisms of accretion for rotating snow sleeves evolving on conductor rods. in: *International Journal for Numerical Methods in engineering* 38 (1995), pp. 861-879

[121] POOTS, G. ; SKELTON, P. L. I.: Simulation of wet-snow accretion by axial growth on a transmission line conductor. in: *Applied Mathematical Modelling* 19 (1995), pp. 514-518

[122] POOTS, G. ; SKELTON, P. L. I.: Thermodynamic models of wet-snow accretion: axial growth and liquid water content on a fixed conductor. in: *International Journal of Heat and Fluid Flow* 16 (1995), pp. 43-49

[123] RAWLINS, C. B.: Wake-Induced Oscillation. in: *Transmission Line Reference Book - Wind Induced Conductor Motion*. EPRI, Palo Alto, CA, U.S.A, 1979

[124] RIERA, J. D. ; OLIVEIRA, T.T.: Wind-strucutre interaction in conductor bundles in transmission lines. in: *Structure and Infrastructure Engineering* 6: 4 (2010), pp. 435-446

[125] ROBERGE, M. ; FARZANEH, M. ; MCCLURE, G. ; PEYRARD, C.: Wet Snow Shedding from an Overhead Cable Part 1: Experimental Study. in: *12th International Workshop on Atmospheric Icing of Structures*, 2007

[126] ROBERGE, M. ; MCCLURE, G. ; FARZANEH, M. ; PELLET, L.: Wet Snow Shedding from an Overhead Cable Part 2: Evaluating the Dynamic Response of a Cable Subjected to Wet Snow Shedding. in: *12th International Workshop on Atmospheric Icing of Structures*, 2007

[127] SADOV, S. Y. ; SHIVAKUMAR, P. N. ; FIRSOV, D. ; LUI, S. H. ; THULASIRAM, R.: Mathematical model of ice melting on transmission lines. in: *Journal of Mathematical Modelling and Algorithms* 6 (2007), pp. 273-286

[128] SCHENK, O. ; GÄRTNER, K.: Solving unsymmetric sparse systems of linear equations with PARDISO. in: *Future Generation Computer Systems* 20 (2004), pp. 475-487

[129] SCHENK, O. ; GÄRTNER, K.: On fast factorization pivoting for sparse symmetric indefinite systems. in: *Electronic Transactions on Numerical Analysis* 23 (2006), pp. 158-179

[130] SCHÄFER, M. ; TUREK, S.: Benchmark Computations of Laminar Flow Around a Cylinder. in: HIRSCHEL, E.H. (ed.): *Flow Simulation with High-Performance Computers* vol. 52. Vieweg, 1996, pp. 547-566

[131] SCHLICHTING, H. ; GERSTEN, K.: *Grenzschicht-Theorie*. Springer, 2006. – [in German]

[132] SCHWAB, A. J. ; MIRI, A. M. ; BÜCHE, R.: Über den Mechanismus des Seiltanzens und Maßnahmen zu seiner Unterdrückung. in: *Elektrizitätswirtschaft* 23 (1990), pp. 1316-1322. – [in German]

[133] SHAO, J. ; LAUX, S. J. ; TRAINOR, B. J. ; PETTIFER, R. E. W.: Nowcasts of temperature and ice on overhead railway transmission wires. in: *Meteorological Application* 10 (2003), pp. 123-133

[134] SIMIU, E. ; COOK, G. R.: Chaotic motion of self-excited forced and autonomous square prisms. in: *Journal of Engineering Mechanics* 117 (1991), pp. 241-259

[135] SIMIU, E. ; SCANLAN, R. H.: *Wind Effects on Structures: Fundamentals and Applications to Designe*. New York : Wiley, 1996

[136] SKELTON, P. L. I. ; POOTS, G.: Approximated prediction of ice accretion along conductors of finite torsional stiffness and control of rotation using counterweights. in: *International Journal of Numerical Methods in Engineering* 30 (1990), pp. 965-980

[137] SKELTON, P. L. I. ; POOTS, G.: A dynamical model for rime-ice accretion of an overhead transmission line of finite trosional stiffness. in: *Mathematics in Engineering Industry* 3 (1990), pp. 1-24

[138] SKELTON, P. L. I. ; POOTS, G.: Snow accretion on overhead line conductors of finite torsional stiffness. in: *Cold Regions Science and Technology* 19 (1991), pp. 301-316

[139] SOCKEL, H.: *Aerodynamik der Bauwerke*. Vieweg, 1984. – [in German]

[140] SOLMO, B. ; GUPTA, V.: A hydrophobic self-assembled monolayer with improved adhesion to aluminium for de-icing application. in: *Journal of Mechanical Behaviour of Materials* 33 (2001), pp. 471-480

[141] SPARROW, E. M. ; STRETTON, A. J.: Natural convection from variously orientaed cubes and from other bodies of unit aspect ratio. in: *International Journal of Heat and Mass Transfer* 28(4) (1985), pp. 741-752

[142] SPIEGEL: Unternehmer verlieren über 100 Millionen Euro. (2005), 29.11. `http://www.spiegel.de/wirtschaft/0,1518,387579,00.html`. – [in German]

[143] SPIEGEL, L. ; BIRKINSHAW, K. ; KUKULKA, R. ; THERKELSEN, R. L.: The cost of wildlife-caused power outage to California's economy / California Energy Commission. 2005 (CEC-500-2005-030). – PIER

[144] STOFFEL, M.: *Numerical Modelling of Snow using Finite Elements*, ETH Zürich, PhD thesis, 2006

[145] SUNDIN, E. ; MAKKONEN, L.: Ice loads on a lattice tower estimated by weather station data. in: *Journal of Applied Meteorology* 37 (1998), pp. 523-529

[146] SZILDER, K. ; LOZOWSKI, E. P.: Simulation of icicle growth using a threedimensional random walk model. in: *Atmospheric Research* 36 (1995), pp. 243-249

[147] SZILDER, K. ; LOZOWSKI, E. P.: Novel two-dimensional modeling approach for aircraft icing. in: *Journal of Aircraft* 41(4) (2004), pp. 854-861

[148] SZILDER, K. ; LOZOWSKI, E. P. ; GATES, E. M.: Modelling ice accretion on non-totating cylinders - the incorporation of time dependeces and internal heat conduction. in: *Cold Regions Science and Technology* 13 (1987), pp. 177-191

[149] SZILDER, K. ; WASLIWAZ, M. ; LOZOWSKI, E. P.: Measurement of average convective heat transfer coefficient and drag coefficient for icing shape cylinders. in: *4th International Workshop on Atmospheric Icing of Structures*, 1988, pp. 147-151

[150] TOMBOULIDES, A. G. ; ORSZAG, S. A.: Numerical investigation of transitional and weak turbulent flow past a sphere. in: *Journal of Fluid Mechanics* 416 (2000), pp. 45-73

[151] TRAVIN, A. ; SHUR, M. ; STRELETS, M. ; SPALART, P.: Detached-eddy simulation past a circular cylinder. in: *Flow, Turbulence and Combustion* 63 (1999), pp. 293-313

[152] UENO, K. ; FARZANEH, M.: The effect of airflow on the wavelength of ripples on icicles. in: *13th International Workshop on Atmospheric Icing of Structures*, 2009

[153] URBAN, M.: *Earthquake Risk Assessment of Historical Structures*, TU Braunschweig, GRK802: Graduate School for Risk Management of Natural Hazards, PhD thesis, 2007

[154] VAN DYKE, P. ; HAVARD, D. ; LANEVILLE, A.: Effect of Ice and Snow on the Dynamics of Transmission Line Conductors. in: FARZANEH, M. (ed.): *Atmospheric Icing of Power Networks*. Springer, 2008, pp. 171-225

[155] VANKO, V. I.: The aerodynamical instability of circular profiles systems. in: *Physics and Control, 2005. Proceedings. 2005 International Conference*, 2005, pp. 202- 205

[156] WACKER, G. ; BILLINTON, R.: Customer cost of electric service interruptions. in: *IEE Proceedings* vol. 77, 1989, pp. 919-930

[157] WAGNER, T. ; PEIL, U.: Atmospheric icing of transmission line conductor bundles. in: *2nd Europian COMSOL Conference 2008*. Göttingen, Germany, November 2008

[158] WAGNER, T. ; PEIL, U.: A numerical model for atmospheric icing of conductor bundles. in: *13th International Workshop on Atmospheric Icing of Structures*. Andermatt, Swiss, September 2009

[159] WAGNER, T. ; PEIL, U.: Vereisung von Hochspannungsleitungen. in: *WtG-Berichte Nr. 11 - Windingenieurwesen in Forschung und Praxis*. Braunschweig, Germany, November 2009, pp. 203-214. – [in German]

[160] WAGNER, T. ; PEIL, U.: Vereisung von Kabeln. in: *Stahlbau* 78 (2009), October, No. 11, pp. 841-848. – [in German]

[161] WAGNER, T. ; PEIL, U. ; BORRI, C.: Numerical investigation of conductor bundle icing. in: *5th European and African Conference on Wind Engineering*. Florence, Italy, July 2009, pp. 473-476

[162] WAIBEL, K.: Die meteorologischen Bedingungen fiir Nebelfrostablagerungen an Hochspannungsleitungen im Gebirge. in: *Archiv für Meteorologie, Geophysik und Bioklimatologie* B3 (1955), pp. 74-83. – [in German]

[163] WANG, J. ; LILIEN, J.-L.: A new theory for torsional stiffness of multi-span bundle overhead transmission lines. in: *Power Delivery, IEEE Transactions on* 13 (1998), October, No. 4, pp. 1405 -1411. – ISSN 0885-8977

[164] WANG, J. ; LILIEN, J.-L.: Overhead electrical transmission line galloping. A full multi-span 3-DOF model, some applications and design recommendations. in: *Power Delivery, IEEE Transactions on* 13 (1998), July, No. 3, pp. 909 -916

[165] WARIS, M. B. ; ISHIHARA, T. ; SARWAR, M. W.: Galloping response prediction of

ice-accreted transmission lines. in: *4th Advances in Wind and Structures (AWAS'08)*, 2008

[166] WESTERHELLWEG, A. ; MÖNNICH, K.: Evaluation of operational data in respect to production losses due to icing. in: *13th International Workshop on Atmospheric Icing*, 2009

[167] WILCOX, D. C.: *Turbulance modeling for CFD*. DCW Industries, 1998

[168] WILDHALM, M. ; RONZHEIMER, A. ; MEYERZ, J: Lagrangian particle tracking on large unstructured three-dimensional meshes. in: *46th AIAA Aerospace Sciences Meeting and Exhibit, Reno, Nevada, USA* vol. AIAA-2008-472, 2008, pp. 1-19

[169] WILLIAMS, R. G. ; SUARIS, W.: An analytical approach to wake interference effects on circular cylindrical structures. in: *Journal of Sound and Vibration* 295 (2006), pp. 266-281

[170] WINDTECHNOLOGISCHE GESELSCHAFT: WtG-Merkblatt über Windkanalversuche in der Gebäudeaerodynamik / Windtechnologische Gesellschaft e. V. 1994

[171] YUKINO, T. ; MATSUDA, M. ; NISHIMURA, H.: New cyclic model of snow accretion on power cable. in: *12th International Workshop on Atmospheric Icing of Structures*, 2007

[172] ZAVARINA, M. V. ; GLUKHOV, V. G. ; MYTAREV, M. N.: Eine Methode zur Berechnung von Eislasten für hohe Bauwerke. in: *Zeitschrift für Meteorologie* 26.2 (1976), pp. 98-104. – [in German]

[173] ZAVARINA, M. V. ; LOMILINA, L. G.: Der Einfluß des Reliefs und der Seehöhe des Ortes auf die Größe der Eislasten. in: *Zeitschrift für Meteorologie* 26.2 (1976), pp. 105-106. – [in German]

[174] ZHANG, M. Y. ; ZHANG, H. ; ZHENG, L. L.: Simulation of droplet spreading, splashing and solidification using smoothed particle hydrodynamics method. in: *International Journal of Heat and Mass Transfer* 51 (2008), pp. 3410-3419

[175] ZHANG, Q. ; POPPLEWELL, N. ; SHAH, A. H.: Galloping of bundle conductors. in: *Journal of Sound and Vibration* 234(1) (2000), pp. 115-134

[176] ZIENKIEWICZ, O. C. ; TAYLOR ; ZHU: *The Finite Element Method: Its Basis and Fundamentals*. Elsevier Butterworth-Heinemann, 2005

[177] ZIENKIEWICZ, O. C. ; TAYLOR, R. L. ; NITHIAPARSU, P.: *The Finite Element Method for Fluid Dynamics*. Elsevier Butterworth-Heinemann, 2005

[178] ZOBEL, G.: Die Anwendung von Ergebnissen der Erforschung der Nebelfrostablagerungen in der Technik / Abhandlungen des Meteorologischen Dienstes der DDR. 1973 (107(14): pp. 3-6). – [in German]

Appendix A

Heat Transfer Coefficients of the Icicle Model

The following set of equations uses dimensionless quantities, common in fluid mechanics and thermodynamics, as well as the concept of natural and forced convection. Both is explained in more detail in section 3.2 and 3.4.

Heat Transfer Coefficient at the Icicle Tip

The heat transfer coefficient at the tip of an icicle is given by:

$$h_t = \frac{k_f \cdot Nu_t}{d_d}$$

where d_d is the diameter of the pendent drop and Nu_t the Nusselt number at the tip. The Nusselt number is calculated for natural and forced convection, whereas the higher one is used. In case of natural convection the Nusselt number is calculated by ([141] from [79]):

$$Nu_t^N = 1.83 + 0.398 \cdot Gr_t^{0.252}$$

with the Grashof number defined as:

$$Gr_t = \frac{g \cdot \rho \cdot d_d^3 \cdot (0°C - T_a)}{\mu^2}$$

where g is the gravity, T_a is the ambient temperature and μ is the dynamic viscosity of the air. In case of forced convection the Nusselt number is ([58] from [79]):

$$Nu_t^F = 2.0 + 0.538 \cdot Re_t^{0.5}$$

where Re_t is the Reynolds number, which is defined as:

$$R_t = \frac{u \cdot \rho \cdot d_d}{\mu}$$

where u is the wind velocity.

Heat Transfer Coefficient at the Icicle Wall

The heat transfer coefficient at the wall of an icicle is defined as:

$$h_w = \frac{k_f \cdot Nu_w}{l_i}$$

where l_i is the length of the icicle and Nu_w the Nusselt number at the wall. The Nusselt number is calculated for natural and forced convection and the higher one is used. For natural convection it is calculated in two steps. First by ([131] from [79]):

$$Nu^N_{w,l_i} = 0.478 \cdot Gr_w^{0.25}$$

where the Grashof number is given by:

$$Gr_w = \frac{g \cdot \rho \cdot l_i^3 \cdot (0°C - T_a)}{\mu^2}$$

where the temperature at the icicles surface is 0 °C and T_a is the ambient temperature. Second, in order to account for the curvature of the cylinder the following equation is used ([58] from [79]):

$$Nu^N_w = \frac{0.9 \cdot S \cdot Nu^N_{w,l_i}}{\ln(1 + 0.9 \cdot S)}$$

where

$$S = \frac{2 \cdot l_i}{d_i \cdot Nu^N_{w,l_i}}$$

where d_i is the diameter of the icicle.

In case of forced convection the following equations for smooth cylinder are used (from [79]):

$$\begin{aligned}
Nu^F_w &= 0.881 \cdot Re_w^{0.330} && for && 0.4 < Re_w \leq 4 \\
Nu^F_w &= 0.811 \cdot Re_w^{0.385} && for && 4 < Re_w \leq 40 \\
Nu^F_w &= 0.608 \cdot Re_w^{0.466} && for && 40 < Re_w \leq 4 \cdot 10^3 \\
Nu^F_w &= 0.172 \cdot Re_w^{0.618} && for && 4 \cdot 10^3 < Re_w \leq 4 \cdot 10^4 \\
Nu^F_w &= 0.024 \cdot Re_w^{0.805} && for && 4 \cdot 10^4 < Re_w \leq 4 \cdot 10^5
\end{aligned}$$

where Re_w is the Reynolds number:

$$Re_w = \frac{u \cdot \rho \cdot d_i}{\mu}$$

Appendix B

Analytical Calculation of Heat Flux at a Cylinder Surface

A basic calculation of the heat flux at a cylinder surface in a flow is presented in the following. It is used in section 3.4 to verify the heat transfer model.

Reynolds number:

$$Re_c = \frac{\rho \cdot u \cdot l}{\mu}$$

where ρ is the fluid density, u is the velocity and μ is the dynamic viscosity. In contrast to the common definition is the characteristic length of the cylinder here defined as $l = 0.5 \cdot \pi \cdot d$, with d the cylinder diameter.

Prandtl number:

$$\mathrm{Pr} = \frac{\mu \cdot c_p}{k_f}$$

where c_p specific heat capacity at constant pressure and k_f is the thermal conductivity.
The Nusselt number for cylinder in a flow is given by:

$$Nu_c = 0.3 + \sqrt{Nu_{laminar}^2 + Nu_{turbulent}^2}$$

with

$$Nu_{laminar} = 0.664 \cdot \sqrt{Re_c} \cdot \sqrt[3]{\mathrm{Pr}}$$

$$Nu_{turbulent} = \frac{0.037 \cdot Re_c^{0.8} \cdot \mathrm{Pr}}{1 + 2.443 \cdot Re_c^{-0.1} \cdot \left(\mathrm{Pr}^{2/3} - 1\right)}$$

The heat flux is then computed by:

$$q = \frac{Nu_c \cdot k_f}{l} \cdot (T_s - T_a)$$

where T_s is the surface temperature and T_a the ambient temperature in the fluid.